Recruitment of host factors and organelles to the *Chlamydia trachomatis* inclusion

Rachel Jayne Ende
Colorado Springs, Colorado

Bachelor of Arts in Biology, Illinois Wesleyan University, 2016
Master of Science in Biological and Physical Sciences, University of Virginia, 2018

A Dissertation presented to the Graduate Faculty
of the University of Virginia in Candidacy for the Degree of
Doctor of Philosophy

Department of Microbiology, Immunology, and Cancer Biology

University of Virginia
August 2022

Abstract

Chlamydia trachomatis is the leading cause of non-congenital blindness and the causative agent of the most common sexually transmitted infection of bacterial origin. Upon entering a host cell, *C. trachomatis* resides within a membrane bound vacuole, the inclusion. Inclusion membrane proteins (Incs) are embedded within the inclusion membrane and possess cytosolic tails that can mediate interactions between the inclusion with host molecules and organelles. These interactions include the formation of membrane contact sites (MCS) between the inclusion and the host cell endoplasmic reticulum (ER), referred to as ER-Inclusion MCS. These contact sites are proposed to play an important role in *C. trachomatis* development through the non-vesicular trafficking of host cell lipids to the inclusion.

Overall, my thesis work has focused on how the *C. trachomatis* inclusion interacts with the host cell environment to establish and maintain a replicative niche. I first sought to better understand the formation and function of ER-inclusion MCS during *C. trachomatis* infection by determining their molecular composition. I used a proximity labeling approach to isolate and identify bacterial and host cell components of ER-inclusion MCS and identified six host glycolytic enzymes (Chapter 2). I demonstrated that host glycolytic enzymes, while not specific to ER-inclusion MCS, localize to the inclusion membrane. Additionally, I showed that the host glycolytic enzyme Aldolase A plays a role in *C. trachomatis* intracellular development (Chapter 3). These findings indicate that, in addition to interactions with host organelles, *C. trachomatis* relies on host cell metabolism for proper intracellular development.

Our lab had previously shown that the interaction of the *C. trachomatis* Inc protein IncV with the ER-resident protein VAP acts as a tether to support the formation/maintenance of ER-inclusion MCS. I next sough to identify cellular determinants that promote the assembly of this bacterial tether. In chapter 4, we demonstrated that the host kinase CK2 is recruited to the inclusion and that multiple layers of host cell kinase-mediated phosphorylation events govern the assembly of the IncV-VAP tethering complex and the formation of ER-inclusion MCS.

Finally, in chapter 5, I discuss how my findings shed light on the interplay between host and bacterial metabolism during *C. trachomatis* pathogenesis and provide insights into the general biology of MCS. Overall, my work could contribute to the identification of novel therapeutic targets and combat the blindness and infertility that can arise from chlamydial infections.

Acknowledgments

I would first like to thank my mentor, Dr. Isabelle Derré, for her constant guidance and advice throughout my graduate career. She has truly pushed me to become a better scientist and has provided me with a valuable skillset that I will take with me as I pursue my future career as a scientist. She has also continued to support me outside of the lab, often sitting front row at my a cappella concerts, for which I am truly grateful.

I would also like to thank my fellow lab members over the years Clayton Bishop, Dr. Maria Eugenia Cortina, Samantha D'Spain, and Dr. Rebecca Murray. I cannot thank you all enough for creating such a kind, caring, and supportive lab environment to work in. You all have supported me through my failures and celebrated my successes and helped me to grow, thank you.

I also want to thank the members of my thesis committee, Dr. Anna Cliffe, Dr. Hervé Agaisse, Dr. Sarah Ewald, and Dr. Jim Casanova. Your support, feedback, and ideas have been encouraging and helpful throughout my training.

I would also like to thank the amazing friends that have supported me through graduate school. The friendships I have made at UVA and in Charlottesville are friendships that I will continue to treasure for the rest of my life. Through coffee breaks, game nights, movies, hiking, and singing, these friendships have brought me such joy and have gotten me through the inevitable difficult times during graduate school.

Last, but most certainly not least, I would like to thank my family for their unwavering love and support. Simply put, I would not be where I am today without you. I would especially like to thank my parents Karen and David Ende. From a young age you taught me to embrace my curiosity and encouraged me to follow my dreams however far

they may take me. Thank you for always being there for me when I need you. Thank you also to my siblings, Michael and Erin, for always believing in me and for providing humor and distraction when I needed it.

List of abbreviations

3D: three-dimensional

AldoA: Aldolase A

aTc: anhydrotetracycline

ATP: adenosine triphosphate

AU: Arbitrary units

Ca^{2+}: calcium

CERT: ceramide transfer protein

CFEM: correlative fluorescence and electron microscopy

CHL: chloramphenicol

CHX: Cycloheximide

COPD: chronic obstructive pulmonary disease

Cyto D: Cytochalasin D

dhnA: Fructose-bisphosphate aldolase

E-syts: extended synaptotagmins

EB: elementary body

EMS: ethyl methanesulfonate

ER: endoplasmic reticulum

FFAT: two phenylalanines (FF) in an Acidic Tract

FFNT: two phenylalanines (FF) in a Neutral Tract)

FL: full length

GART: Glycinamide ribonucleotide transformylase

Glucose-6P: Glucose-6-Phosphate

HBV: Hepatitis B Virus

HCV: Hepatitis C virus

IFUs: inclusion forming units

Inc: inclusion membrane proteins

LDHA: Lactate Dehydrogenase

LVG: Lymphogranuloma venereum

MCS: membrane contact sites

MOSPD: <u>mo</u>tile <u>sp</u>erm <u>d</u>omain-containing proteins

MTOC: microtubule organizing center

NMR: Nuclear magnetic resonance

ORF: open reading frame

OSBP: <u>O</u>xy<u>s</u>terol <u>b</u>inding protein

OSBP: <u>o</u>xy<u>s</u>terol-<u>b</u>inding protein

PAICS: Phosphoribosylaminoimidazole carboxylase

PEP: phosphoenolpyruvate

pgi: glucose-6-phosphate isomerase

pi: post-infection

PI4P: phosphatidylinositol 4-phosphate

PKM2: Pyruvate Kinase

PM: plasma membrane

PNBM: P-Nitrobenzyl mesylate

PP1: protein phosphatase 1

PP4: Protein phosphatase 4

PPP: pentose phosphate pathway

PPPs: Phosphoprotein phosphatases

pykF: Pyruvate Kinase

RT-qPCR: quantitative reverse transcription PCR

RB: reticulate body

rRNA: ribosomal RNA

SAINT: Significance Analysis of INTeractome

SD: standard deviation

STIM1: stromal interaction molecule 1

STOMP: Spatially Targeted Optical Micro Proteomics

T3SS: type III secretion system

TarP: translocated actin-recruiting phosphoprotein

TBS: Tris-buffered saline

TCA cycle: tricarboxylic acid cycle

VAPs: VAMP-associated proteins

vCLAMPS: mitochondria–vacuole contact sites

λ: lambda

List of Figures

Figure 5.1. Phosphorylatable serine residues upstream of the IncV FFAT motifs cores mimic acidic tracts upstream of eukaryotic FFAT motif cores

Table of Contents

Chapter 1:

Introduction

Chlamydia

Chlamydia species are gram negative, obligate intracellular pathogens belonging to the

Chlamydiaceae family of bacteria (1). The *Chlamydiaceae* family includes the causative

agents of several diseases affecting humans, livestock, and other animals (1). The

majority of *Chlamydia* species infect animals, including the mouse pathogen *C.*

muridarum, which causes respiratory and genital tract infections in infected mice (2, 3).

There are currently four *Chlamydia* species that are known to infect humans: *C.*

trachomatis, *C. pneumoniae*, *C. psittaci*, and *C. abortus* (4). *C. pneumoniae* typically

infects the lungs and can cause respiratory tract infections such as pneumonia and several

inflammatory conditions including chronic obstructive pulmonary disease (COPD) (5, 6).

C. psittaci most commonly infects birds, but can infect humans and cause psittacosis, a

flu-like respiratory illness, or pneumonia (7). *C. abortus* most commonly infects

ruminants and is the most common cause of infectious abortion in sheep and goats (8, 9).

Although rare, *C. abortus* has been shown to infect humans and can cause respiratory

illness and infectious abortion (8).

  C. trachomatis is the major human pathogenic species and can cause sexually

transmitted infections, eye infections, and pneumonia (10, 11). *C. trachomatis* serovars

are categorized into three main biovars based on the type of disease they cause: 1) the

trachoma biovar, 2) the genital biovar, and 3) the Lymphogranuloma biovar (12). These

biovars are further broken down into 15 distinct serovars based on the surface antigen

that the immune system recognizes. Serovars A-C cause the ocular infection trachoma,

which is the leading cause of non-congenital blindness worldwide (13). Serovars D-K

cause the genital tract infection known as Chlamydia, the most common sexually

transmitted infection of bacterial origin (11). Serovars L1-L3, although also transmitted sexually, cause a systemic infection Lymphogranuloma venereum (LGV) that disseminates to the lymph nodes (14, 15).

Treatment and pathogenesis of *C. trachomatis* infections

Currently, the treatment recommended by the CDC is Doxycycline administered orally twice a day for seven days, or a single dose of Azithromycin administered orally (16). Doxycycline is not recommended for treatment of pregnant women after the first trimester, thus Azithromycin is the treatment of choice in pregnant women (17). Although *C. trachomatis* can be treated with antibiotics, an effective vaccine has yet to be developed. The development of a vaccine is especially important due to the high amount of asymptomatic infections associated with *C. trachomatis* (18-21). Over 80% of *C. trachomatis* infections are asymptomatic in women and asymptomatic infection rates in men can be as high as 50% (20, 22). Due to the high rates of asymptomatic infection, *C. trachomatis* infections often go untreated, resulting in severe sequalae. In the case of trachoma, lack of treatment can result in blindness (13), and untreated genital tract infections are associated with pelvic inflammatory disease, ectopic pregnancy, and infertility (11, 23). Additionally, untreated *C. trachomatis* infections in pregnant women can lead to vertical transmission during delivery and cause conjunctivitis or *C. trachomatis*-associated pneumonia in infants (24).

***Chlamydia* developmental cycle**

Chlamydiae species primarily infect epithelial cells (25) and all *Chlamydiae* species share

a unique biphasic developmental cycle (Figure 1.1) (26). Throughout the developmental

cycle, *Chlamydia* transitions between two developmental forms, the non-dividing

infectious form, known as the elementary body (EB), and the non-infectious replicative

form, referred to as the reticulate body (RB) (26-28). Upon inducing its own endocytosis

into the host cell, the infectious EBs remain within a membrane bound vacuole called the

inclusion (27-29). The inclusion then traffics along microtubules to the microtubule

organizing center (MTOC) near the nucleus (30, 31) and the EBs transition into the

replicative RB form (28). If more than one EB enters the cell, they will initially form

individual inclusions that will later fuse to form a single inclusion (32). The RBs will

continue to replicate and divide within the inclusion. At 24-48 hours post-infection, the

RBs will begin to asynchronously transition back into infectious EBs (28). At 48-72

hours post-infection, the bacteria can exit the cell either through lysis of the host cell or

extrusion (33, 34). Once released, the infectious EBs are able to infect neighboring host

cells.
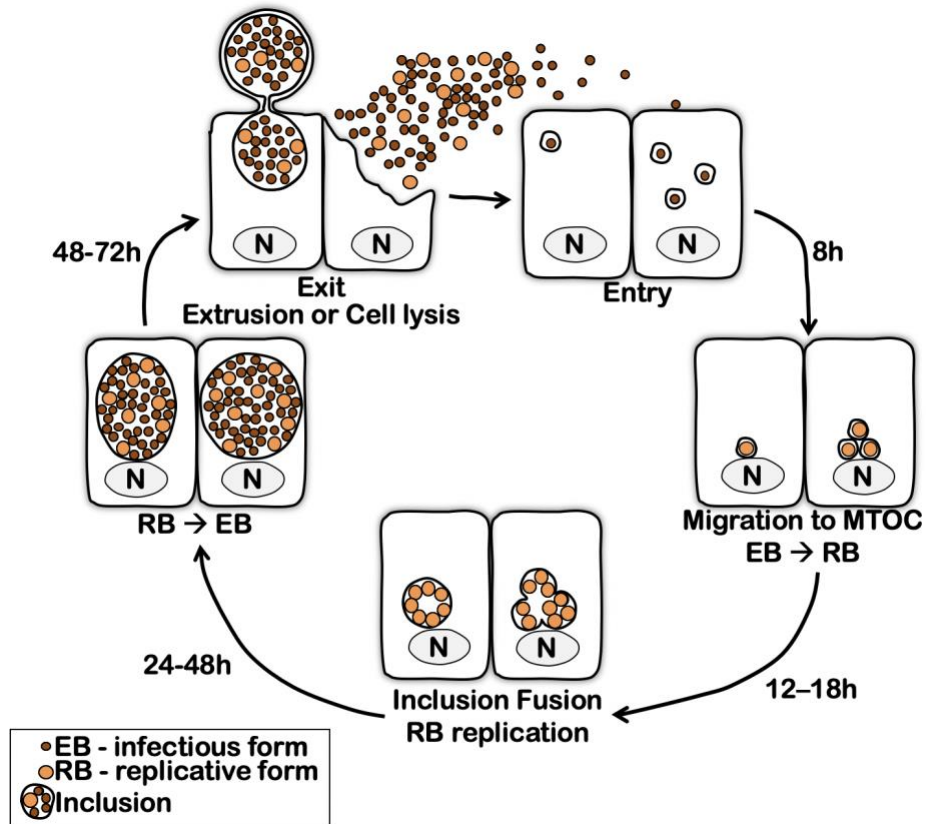
Figure 1.1. *Chlamydia* **life cycle**. Upon entry into the host cell, the infectious elementary body (EB, dark brown) is enclosed in a membrane-bound vacuole termed the inclusion. The inclusion traffics along microtubules to the microtubule organizing center (MTOC) near the nucleus. By 8 hours post-infection, the infectious EB transitions into a replicative reticulate body (RB, light brown). If more than one EB enters the cell, the individual inclusions will fuse between 12-28 hours post-infection. The RBs continue to replicate and divide within the inclusion. At 24-48 hours post-infection the RBs will begin to asynchronously transition back into infectious EBs. At 48-72 hours post-infection the bacteria exit the host cell, either through extrusion or host cell lysis and to begin the cycle again. N = nucleus. Figure courtesy of Rebecca Murray.

Central carbon metabolism

Throughout its intracellular life cycle, *Chlamydia* must influence and interact with host cell central carbon metabolism to establish an intracellular niche. Central carbon metabolism is the collection on enzymatic processes by which carbohydrates are converted to metabolic intermediates that are used to generate energy and biomass. Central metabolism is comprised of three main metabolic pathways: glycolysis (also referred to as the Embden–Meyerhof–Parnas pathway), and the tricarboxylic acid (TCA) cycle (also referred to as the Krebs cycle or citric acid cycle), and the pentose phosphate pathway (PPP) (Figure 1.2A).

In glycolysis, a series of ten enzymatic reactions convert one six-carbon molecule of glucose into two three-carbon molecules of pyruvate, generating two molecules of adenosine triphosphate (ATP) and two molecules of nicotinamide adenine dinucleotide (NADH). Pyruvate generated by glycolysis can then be converted to acetyl-CoA and enter into the TCA cycle. The TCA cycle is a series of enzymatic reactions that serve to generate NADH and flavin adenine dinucleotide ($FADH_2$) as well as important metabolic intermediates that feed biosynthetic pathways, such as the synthesis of amino acids. The NADH and $FADH_2$ generated by glycolysis and/or the TCA cycle can donate electrons to the mitochondrial electron transport chain to drive ATP production, a process referred to as oxidative phosphorylation. In oxygen limiting conditions, however, pyruvate is converted to lactate by the enzyme lactate dehydrogenase.

Glycolytic intermediates can also supply other pathways important for cellular growth. Most notably, the glycolytic intermediate glucose-6-phosphate is used to drive the pentose phosphate pathway. The pentose phosphate pathway leads to the generation

of NADPH and ribose-5-phosphate. Ribose-5-phosphate is a building block for nucleic acid synthesis and NADPH provides reducing power for the synthesis of fatty acids, sterols, nucleotides and non-essential amino acids.

C. trachomatis metabolism

As an obligate intracellular pathogen with a reduced genome (35-37), *C. trachomatis* was thought for many years to be an energy parasite, relying on the host cell for energy production (38-41). Early studies were not able to detect glycolytic enzyme activity or electron transport chain components necessary for oxidative phosphorylation (27). Additional studies found that treatment of *C. trachomatis* infected fibroblast with inhibitors of mitochondrial function resulted in a reduction of the number of bacteria recovered (40), suggesting that *C. trachomatis* depends on mitochondrial ATP. Some of the strongest support for the energy parasite hypothesis was the identification and characterization of a chlamydial ATP-ADP translocase, which would allow *Chlamydia* to exchange ADP for host cell ATP (41).

However, sequencing of the *C. trachomatis* genome has provided new insight into the metabolic capacity of *Chlamydia*. Genome sequencing revealed that *C. trachomatis* possesses components of the electron transport chain and ATP synthase complex, suggesting that *C. trachomatis* can drive a minimal electron transport chain to produce ATP through oxidative phosphorylation (37). *C. trachomatis* also has an intact pentose phosphate pathway and a partial TCA cycle (37, 42)(Figure 1.2B). Additionally, *C. trachomatis* possess a nearly complete glycolytic pathway (37). Genomic data revealed that *C. trachomatis* only lacks the gene for Hexokinase, the first enzyme of the pathway

responsible for converting glucose to glucose-6-phosphate (37). Instead, glucose-6-phosphate is taken directly from the host cell via the UhpC antiporter produced by *Chlamydia* (43, 44) (Figure 1.2B). The functionality of the *C. trachomatis* glycolytic enzymes was confirmed through heterologous expression in *E. coli* mutants (45). However, saturated EMS mutagenesis resulted in a loss-of-function mutation in bacterial glucose-6-phosphate isomerase (*pgi*), the enzyme responsible for shuttling glucose-6-phosphate into the glycolytic pathway, thus the enzymes are proposed to be expendable (46).

Early studies showed that RBs are capable of RNA, DNA, and protein synthesis during infection (47-49), but are reliant on molecular ATP in assays of host free protein synthesis (47). However, these same activities were not observed in EBs, leading to EBs being described as metabolically inert. More recent studies, however, have determined that bacterially encoded glycolytic enzymes are present in both RBs and EBs (50, 51). Work by Omsland et al. suggests that while RBs are strictly dependent on ATP as an energy source, EBs preferentially require glucose-6-phosphate (52).

While studies continue to shed light on the metabolic capacity of *C. trachomatis*, many questions remain regarding the interplay between host and bacterial metabolism and the full extent to which host metabolism plays a role in *C. trachomatis* intracellular development.
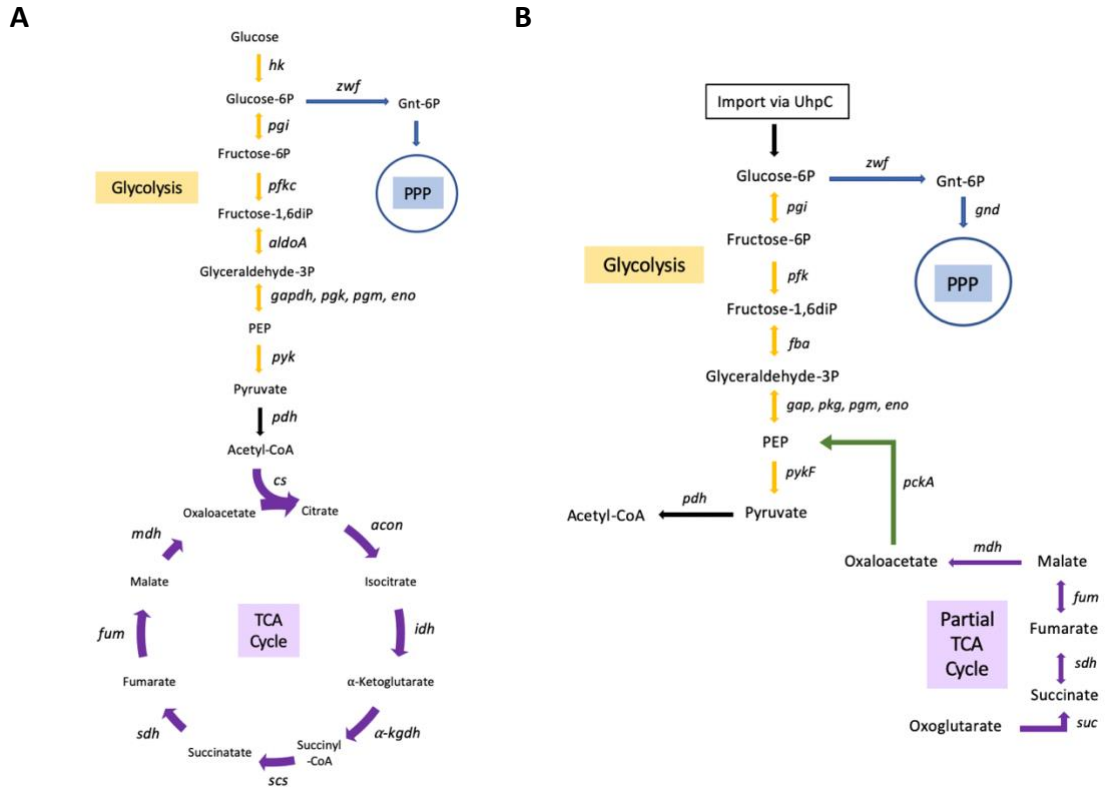
Figure 1.2 Central Carbon Metabolism. A) A schematic representation of central carbon metabolism. Glucose is metabolized by glycolysis (orange arrows) and the pentose phosphate pathway (PPP, blue arrows). Pyruvate generated by glycolysis can be converted into acetyl-CoA and enter the tricarboxylic acid (TCA) cycle (purple arrows). B) Schematic representation of *C. trachomatis* central carbon metabolism. Glucose-6-Phosphate (Glucose-6P) is directly imported via the UhpC transporter and is metabolize by glycolysis and the PPP. *C. trachomatis* possess a partial TCA cycle and phosphoenolpyruvate (PEP) carboxylase (PckA) connects the partial TCA with glycolysis (green arrow).

Manipulation of host metabolism by *C. trachomatis*

Although it is now clear that *Chlamydia* is not merely an energy parasite, *Chlamydia* is still reliant on the host cell to meet its metabolic needs. For example, *Chlamydia* obtains nucleotides, amino acids, and iron from the host cells and lipids by vesicular and non-vesicular trafficking from the ER (12). Additionally, a genome wide RNA interference screen and identified two glycolytic enzymes, glucose-6-phosphate isomerase and 6-phosphofructokinase, as potentially involved in *Chlamydia* progeny production (53). Metabolite profiling of central carbon metabolism following *C. trachomatis* infection revealed increased levels of pyruvate, lactate, and glutamate (53). The upregulation of these metabolites is indicative of Warburg metabolism, commonly exhibited by cancer cells, in which metabolism is altered to favor anaerobic glycolysis over oxidative phosphorylation (54-56). This hyper metabolic state results in the accumulation of glycolytic intermediates that can be shuttled into the pentose phosphate pathway and used for ribonucleotide synthesis. These findings suggest that *C. trachomatis* infection shifts the cell into this hypermetabolic state, effectively forcing the host cell to generate anabolic substrates that the bacteria can then scavenge from the host.

***Chlamydia* inclusion membrane proteins**

Chlamydia species possess a needle-like apparatus, called a type III secretion system (T3SS), that allows for the injection of bacterial effectors directly into the host cell cytosol (Figure 1.3A) (57-61). *Chlamydia* utilizes the T3SS to translocate effectors that can interact with, and manipulate, the host cell (29, 62). One major group of these type three secreted effectors is the inclusion membrane proteins (Incs) (Figure 1.3B). Inc

proteins are integral membrane proteins that are translocated through the *Chlamydia*

T3SS and embedded within the inclusion membrane (29, 62-65). Inc proteins are

characterized by one or more bi-lobed transmembrane domains and cytosolic tails that are

available to interact with host molecules and organelles (63). Inc proteins are thus well

positioned to mediate interactions between the inclusion and the host cell. Inc proteins

have been shown to serve numerous functions throughout infection, including modulating

host cell vesicular trafficking, controlling inclusion membrane stability and host cell

death, modulating the Golgi and the host cell cytoskeleton, interactions with the ER, and

controlling chlamydial exit from host cells (62). The purposed functions and host

interacting partners of known Inc proteins are summarized in Table 1.1.

Table 1.1 Interacting partners and proposed function of experimentally validated *C.*

***trachomatis* Inc proteins**

Annotated Name D/L2	Common Name	Host Interacting Partner(s)	Proposed Function(s)	References
CT005/ CTL0260	IncV	VAPA/B	Formation of ER-inclusion MCS	(66-69)
CT006/ CTL0261	-	Unknown	Interactions with LDs	(67)
CT101/ CTL0356	MrcA	ITPR3	Promotion of chlamydial extrusion	(66, 70, 71)
CT115/ CTL0370	IncD	CERT	Formation of ER-inclusion MCS; non-vesicular lipid trafficking	(72-74)
CT116/ CTL0371	IncE	SNX5/6	Modulation of retromer-dependent trafficking	(67, 72, 73, 75-77)
CT117/ CTL0372	IncF	Unknown	Inc-Inc interactions	(67, 72, 73, 78)
CT118/ CTL0373	IncG	14-3-3β	Associates with LDs	(72, 73, 79, 80)
CT119/ CTL0374	IncA	VAMP3/7/8	Homotypic inclusion fusion; regulation of host cell vesicular trafficking; associates with LDs	(69, 72, 73, 81-87)
CT134/ CTL0389	-	Unknown	Unknown	(67)
CT135/ CTL0390	-	Unknown	Important for chlamydial virulence in a mouse infection model.	(67, 88, 89)
CT147/ CTL0402	-	Unknown	Unknown	(67, 72, 90)
CT179/ CTL0431	-	Unknown	Unknown	(67)
CT192/ CTL0444	-	Unknown	Unknown	(67)
CT222/ CTL0475	-	Unknown	Inc-Inc interactions	(66, 67, 70, 78)
CT223/ CTL0476	IPAM	CEP170	Modulation of the microtubule network; inhibition of host cell cytokinesis	(63, 66, 67, 72, 91, 92)
CT224/ CTL0477	-	Unknown	Inhibition of host cell cytokinesis	(66, 67, 92)
CT225/ CTL0477A	-	Unknown	Inhibition of host cell cytokinesis	(66, 72, 92)
CT226/ CTL0478	-	Unknown	Unknown	(66, 67, 72, 93)
CT227/ CTL0479	-	Unknown	Unknown	(66, 67)
CT228/ CTL0480	-	MYP1	Inhibition of chlamydial extrusion	(66, 72, 94, 95)
CT229/ CTL0481	CpoS	Small GTPase RAB proteins	Control of inclusion membrane stability and/or host cell death, and of host cell vesicular trafficking	(63, 66, 67, 72, 96-99)
CT232/ CTL0484	IncB	Unknown	Unknown	(67, 70, 72)
CT233/ CTL0485	IncC	Unknown	Control of inclusion membrane stability	(63, 67, 72, 99)
CT249/ CTL500A	-	Unknown	Unknown	(66, 72, 100)
CT288/ CTL0540	-	CCDC146	Unknown	(63, 67, 72, 101)
CT345/ CTL0599	-	Unknown	Unknown	(67)
CT358/ CTL0612	-	Unknown	Unknown	(72)

CT383/ CTL0639	-	Unknown	Modulation of inclusion membrane stability	(67, 99)
CT440/ CTL0699	-	Unknown	Unknown	(72)
CT442/ CTL0701	CrpA	Unknown	Unknown	(63, 67, 72, 102)
CT449/ CTL0709	-	Unknown	Unknown	(67)
CT483/ CTL0744	-	Unknown	Unknown	(66)
CT565/ CTL0828	-	Unknown	Unknown	(66)
CT618/ CTL0882	-	Unknown	Associates with LDs	(72, 80, 103)
CT813/ CTL0184	InaC	14-3-3 proteins, ARF1/4, VAMP7/8	Modulation of post-translational modification of microtubules, and of F-actin and Golgi redistribution around the inclusion	(46, 66, 72, 84, 104, 105)
CT850/ CTL0223	-	DYNLT1	Inclusion positioning at the centrosomal region	(66, 70)
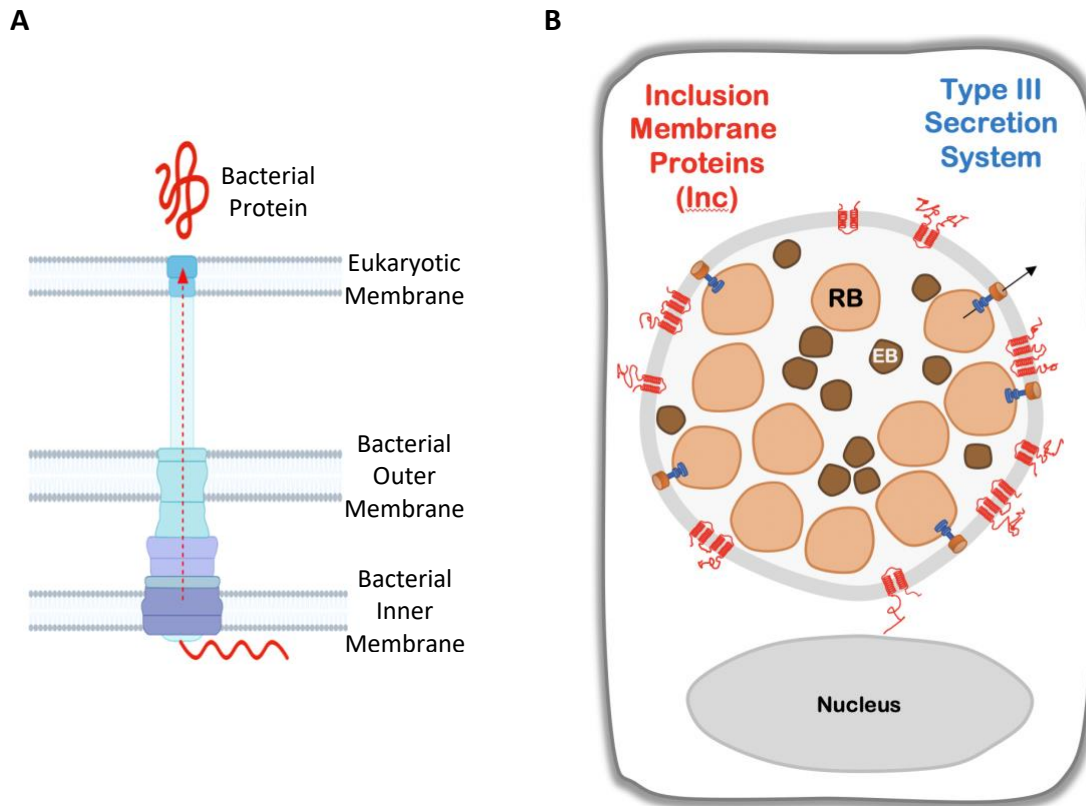
Figure 1.3 Type III secretion systems and inclusion membrane proteins. A) Schematic of a bacterial Type III secretion system (T3SS) (blue/purple). Proteins generated by the bacteria (red) are translocated through the T3SS into the cytosol of the eukaryotic host cell. B) Schematic of a *C. trachomatis* inclusion within an epithelial cell. Inclusion membrane proteins (Inc) (red) are translocated through the *C. trachomatis* T3SS (blue/orange) and are embedded within the inclusion membrane. Inc proteins are characterized by the presence of two or more bi-lobbed transmembrane domains and cytosolic tails. RB, reticulate body (tan). EB, elementary body (brown). The schematic in A was created with BioRender.com and the schematic in B is courtesy of Rebecca Murray.

***C. trachomatis* interactions with host cell factors and organelles**

As an intracellular pathogen, *C. trachomatis* must be able to interact with multiple host

cell factors and organelles in order to establish and maintain a replicative niche. *C.*

trachomatis T3SS effectors, especially the Inc proteins, play a major role in facilitating

interactions with the host cell (29, 62). In fact, the inclusion has been shown to interact

with a wide range of host factors and organelles throughout development including, the

host cytoskeleton, mitochondria, Golgi apparatus, and the endoplasmic reticulum (12,

26).

Interactions with the host cytoskeleton

The host actin cytoskeleton plays a major role throughout the *C. trachomatis*

developmental cycle. Following initial attachment of *C. trachomatis* to the cell surface,

the *Chlamydia* T3SS effector t̲ranslocated a̲ctin-r̲ecruiting p̲hosphoprotein (TarP) is

secreted into the host cytosol and induces actin nucleation and pedestal formation that

facilitates internalization of the bacterium (106). In addition to its role in internalization,

actin has been shown to play a role in stabilizing the inclusion throughout development

(107, 108). The inclusion becomes surrounded by a cage of actin and intermediate

filaments, and disruption of this actin cage was shown to result in loss of inclusion

integrity (107). The formation of this actin cage around the inclusion is mediated by host

factors, such as RhoA, ARF GTPases, septins, EGFR signaling, and the Inc protein InaC

(46, 105, 109-112).

Microtubules also play a role in *C. trachomatis* development, particularly early in

the developmental cycle. Following internalization, inclusions traffic along microtubules

to the Microtubule Organizing Center (MTOC) (30, 31). Similar to what has been observed for actin and intermediate filaments, post-translationally modified microtubules have been shown to encase the inclusion and have been purposed to function in the redistribution of the Golgi around the inclusion (105, 113). Several Inc proteins (MrcA, CT222, IPAM, CT224, CT228, IncB, IncC, CT288, CT850) have been shown to localize to areas of the inclusion in contact with host centrosomes and have been predicted to act as a platform for interactions with the centrosome, microtubules, and the actin cytoskeleton (70, 91, 94, 114).

Interactions with the Golgi apparatus

For proper development, *C. trachomatis* relies on acquisition of host lipids, such as sphingomyelin, that are synthesized in the Golgi (115-117). During *C. trachomatis* development the Golgi apparatus is fragmented into "mini-stacks" that are redistributed around the inclusion membrane (118). Golgi-fragmentation and redistribution were purposed to play a role in *Chlamydia* growth by allowing for an increase in sphingomyelin acquisition (118). However, more recent studies have shown that, although lipid acquisition from the Golgi is essential for normal *C. trachomatis* development, fragmentation of the Golgi is not (119). This redistribution of the Golgi around the inclusion requires the Inc protein InaC, host ARF GTPases, and the presence of intact F-actin filaments, however an InaC mutant strain of *C. trachomatis* is not deficient in sphingolipid trafficking (46, 105). Overall, while the acquisition of lipids from the Golgi is important for *C. trachomatis* normal development, the role of Golgi fragmentation in development is not fully understood.

<u>Interactions with Mitochondria</u>

Mitochondria have been shown to associate with the *C. pssitaci* inclusion but have not been shown to directly associate with *C. trachomatis* or *C. pneumoniae* inclusions (120, 121). Although there is not a direct physical association of mitochondria with the inclusion, *C. trachomatis* infection has been shown to regulate mitochondrial dynamics to promote intracellular survival and replication (122, 123). Work by Chowdhury et al. (2017) showed that *C. trachomatis* infection resulted in the upregulation of the microRNA miR-30c. This miRNA is linked to the downregulation of the mitochondrial fission protein Drp. Upon depletion of miR-30c, *C. trachomatis* growth was severely decreased and mitochondria appeared fragmented, indicating that *C. trachomatis* actively protects mitochondrial integrity to support it infection and replication (122). Further study has indicated that *C. trachomatis* modulation of mitochondrial dynamics is dependent on stage of infection, with mitochondria being elongated in early stages of infection and fragmented at later stages of infection (123).

<u>Direct interactions with the Endoplasmic Reticulum</u>

Direct interaction between the *C. trachomatis* inclusion and the endoplasmic reticulum (ER) was first observed by election microscopy in 1988, where both smooth and rough ER vesicles were shown to be in close contact with the inclusion (124). Since this finding, similar observations have been made, and these direct interactions are now referred to as ER-inclusion MCS and pathogen synapses (74, 125-128). Our lab identified patches of the ER maintained in close proximity (10-20nm) to the inclusion without membrane fusion (Figure 1.4) (74). Due to the morphological and molecular similarities

to membrane contact sites (MCS) that form between the ER and many cellular organelles, these sites have been termed ER-Inclusion membrane contact sites (MCS) (74, 129). Both MCS and ER-Inclusion MCS are discussed in more detail in the following "Membrane contact sites" and "ER-Inclusion membrane contact sites" sections. Pathogen synapses were first identified by electron and immunolabeling microscopy as areas of the inclusion membrane that were closely opposed to rough ER structures and appeared to be connected by ordered arrays of T3SS complexes (127, 128). Currently, the function and molecular composition of pathogen synapses are not well understood, and it remains unknown if ER-inclusion MCS and pathogen synapses are describing the same structure.
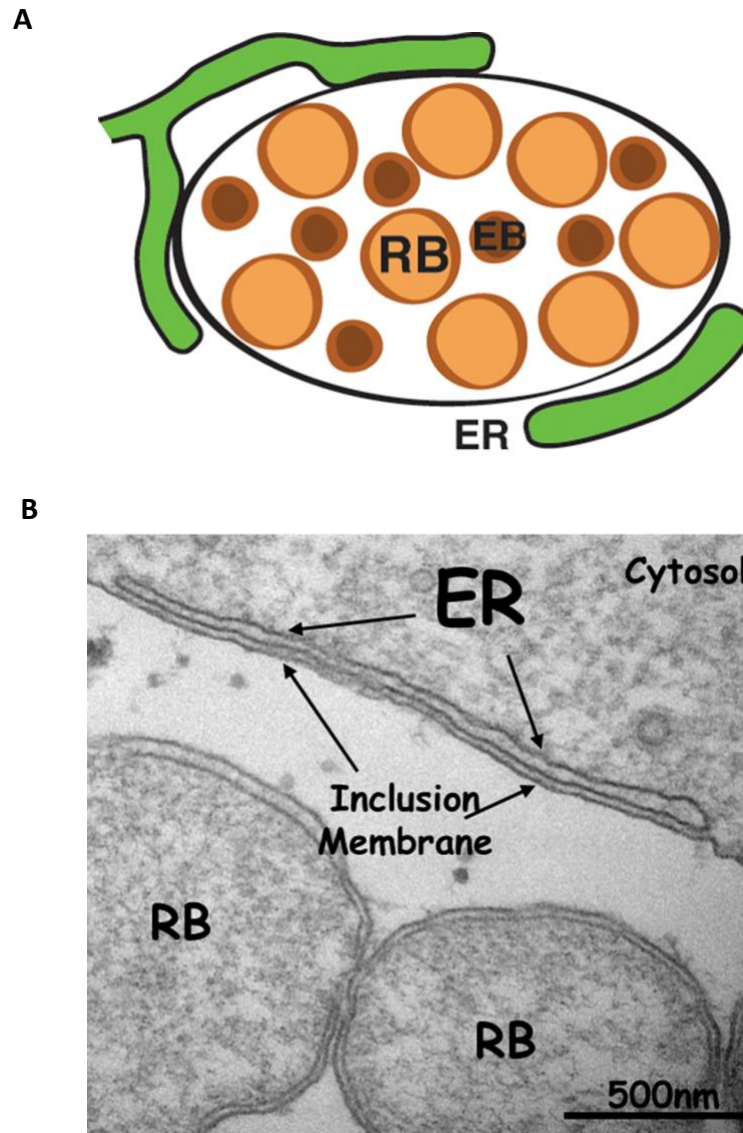
Figure 1.4 ER-Inclusion membrane contact sites. A) Schematic representation of ER-inclusion membrane contact sites (MCS) that form between the *C. trachomatis* inclusion and the host endoplasmic reticulum (ER) (green). RB, reticulate body (tan). EB, elementary body (brown). B) Transmission electron micrograph depicting a tubule of the ER in close apposition to the inclusion membrane (arrowheads). Scale bar, 500nm. RB, reticulate body. Schematic in A is adapted from Derré, 2015 and Figure B is courtesy of Isabelle Derré.

Membrane contact sites

While vesicular trafficking is responsible for the majority of lipid transport between membranes throughout the cell, non-vesicular trafficking allows for lipid transport in the absence of membrane trafficking to help to maintain membrane lipid homeostasis (130). Most non-vesicular trafficking is thought to occur at membrane contacts formed throughout the cell. MCS are zones of close apposition (10-30nm) between two organelles, with no membrane fusion occurring (129, 131), and serve as platforms for the non-vesicular lipid transfer, cell signaling, and ion exchange (132). In mammalian cells, the ER is known to form MCS with many cellular organelles such as mitochondria, endosomes, the Golgi, and the plasma membrane (132, 133)(Figure 1.5).
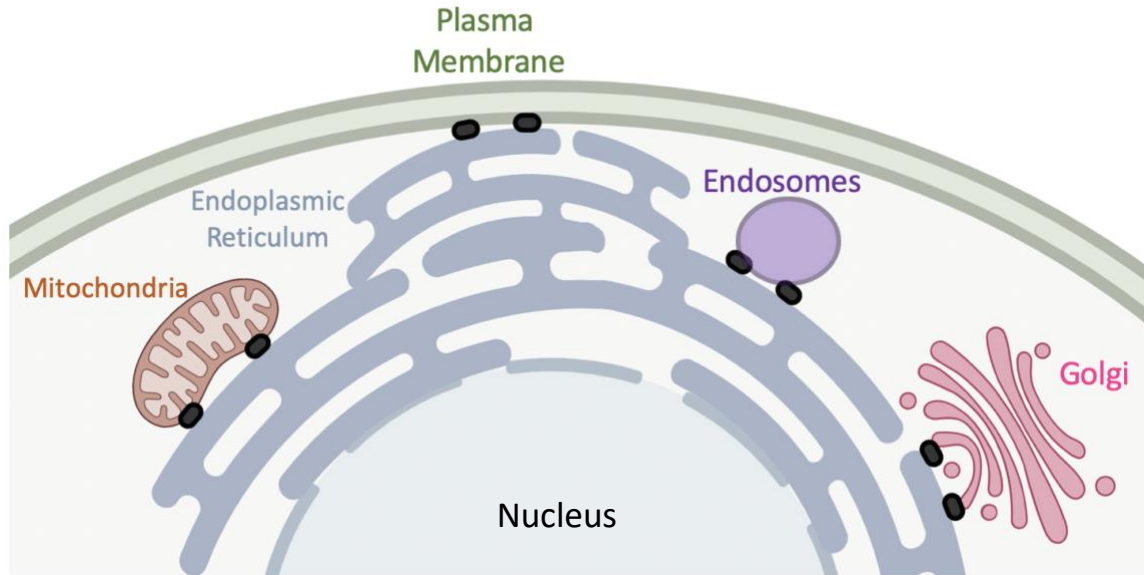
Figure 1.5 Cellular membrane contact sites. The endoplasmic reticulum (grey) forms membrane contact sites with most other cellular organelles. ER contacts with mitochondria (tan), the plasma membrane (green), endosomes (purple), and the Golgi (pink) are represented. Proteins enriched at each MCS are depicted with black ovals. Figure Created with BioRender.com.

Originally, proteins present at MCS were categorized as either functional components,

that function in lipid transfer and ion exchange, or structural components, which serve to

tether the two membranes together and aid in the formation and maintenance of MCS

(134). However, as the field continues to advance and more MCS are discovered, so does

our understanding of their components. More recently, four classes of MCS components

have been described: 1) structural proteins, 2) functional proteins, 3) sorter proteins, and

4) regulator proteins (131). Structural proteins often act as tethers to maintain the

organelles in close proximity (131). For example, the ER integral membrane proteins

oxysterol-binding protein (OSBP)-related protein 5 (ORP5) and ORP8 tether the ER to

the plasma membrane through interactions with phosphatidylinositol 4-phosphate (PI4P)

in the plasma membrane (135). Functional proteins are largely responsible for performing

ion, protein, lipid, or metabolite exchange at MCS (131). Such functional components

include ion channels, lipid transfer proteins, or metabolite channels/transporters. The

lipid transfer activity of the ceramide transfer protein (CERT) places CERT in this class

(136). Sorter proteins serve to define the protein and lipid composition at MCS through

recruitment of proteins to the MCS or modifying membrane lipids (131).

Phosphatidylinositol transfer proteins, for example, could be classified as sorter proteins,

due to the ability of these proteins to define the lipid composition of membranes (137).

Regulator proteins function dynamically to regulate the extent and activity of proteins at

membrane contact sites (131). For example, phosphorylation of the tether protein Vps39

by an unidentified kinase at mitochondria–vacuole contact sites (vCLAMPS) in yeast

regulates the tethering and formation of these contact sites (138). Kinases may often

serve as regulator proteins at MCS as post-translational modification has been recognized to play a major role in the regulation of protein interactions (139). For example, post-translation modification of CERT, can up- or down-regulate the interaction of CERT with ER-resident VAMP-associated proteins (VAPs) (140). It is important to note that these classifications are not mutually exclusive and MCS proteins may fall into more than one class (131).

Functions of ER-containing MCS

ER-containing MCS can have a large variety of functions throughout the cells, some of the most notable being the exchange of lipids and calcium (Ca^{2+}). The presence of lipid transfer proteins at many cellular MCS allows for the non-vesicular trafficking of lipids that occurs at these sites. Different lipid transfer proteins can localize to specific MCS depending on the lipids and proteins present for the lipid transfer proteins to interact with (129). In general, lipid transfer proteins function through extracting lipids from one membrane and transfer them to another membrane (141). For example, the cytosolic lipid transfer protein CERT contains domains that allow for interaction with the Golgi and ER, facilitating the localization of CERT to ER-Golgi MCS (142). Once localized to ER-Golgi MCS, the ceramide binding domain of CERT facilitates the transfer of ceramide from the ER to the Golgi (142).

The transfer of Ca^{2+} across membranes provides a major source of signaling throughout the cell. Thus, intracellular Ca^{2+} levels are carefully regulated through the presence of Ca^{2+}-permeable channels on the plasma membrane and ER. The concentration of Ca^{2+} is kept low in the cytosol, and the ER stores the majority of Ca^{2+} in

23

mammalian cells (143). ER-MCS help to direct Ca^{2+} exchange to maintain Ca^{2+}

homeostasis. For example, ER-plasma membrane MCS play a central role in store-

operated Ca^{2+} entry (144-146). At steady state, the ER Ca^{2+} sensor stromal interaction

molecule 1 (STIM1) is bound to Ca^{2+} and localized to the ER. Upon depletion of ER Ca^{2+}

stores, STIM1 is no longer bound to calcium and oligomerizes and localizes to ER-

plasma membrane MCS (147). At ER-plasma membrane MCS, STIM1 interacts with the

Orai1 Ca^{2+} channel to facilitate the influx of Ca^{2+} and replenish the ER Ca^{2+} store (148).

Formation of ER-containing MCS

Contact sites with the ER are commonly formed through the interaction of the ER-

resident VAP-family proteins with partner proteins on the opposing organelle (149)

(Figure 1.5). Two of the VAP-family proteins, VAPA and VAPB, are highly homologous

and are commonly referred to together as VAP (149). VAP protein interactions play a

role in the formation of a significant proportion of ER-MCS, however the presence of

ER-MCS in the absence of VAP indicated that additional proteins act to form ER-MCS

(150, 151). In line with these observations, recent studies have revealed three new

homologs of VAP, motile sperm domain-containing proteins MOSPD1, MOSPD2, and

MOSPD3, thus adding to the list of VAP-family proteins (152, 153).

The VAP-family proteins are known to interact with FFAT motif containing

proteins. FFAT, two phenylalanines (FF) in an Acidic Tract, motifs are linear peptide

motifs typified by an E_1-F_2-F_3-D_4-A_5-X_6-E_7 consensus core sequence (154, 155). While

most of the seven core elements can have significant derivation from this core sequence,

the residue in position two is considered essential and must be either a phenylalanine (F)

or a tyrosine (Y) (149, 156). Importantly, the core of the FFAT motif is flanked by adjacent acidic residues to create an acidic tract (154). It is increasingly recognized that FFAT motifs can have significant variation (157). Recent work by Di Miatta et al. has identified FFAT motifs where the residue in the fourth position is a phosphorylatable serine or threonine residue, termed Phospho-FFAT motifs, and shown that the phosphorylation of this residue is required to interact with VAP (158). Additionally, MOSPD1 and MOSPD3 have been shown to favor FFAT motifs where the residues flanking the core of the FFAT motif are neutral amino acids rather than acidic and are referred to as FFNT (two phenylalanines (FF) in a Neutral Tract) motifs (153).

ER-Inclusion membrane contact sites

Our lab's work to characterize the molecular composition of ER-Inclusion MCS has shown that ER-inclusion MCS are enriched in *C. trachomatis* Inc proteins and host effectors (Figure 1.6). The *C. trachomatis* Inc protein IncD interacts with the lipid transfer protein CERT, which in turn interacts with VAP on the ER (74, 159). The IncD/CERT/VAP complex is proposed to function in the non-vesicular trafficking of host lipids to the inclusion (74, 126). Depletion of CERT or VAP resulted in a significant decrease in inclusion size and infectious progeny production, indicating the importance of these ER-inclusion MCS during *C. trachomatis* development (74, 126). Another *Chlamydia* Inc protein, IncV, interacts directly with VAP through the presence of two core FFAT motifs and functions as a structural tether between the inclusion and the ER (68). The host ER calcium sensor STIM1 also localizes to ER-inclusion MCS (160).

STIM1 has been proposed to play a role in *C. trachomatis* host cell exit by extrusion (71), however, the role of the STIM1 at ER-inclusion MCS remains unknown.
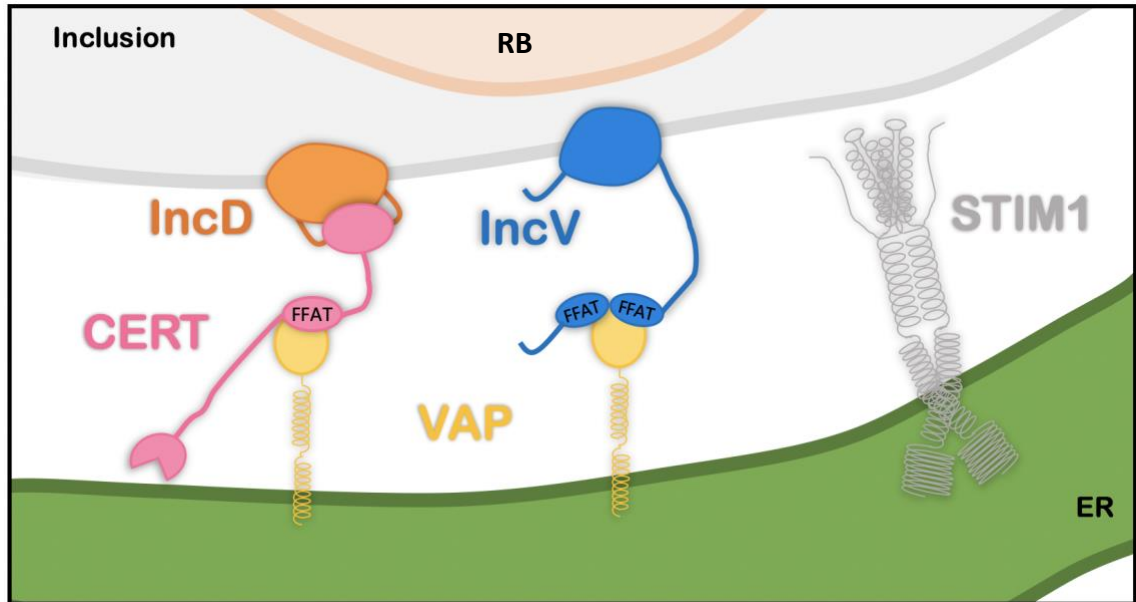
Figure 1.6 Current model of the molecular composition of ER-Inclusion membrane contact sites. The Inc protein IncD (orange) interacts with the lipid transfect protein CERT (pink), which interacts with the ER-resident protein VAP (yellow). The IncD/CERT/VAP complex is purposed to function in lipid acquisition. The Inc protein IncV (blue) also interact with VAP and functions in the tethering of the two organelles. The ER calcium sensor STIM1 (grey) also localizes to ER-inclusion MCS. The function of STIM1 at ER-inclusion MCS is not currently understood. Inclusion, C. trachomatis inclusion (light grey); RB, reticulate body (light orange); ER, endoplasmic reticulum (green). Figure courtesy of Rebecca Murray.

Research Goals and Significance

Overall, my research projects have sought to provide insight into how *C. trachomatis* is able to manipulate the host cell environment in order to establish and maintain a replicative niche, by identifying novel interactions of the inclusion with host factors and elucidating the regulation of a tether at ER-inclusion MCS.

Identification of additional ER-inclusion MCS components could provide important information regarding their molecular composition and further elucidate the role that ER-inclusion MCS play in the chlamydial developmental cycle and pathogenesis. When I started my thesis research, few components of ER-inclusion MCS had been identified, thus my first goal was to isolate and identify novel bacterial and host cell components of ER-Inclusion MCS (Chapter 2).

A proximity labeling screen for ER-inclusion MCS components identified several of host glycolytic enzymes. This potential localization of host glycolytic enzymes to the inclusion was of interest as relatively few studies in the field have addressed the mechanisms by which *Chlamydia* manipulates host cell metabolism. Thus, my second goal was to determine how *Chlamydia* hijacks host metabolism, specifically glycolysis, and shed light on the interplay between host and bacterial metabolism during *C. trachomatis* pathogenesis (Chapter 3).

Lastly, our lab previously identified a complex at ER-Inclusion MCS, consisting of the *Chlamydia* Inc protein IncV and the host ER-resident protein VAP, that is responsible for tethering and maintaining the two organelles in close proximity. My third goal was to characterize the regulation of the IncV-VAP interaction (Chapter 4). Through the characterization of the IncV-VAP interaction we can gain valuable insight into the

mechanisms controlling the formation and maintenance of ER-inclusion MCS. Additionally, since pathogens often co-opt cellular processes, the mechanisms uncovered for the regulation of ER-inclusion MCS may apply to the regulation of cellular MCS.

Overall, my work could contribute to the identification of novel therapeutic targets and combat the blindness and infertility that can arise from chlamydial infections.

Chapter 2:

APEX proximity labeling to identify host and

bacterial factors at ER-Inclusion MCS

All data presented in this chapter generated by R. Ende

Abstract

Our lab has shown that the endoplasmic reticulum (ER) forms membrane contact sites

with the *C. trachomatis* inclusion (ER-inclusion MCS). It is proposed that these contact

sites play a role in the non-vesicular trafficking of host cell lipids to the inclusion, a

process required for proper bacterial growth. However, the overall function of these

contact sites and how they are formed is not well understood. We sought to identify and

characterize the molecular composition of ER-inclusion MCS. Our previous work has

shown that the bacterial protein IncV interacts with the ER resident protein VAP and

overexpression of IncV increases the amount of ER-inclusion MCS per inclusion. We

utilized the IncV-VAP interaction coupled with BioID or APEX2 proximity labeling to

isolate proteins at ER-inclusion MCS. Fusion of BioID to IncV disrupted the catalytic

activity of the BioID proximity labeling enzyme and expression of an IncV-APEX2

fusion protein was not detected. However, a Myc-APEX2-VAPA fusion construct was

recruited to the inclusion membrane in HeLa cells infected with an IncV overexpressing

strain of *C. trachomatis* and was able to biotinylate proteins at the inclusion membrane

when biotin-phenol was provided. Under the same conditions, there was an increase in

biotinylated proteins pulled down with streptavidin beads. Moreover, the Myc-APEX2-

VAPA construct was able to biotinlyate itself and its interacting partner IncV, a known

ER-inclusion MCS component. We were also able to generate an APEX2 proximity

labeling construct using CERT, another known host component of ER-inclusion MCS.

These data were consistent with the APEX system being an effective approach for

isolating novel components of ER-inclusion MCS. Given these results, we performed a

pilot screen comparing the proteomes identified by the VAP and CERT proximity labeling constructs.

Introduction

Our lab has shown that the ER forms membrane contact sites with the *C. trachomatis* inclusion (ER-inclusion MCS) and have characterized several bacterial and host effectors enriched at these contact sites (68, 74, 126, 159). However, the overall function of these contact sites and how they are formed is not well understood. To address these questions, we sought to identify and characterize the proteome of ER-inclusion MCS.

Traditional biochemical approaches, such as affinity purification, can only identify direct interacting partners of a protein of interest and do not allow for global mapping of MCS proteomes. However, proximity labeling approaches allow for the labeling and identification of neighboring as well and interacting proteins and are promising approaches for determining the proteome of MCS (161-163). Proximity labeling approaches rely on the use of enzymes that are capable of catalyzing the transfer of biotin or other derivatives to protein within a certain proximity to the enzyme. These enzymes are fused to a protein of interest to direct the enzyme to a particular subcellular localization and upon addition of exogenous biotin, the enzyme can biotinylate proteins that are interacting with, or in close proximity to, the protein of interest. The biotinylated proteins can then be isolated by streptavidin beads and identified via subsequent mass spectrometry (Figure 2.1).

Currently, the major proximity labeling approaches are BioID and APEX2 (161-163). The BioID approach utilizes a biotin ligase enzyme, BirA, from *E. coli* with a

catalytic site mutation that alters substrate specificity and makes it promiscuous (164, 165). The APEX2 approach utilizes the soybean ascorbate peroxidase enzyme APEX2 (166). Rather than biotin, the substrate biotin-phenol is provided for the APEX2 enzyme (166, 167). In the presence of Hydrogen peroxide, a biotin phenoxyl radical is generated that can then covalently attach to surrounding proteins. The APEX2 approach does possess some key advantages compared to BioID in that the APEX2 enzyme is smaller in size (27 versus 35 kDa) and has a significantly shorter labeling time (minutes versus hours) (167). This faster labeling allows for analysis of more dynamic changes in protein-protein interactions.

Both BioID and APEX2 approaches have been used to identify novel MCS components (168, 169), and both approaches have also been used in the context of *Chlamydia* infection (170-175). The BioID approach has been used to determine if specific eukaryotic proteins are recruited to the chlamydial inclusion and to demonstrate interactions between chlamydial effectors and eukaryotic proteins (170-172). However, because these studies did not use T3SS effectors, it is unknown if fusion of the BioID enzyme can interfere with proper translocation through the chlamydial T3SS. On the other hand, recent studies have successfully utilized Inc-APEX2 fusions to identify potential binding partners of these Inc proteins, define the proteome of the inclusion membrane at different stages developmental cycle, and establish APEX2 as powerful approach to identify protein interactions at the inclusion membrane (173-175). In all of these studies, Inc-APEX2 fusion proteins were shown to be properly translocated by the chlamydial T3SS (173-175). Thus, BioID and APEX2 are promising approaches to identify ER-inclusion MCS components.

We utilized the previously characterized IncV-VAPA tethering interaction at ER-inclusion MCS (68) and BioID or APEX2 proximity labeling approaches to isolate and identify additional bacterial and host cell effectors that localize to *C. trachomatis* ER-inclusion MCS.
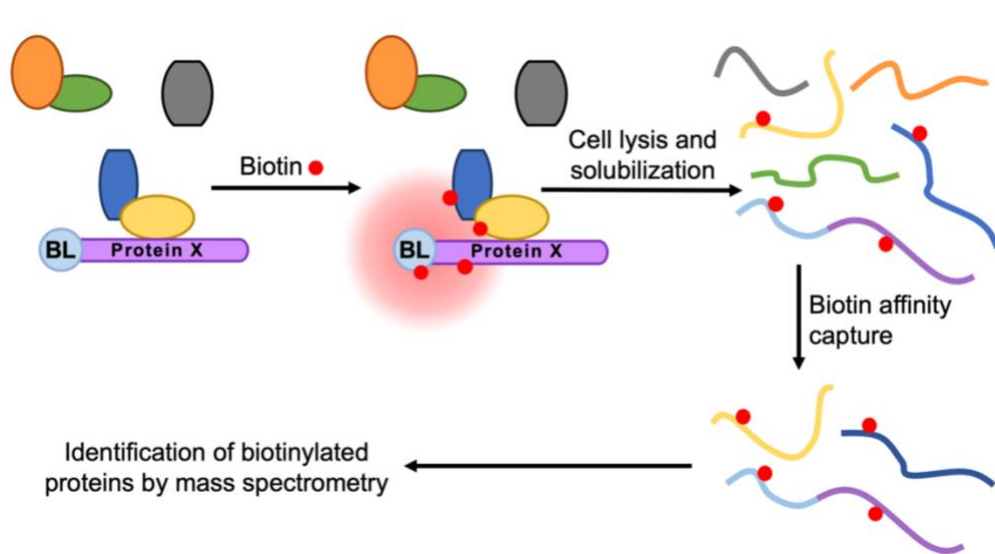
Figure 2.1 Schematic of proximity labeling approach. The expression of a biotin ligase enzyme (BL) fused to a protein of interest (Protein X) results in the biotinylation of proteins interacting with, and proximal to, the protein in interest when exogenous biotin (red dot) is provided. Following cell lysis, biotinylated proteins can be affinity purified and identified by mass spectrometry. Adapted from Roux et al, 2012 courtesy of Clayton Bishop.

Results

In order to isolate and identify novel host and bacterial factors present at ER-inclusion

membrane contact using a proximity labeling approach, we first wanted to identify a

protein of interest that is known to localize to ER-inclusion MCS and would remain

functional after being fused a proximity labeling enzyme. Our lab had previously

identified an interaction between the bacterial Inc protein IncV and the ER-resident

protein VAPA at ER-Inclusion MCS (68). Overexpression of IncV has been shown to

significantly increase the formation of ER-Inclusion MCS (68). Thus, IncV was an ideal

protein of interest, as overexpression of IncV could be used to increase our ability to

identify factors present at ER-inclusion MCS. Fusion of a proximity labeling enzyme

(BioID or APEX2) to IncV, which we refer to as the bacterial effector approach, was the

favored approach due to its specificity to ER-inclusion MCS (Figure 2.2A). As a

complementary approach, we also used a host effector approach where we fused a

proximity labeling enzyme to VAPA, the interacting partner of IncV (Figure 2.2B).
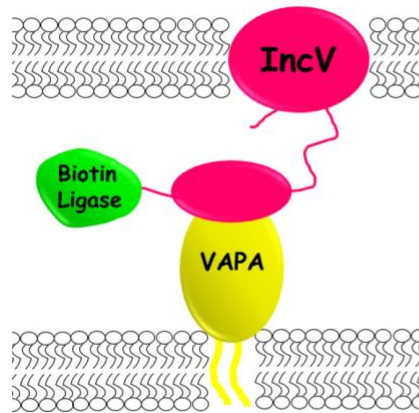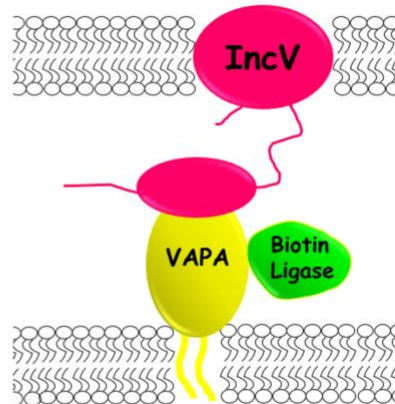
Figure 2.2 Proximity labeling approaches to identify proteins at ER-Inclusion MCS. A) Schematic of the bacterial effector approach of fusing a biotin ligase proximity labeling enzyme (green) to the bacterial effector IncV (Pink). B) Schematic of the host effector approach of attaching a biotin ligase proximity labeling enzyme (green) to the host effector VAPA (yellow).

Bacterial effector approach

An IncV-BioID fusion protein is expressed by *C. trachomatis* and localized to the inclusion membrane

Using the bacterial effector approach, we first determined if an IncV-BirA fusion protein was expressed in *C. trachomatis* and localized to the inclusion membrane. HeLa cells were infected at a MOI of 0.5 with a strain of *C. trachomatis* expressing mCherry constitutively and IncV-BirA-HA under the control of an aTc inducible promoter. At 20h post-infection (pi), IncV-BirA-HA expression was induced by addition of 20ng/mL aTc. At 24h pi, the cells were fixed, immuno-stained with anti-HA antibody, and processed for fluorescence microscopy. Upon induction, IncV-BirA-HA was expressed and localized to the inclusion membrane (Figure 2.3A), indicating that fusion of BirA to IncV did not disrupt expression or proper localization of IncV to the inclusion membrane.

An IncV-BioID fusion protein is biotinylation-deficient

To verify that IncV and the BioID enzyme both remain fully functional following translation fusion, we next determine if IncV-BirA-HA was still able to interact with VAPA and if the BioID enzyme was able to biotinylate proximal proteins. HeLa cells expressing YFP-VAPA were infected with the IncV-BirA-HA overexpressing strain of *C. trachomatis*. At 18h pi, media containing 0.5ng/mL aTc and 50 μM biotin was added. Following overnight incubation with aTc and biotin, the cells were fixed at 24h pi, stained with fluorescent streptavidin labeled conjugate, and processed for fluorescence microscopy. YFP-VAPA was recruited to the inclusion indicating that IncV-BirA-HA was still able to interact with VAPA (Figure 2.3B, middle panel). However, streptavidin

staining to detect biotinylated proteins resulted in no detectable signal, indicating that the

fusion of the BioID enzyme to IncV interfered with the biotinylation of proximal proteins

(Figure 2.3B, right panel).
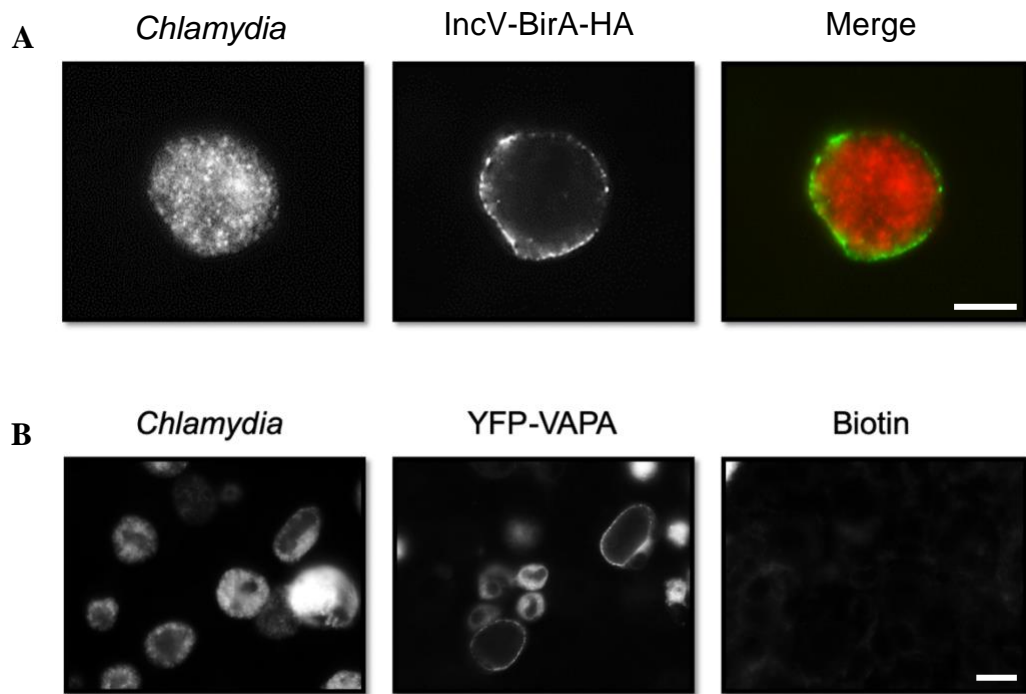
Figure 2.3 Expression and functionality of a *C. trachomatis* IncV-BioID fusion protein. A) Single plane fluorescence micrographs of HeLa cells infected with a *C. trachomatis* strain expressing mCherry constitutively (left panel and red in merge panel) and induced to express IncV-BirA-HA (middle panel and green in merge panel). Scale bar, 5 μm. B) Single plane fluorescence micrographs of HeLa cells expressing YFP-VAPA (middle panel) and infected with a *C. trachomatis* strain expressing mCherry constitutively (left panel), induced to express IncV-BirA-HA, and stained to detect biotinylated proteins (right panel). Scale bar, 10 μm.

Expression of an IncV-APEX fusion protein by *C. trachomatis* is not detected

Since the BioID enzyme was not functional following fusion to IncV, we looked for

alternative proximity labeling enzymes. As previous studies had successfully used Inc-

APEX2 fusion proteins (173-175), we next sought to determine whether an IncV-APEX2

fusion protein was expressed by *C. trachomatis* and localized to the inclusion membrane.

HeLa cells were infected with a strain of *C. trachomatis* expressing mCherry

constitutively and IncV-FLAG-APEX under the control of an aTc inducible promoter. At

20h pi, IncV-FLAG-APEX expression was induced by addition of 20ng/mL aTc. At 24h

pi, the cells were fixed, immuno-stained with anti-FLAG antibody, and processed for

fluorescence microscopy. Following induction, no FLAG signal was detected, indicating

that the IncV-FLAG-APEX2 fusion protein was not being properly synthesized by the

bacteria (Figure 2.4).

Chlamydia	IncV-FLAG-APEX2	Merge
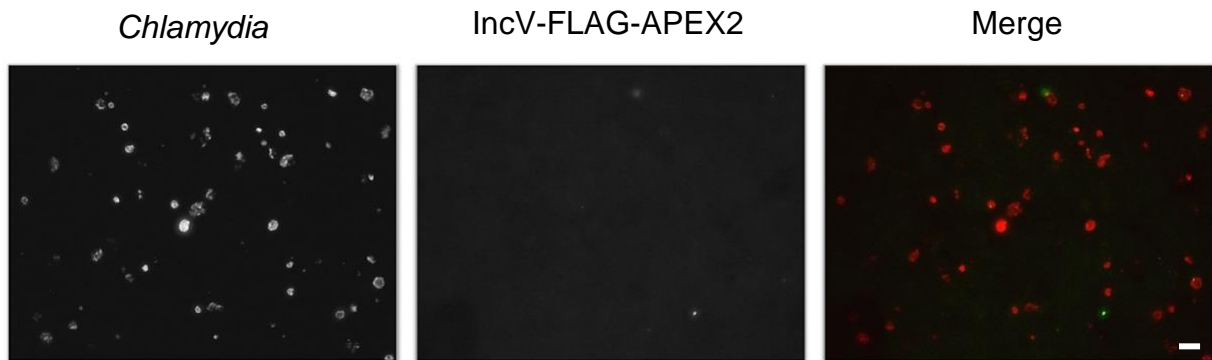
Figure 2.4 Expression of a *C. trachomatis* IncV-APEX fusion protein is not detected. Single plane fluorescence micrographs of HeLa cells infected with a *C. trachomatis* strain expressing mCherry constitutively (left panel and red in merge panel) and induced to express IncV-FLAG-APEX2 (middle panel and green in merge panel). Merge is on the right. Scale bar, 20 μm.

An APEX2-VAPA fusion protein is recruited to the inclusion and biotinylates protein at the inclusion membrane

Using the host effector approach, we first determined if an IncV-APEX fusion protein was recruited to the inclusion membrane and able to biotinylate proximal proteins. HeLa cells expressing Myc-APEX2-VAPA were infected with a strain of *C. trachomatis* expressing mCherry constitutively and IncV-3xFLAG under the control of an aTc inducible promoter. At 20h pi, IncV-3xFLAG expression was induced by addition of 20ng/mL aTc for 4 hours. Following induction, the infected cells were incubated in media containing biotin-phenol for 30 min and biotinylation was catalyzed with hydrogen peroxide as previously described (167, 173). The cells were then fixed, immuno-stained with anti-Myc antibody and fluorescent streptavidin labeled conjugate, and processed for confocal microscopy. The Myc-APEX2-VAPA construct was recruited to the inclusion upon induction of IncV, indicating that the fusion of the APEX2 enzyme did not disrupt the IncV-VAPA interaction (Figure 2.5A, middle panel). Additionally, streptavidin staining revealed the presence of biotinylated proteins at the inclusion membrane, indicating that fusion of the APEX2 enzyme to VAPA did not interfere with APEX2 catalytic function (Figure 2.5A, right panel). Using the same experimental setup as above, except that following fixation the cells were immuno-stained with anti-FLAG antibody to detect IncV, we observed that the signal corresponding to biotinylated proteins appeared to co-localize with IncV at the inclusion membrane (Figure 2.5B). This co-localization with IncV indicated that the Myc-APEX2-VAPA construct could be utilized to biotinylate proteins at ER-Inclusion MCS.

An APEX2-VAPA fusion protein can be used to identify novel components of ER-inclusion MCS

Since the host effector approach resulted in biotinylation of proteins at the inclusion membrane, we next wanted to determine if this approach was biotinylating proteins at ER-inclusion MCS specifically. HeLa cells expressing Myc-APEX2-VAPA were infected with a strain of *C. trachomatis* expressing mCherry constitutively and IncV-3xFLAG under the control of an aTc inducible promoter. At 7h pi, IncV-3xFLAG expression was induced by addition of 0.5ng/mL aTc overnight. At 24h pi, the infected cells were incubated in media containing biotin-phenol for 30 min and biotinylation was catalyzed with hydrogen peroxide as previously described (167, 173). Following biotinylation, the cells were lysed and the lysate was incubated with streptavidin sepharose beads to pulldown biotinylated proteins. The protein-bound beads were then subjected to western blot analysis using, Streptavidin-HRP, anti-Myc antibodies, or anti-FLAG antibodies. As expected, the addition of exogenous biotin resulted in an increase in biotinylated proteins pulled down with streptavidin beads (Figure 2.5C, Streptavidin-HRP). Additionally, the Myc-APEX2-VAPA construct was able to self-biotinylate (Figure 2.5C, αMyc) and biotinylate a known VAP interacting partner, IncV (Figure 2.5C, αFlag). Overall, these results indicated that we were able to successfully isolate biotinylated proteins and that the Myc-APEX2-VAPA construct was able to biotinylate at least two known ER-inclusion MCS components.

Pulldown samples for the condition in which IncV-3xFLAG expression was not induced and no exogenous biotin was provided, and the condition in which IncV-3xFLAG expression is induced and exogenous biotin was provided were then sent for

mass spectrometry analysis to identify the biotinylated proteins (data not shown). In order to increase the specificity of our screen, we also generated a CERT-FLAG-APEX2 construct that is recruited to the inclusion upon overexpression the Inc protein IncD. Since CERT known to interact with IncD at ER-inclusion MCS (74, 159), candidate proteins identified by both the Myc-APEX2-VAPA and the CERT-FLAG-APEX2 constructs have a high likelihood of being ER-inclusion MCS components. The CERT-FLAG-APEX2 construct was shown to be recruited to, and biotinylate proteins at, the inclusion membrane upon overexpression on IncD and samples were sent for mass spectrometry as was done for the Myc-APEX2-VAPA construct (data not shown). Comparison of mass spectrometry results preliminarily identified several host pathways, including several of the host glycolytic enzymes that are further explored in Chapter 3.
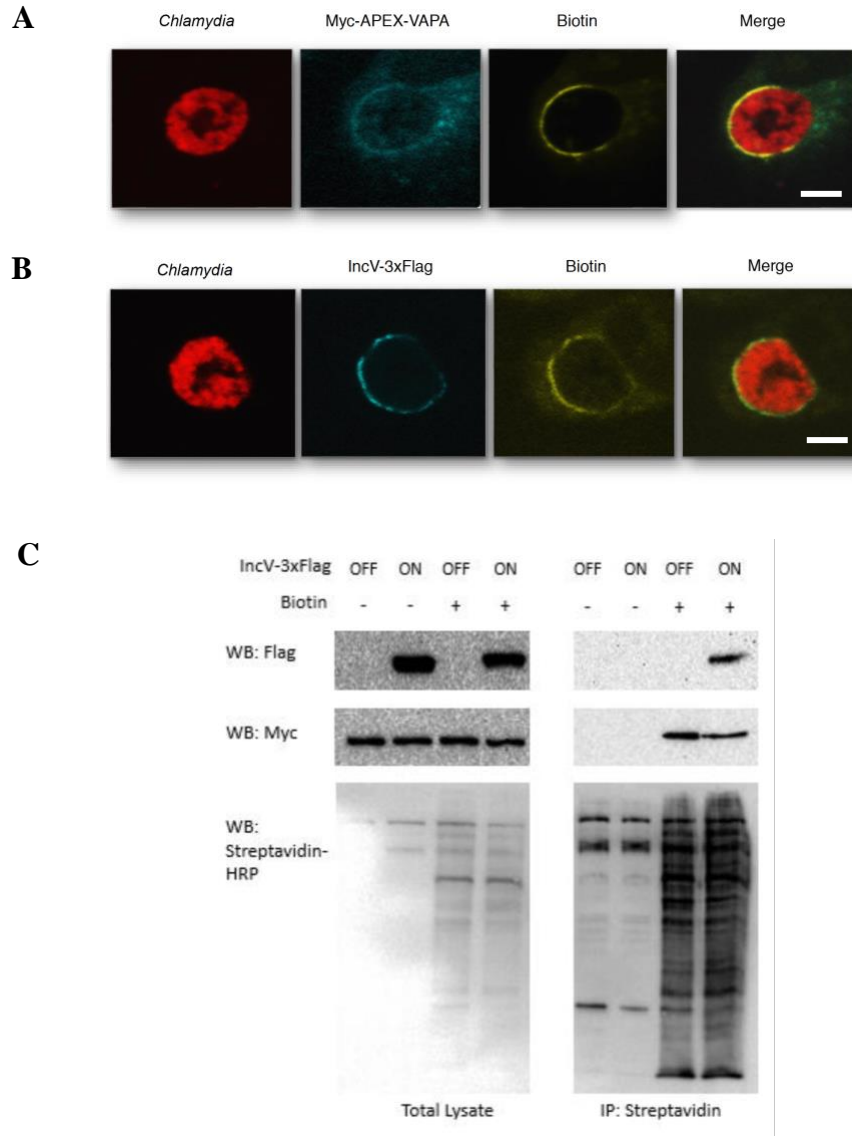
Figure 2.5 A VAP-APEX fusion protein can biotinylate proteins at ER-inclusion MCS. A-B) Single plane confocal micrographs of HeLa cells expressing Myc-VAPA-APEX2 (blue in A) and infected with a *C. trachomatis* strain expressing mCherry constitutively (red), induced to express IncV-3xF (blue in B), and stained to detect biotinylated proteins (yellow). The merged images are shown on the right. Scale bar, 5 μm. C) Pulldown of biotinylated proteins from lysates of HeLa cells expressing Myc-APEX2-VAPA and infected with *C. trachomatis* expressing IncV-3xFlag (ON), or not (OFF) in the presence (+) or absence (-) of exogenous biotin-phenol.

Discussion

Although fusion of the BioID proximity labeling enzyme to IncV was expressed by *C. trachomatis*, localized to the inclusion membrane, and did not disrupt the interaction of IncV with the host protein VAP as previously described (68), we observed that the BioID enzyme was not able to biotinylate proximal proteins (Figure 2.3). We believe that this is most likely due to the topology of the IncV cytosolic domain preventing access to the catalytic site of the proximity labeling enzyme. However, it is difficult to determine exactly how the catalytic activity of the proximity labeling enzymes is being obscured as the topology and function of Inc protein C-terminal domain is not well understood.

As other labs had been successful at generating functional fusions of the APEX2 proximity labeling enzyme with *Chamydia* Inc proteins (173-175), we sought to generate a *C. trachomatis* strain expressing an IncV-APEX2 fusion protein. However, we observed that *C. trachomatis* was not able to express an IncV-APEX2 fusion protein (Figure 2.4). We have not had previous issues with the expression of IncV-3xFLAG fusion proteins by *C. trachomatis*, indicating that fusion of the APEX2 enzyme specifically is interfering with IncV expression. The lack of IncV-APEX2 expression appears to be IncV specific, however only three other Inc proteins have been fused to APEX2. Inc proteins have variation in the timing of their expression during the *Chlamydia* developmental cycle, and this may affect the ability of the different Inc proteins to be expressed as APEX2 fusion proteins (62, 66, 90, 176, 177). Overall, this may indicate that the ability to fuse APEX to Inc proteins may be Inc dependent and will need to be tested on an individual basis.

We were successful in generating APEX2-VAPA and -CERT constructs that were able to localize to, and biotinylate proteins at, the inclusion membrane (Figure 2.4). However, there are caveats to using this host effector approach that must be considered. VAP is a host ER-resident protein that is present throughout the host cell and at membrane contact sites formed between the ER and other host organelles (178), and CERT is a largely cytosolic protein that is also known to localize to ER-Golgi MCS (179, 180). Thus, the VAP- and CERT-APEX2 constructs are not specific to the inclusion and can biotinylate proteins at sites other than ER-Inclusion MCS. By inducing the expression of IncV or IncD and were able to recruit a large portion of the APEX2-VAP or -CERT constructs to the inclusion, effectively increasing the amount of APEX2-VAP and -CERT localized at ER-inclusion MCS (Figure 2.5 A). As a result, the signal corresponding to the biotinylated proteins appeared strongly localized to the inclusion membrane (Figure 2.5 B).

We have increased the specificity of our screen for ER-inclusion MCS components by using two different host effectors known to localize to ER-inclusion MCS. While both VAP and CERT localize to ER-inclusion MCS, they have largely different localizations outside of these membrane contact sites, with VAP localized to the ER and CERT in the cytosol. This allows us to effectively compare the candidates identified by both constructs. Any candidates that were identified by both constructs can be prioritized, while candidates that are only identified in one of the screens can be attributed to VAP or CERT localization outside of ER-inclusion MCS. It is important to note, however, that both the VAP and CERT constructs could identify ER proteins that are not specific to ER-inclusion MCS, as both VAP and CERT can localize to ER- golgi

MCS. Overall, our screen is still rather preliminary and analysis of mass spectrometry results will need to consider that some of the host cell proteins identified will be a result of APEX construct localization outside of ER-inclusion MCS. Thus, identified proteins will need to be validated on an individual basis and the screen repeated and optimized as further discussed in Chapter 5.

Materials and Methods.

Ethics statement.

All genetic manipulations and containment work were approved by the UVA Biosafety Committee and are in compliance with the section III-D-1-a of the National Institutes of Health guidelines for research involving recombinant DNA molecules.

Cell lines and bacterial strains.

HeLa cells (ATCC CCL-2) were maintained in DMEM high glucose (Gibco) containing 10% heat-inactivated fetal bovine serum (Gibco) at 37˚C and 5% CO_2. *Chlamydia trachomatis* Lymphogranuloma venereum, type II (ATCC L2/434/Bu VR-902B) was propagated in HeLa cells as previously described (181). All cell lines and *Chlamydia* strains are routinely tested for mycoplasma contamination.

Plasmid construction.

Inserts were generated by PCR using the primers (IDT) listed in Table 2.1, and the Herculase DNA polymerase (Stratagene). The inserts were cloned as described below using restriction enzymes (NEB) and T4 DNA ligase (NEB).

Vectors for expression in mammalian cells.

The Myc-APEX2-VAPA plasmids was constructed by cloning the APEX2 open reading frame (ORF) into pMyc-BioID-VAPA, using NheI and XhoI restriction sites.

Vectors for expression in *C. trachomatis*.

All the constructs to express the various IncV constructs from the aTc inducible promoter were generated by overlapping PCR and cloned into KpnI and NotI of the p2TK2-SW2 mCh(Gro) vector (182). The Tet-IncV-3xFLAG construct was previously described (68).

***C. trachomatis* transformation.**

Wild type *C. trachomatis* was transformed using our previously described calcium-based *Chlamydia* transformation procedure (182).

DNA transfection.

Cells were transfected with mammalian construct DNA according to manufacturer instructions with X-tremeGENE 9 DNA Transfection Reagent (Roche).

SDS-PAGE.

Biotinylated proteins were purified as described in the immunoprecipitation and protein purification sections then suspended in a final concentration of 1x Laemmli buffer with 10mM DTT. Protein samples were separated using SDS-PAGE.

Immunoblotting.

After SDS/PAGE, proteins were transferred onto nitrocellulose membranes (GE Healthsciences). Prior to blocking, membranes were stained with Ponceau S in 5% acetic acid and washed in dH_2O. Membranes were incubated for 1 hour with shaking at room temperature in blocking buffer (5% skim milk in 1x PBS with 0.05% Tween). Membranes were then incubated with primary and secondary (HRP-conjugated) antibodies diluted in blocking buffer overnight at 4°C and 1 hour at room temperature, respectively, with

shaking. ECL Standard western blotting detection reagents (Amersham) were used to detect HRP-conjugated secondary antibodies on a BioRad ChemiDoc imaging system. For membranes incubated with Streptavidin-HRP conjugates, the blocking buffer contained 5% bovine serum albumin (BSA) instead of skim milk. Membranes were incubated with the Streptavidin-HRP conjugates for one hour and room temperature, shaking, and developed with ECL Standard western blotting detection reagents as described above.

Antibodies.

The following antibodies were used for immunofluorescence microscopy (IF) and immunoblotting (WB): mouse monoclonal anti-FLAG [1:1,000 (IF); 1:10,000 (WB); Sigma], mouse monoclonal anti-Myc [1:1,000 (IF), 1:1,000 (WB), Cell Signaling], mouse monoclonal anti-HA (1:1000 for IF; BioLegend), HRP-conjugated goat anti-mouse IgG [1:10,000 (WB); Jackson], HRP-conjugated Streptavidin [1:2000 for WB; Invitrogen], Alexa Fluor 488-, or Pacific Blue-conjugated goat anti-mouse IgG [1:500 (IF); 1:10,000 (WB); Molecular Probes], Alexa Fluor 488-, or Pacific Blue-conjugated Streptavidin [1:500 (IF); Molecular Probes].

DNA transfections and infections for microscopy.

HeLa cells were seeded onto glass coverslips and transfected with Myc-APEX2-VAPA the following day. 18 hours post-transfection, cells were infected with the indicated strain of *C. trachomatis* at a MOI of 0.5. 7h pi, media containing 0.5ng/mL aTc (final concentration) was added overnight to induce expression of IncV-3xFLAG.

Immunofluorescence and confocal microscopy.

HeLa cells seeded on glass coverslips and infected with *C. trachomatis* were fixed with 4% paraformaldehyde in 1x PBS for 20 minutes at room temperature then washed with 1x

PBS three times. The coverslips were sequentially incubated with primary and secondary antibodies in 0.1% Triton X-100 in 1x PBS for 1 hour at room temperature. Coverslips were washed with 1x PBS three times then mounted with glycerol containing DABCO and Tris pH 8.0.

Non-confocal fluorescent images were obtained with a Nikon epifluorescence microscope. Confocal images were obtained using an Andor iXon ULTRA 888BV EMCCD camera and a Yokogawa CSU-W1 Confocal Scanner Unit attached to a Leica DMi8 microscope. 1 μm thick Z slices covering the entirety of the cell were captured. Image analysis was performed using the Imaris software. All the micrographs within a given figure panels are at the same scale.

Detection of biotinylated proteins

50,000 HeLa cells were seeded onto glass coverslips and transfected with Myc-APEX2-VAPA the following day. 24 hours post-transfection, cells were infected with the indicated strain of *C. trachomatis* at a MOI of 0.5. 20h pi, media containing 20ng/mL aTc (final concentration) was added to induce expression of IncV-3xFLAG. At 24h pi, the infected cells were incubated with 1.5 mM biotinyl-tryamide (biotin-phenol) (Chemodex) for 30 min at 37°C and 5% CO2. At 24.5h pi, biotinylation was catalyzed by the addition of 3 mM H2O2 in PBS for 1 min at RT with gentle rocking. The reaction was quenched by 3 washes at RT with 10 mM sodium ascorbate, 10 mM sodium azide, and 5 mM Trolox in PBS. Coverslips were removed and fixed for immunofluorescence and microscopy.

Purification of biotinylated proteins from cells infected with C. *trachomatis*.

250,000 HeLa cells were seeded into one well of a six-well plate (Falcon) and transfected the following day with Myc-APEX2-VAPA. 24 hours post-transfection, cells were infected

with *C. trachomatis* at a multiplicity of infection (MOI) of 1. 7h pi, media containing 0.5ng/mL anhydrotetracycline (aTc) was added to the infected cells. At 24h pi, the infected cells were incubated with 1.5 mM biotinyl-tryamide (biotin-phenol) (Chemodex) for 30 min at 37°C and 5% CO2. At 24.5h pi, biotinylation was catalyzed by the addition of 3 mM H2O2 in PBS for 1 min at RT with gentle rocking. The reaction was quenched by 3 washes at RT with 10 mM sodium ascorbate, 10 mM sodium azide, and 5 mM Trolox in PBS. The quenching solution was removed and 500μL of lysis buffer (20 mM Tris pH 7.5, 150 mM NaCl, 2 mM EDTA, 1% Triton X-100, protease inhibitor mixture EDTA-free (Roche)) was added per well. Cells were lysed for 20 minutes at 4°C with rotation. Lysates were centrifuged at 16,000xg for 10 minutes at 4°C to pellet nuclei and unlysed cells. Cleared lysates were incubated with 10μL of Streptavidin sepharose beads (GE Healthcare) for 2 hours at 4°C with rotation. The beads were washed with lysis buffer three times. The beads were resuspended in a final concentration 1x Laemmli buffer with 10mM DTT and 0.5mM biotin to elute biotinylated proteins.

Chapter 3:

Host and Bacterial Glycolysis During

Chlamydia trachomatis Infection

This Chapter is a modified version of the previously published article,
"Host and Bacterial Glycolysis during *Chlamydia trachomatis* Infection"
Ende, R. J., & Derré, I. (2020). *Infection and immunity*, *88*(12), e00545-20.

All data presented in this chapter generated by R. Ende

Abstract

With a reduced genome, *C. trachomatis* is dependent on its host for survival, in part due to a need for the host cell to compensate for incomplete bacterial metabolic pathways. However, relatively little is known regarding how *C. trachomatis* is able to hijack host cell metabolism. In this study, we show that two host glycolytic enzymes, Aldolase A and Pyruvate Kinase, as well as Lactate Dehydrogenase, are enriched at the *C. trachomatis* inclusion membrane during infection. Inclusion localization was not species specific, as a similar phenotype was observed with *C. muridarum*. Time course experiments showed that the number of positive inclusions increased throughout the developmental cycle. Additionally, these host enzymes co-localized to the same inclusion and their localization did not appear dependent on sustained bacterial protein synthesis, or intact host actin, vesicular trafficking, or microtubules. Depletion of the host glycolytic enzyme Aldolase A resulted in decreased inclusion size and infectious progeny production, indicating a role for host glycolysis in bacterial growth. Finally, quantitative PCR analysis showed that expression of *C. trachomatis* glycolytic enzymes inversely correlated with host enzymes localization at the inclusion. We discuss potential mechanisms leading to inclusion localization of host glycolytic enzymes and how it could benefit the bacteria. Altogether, our findings provide further insight into the intricate relationship between host and bacterial metabolism during *Chlamydia* infection.

Introduction

As an obligate intracellular pathogen with a small genome (1Mb compared to 5Mb genome of *E. coli*), *C. trachomatis* is strictly dependent on the host cell to complete its developmental cycle. Upon entering epithelial cells, *C. trachomatis* resides within a membranous vacuole, the inclusion. In the lumen of the inclusion, the bacteria undergo a biphasic developmental cycle, alternating between the infectious elementary body (EB) form and the replicative reticulate body (RB) form (27, 28). After entry, the EBs differentiate into RBs and the RBs continue to replicate within the inclusion until the asynchronous differentiation of RBs back to EBs begins approximately 24 h pi (28). The EBs are then released from the host cell through extrusion or host cell lysis, allowing for infection of neighboring cells (33, 34, 94).

It is still unclear how much *C. trachomatis* relies on the host cell for energy production throughout development. For almost 40 years, *C. trachomatis* was thought to be an energy parasite (38-41). However, sequencing of the *C. trachomatis* genome revealed that the bacteria possess components of the electron transport chain and adenosine triphosphate (ATP) synthase complex, suggesting that *C. trachomatis* can drive a minimal electron transport chain to produce ATP through oxidative phosphorylation (37). Additionally, *C. trachomatis* was found to have an intact pentose phosphate pathway and a partial citric acid (TCA) cycle (37, 42). While these findings indicate that *C. trachomatis* is not merely an energy parasite, there is evidence to suggest that *C. trachomatis* is in part dependent on the host cell for energy production. For example, the nucleotide transporters Npt1 and Npt2 are highly expressed in *Chlamydia*

RBs (50, 51), indicating that *Chlamydia* is reliant on scavenging ATP and NAD+ from the host (44, 183).

In addition to oxidative phosphorylation, glycolysis is another major source of cellular energy. Glycolysis relies on the function of 10 different enzymes to sequentially convert glucose into pyruvate and NAD+ to NADH, producing ATP in the process (184). Sequencing of the *C. trachomatis* genome identified a nearly full set of glycolytic enzymes, lacking only the gene for hexokinase, the first enzyme of the pathway responsible for converting glucose to glucose-6-phosphate (37). Instead, glucose-6-phosphate is taken directly from the host cell via the UhpC antiporter produced by *Chlamydia* (43). Heterologous expression of *C. trachomatis* glycolytic enzymes in *E. coli* confirmed their functionality (45). However, the *C. trachomatis* glycolytic enzymes were proposed to be expendable, as saturated ethyl methanesulfonate (EMS) mutagenesis resulted in a loss-of-function mutation in bacterial glucose-6-phosphate isomerase (*pgi*), the enzyme responsible for shuttling glucose-6-phosphate into the glycolytic pathway (46).

More recently, a genome-wide RNA interference screen performed by Rother et al. suggested that two host glycolytic enzymes, glucose-6-phosphate isomerase and 6-phosphofructokinase, were potentially involved in *Chlamydia* progeny production (53). However, these results were not validated. The same study also profiled metabolites of central carbon metabolism following *Chlamydia* infection and observed elevated levels of pyruvate, lactate, and glutamate. An increase of these metabolites is indicative of Warburg metabolism, a metabolic state commonly observed in cancer cells that is characterized by the increased utilization of glycolysis rather than oxidative

phosphorylation, resulting in the increased production of lactate (54-56). In this

metabolic state, the upregulation of glycolysis leads to an accumulation of glycolytic

intermediates that can be shuttled into the pentose phosphate pathway and used for

ribonucleotide synthesis. Thus, Rother et al. concluded that, much like what occurs in

cancer cells, *Chlamydia* is able to shift the host cell into a hypermetabolic state in order

to meet the high energetic demand of bacterial replication. However, whether this

upregulation of host glycolysis is influenced by the localization of host glycolytic

enzymes in relation to the *C. trachomatis* inclusion remains unknown.

In the present study, we showed that several of the host glycolytic enzymes

localized at the inclusion membrane and that the number of positive inclusions increased

as the developmental cycle progressed. Moreover, knockdown of the host glycolytic

enzyme Aldolase A resulted in reduced inclusion size and decreased infectious progeny

production, suggesting a role for host glycolysis in bacterial development. Lastly,

quantitative PCR analysis of *C. trachomatis* glycolytic enzymes showed their down-

regulation throughout the developmental cycle. These novel findings further shed light on

host and bacterial metabolism throughout *Chlamydia* development.

Results

Host glycolytic enzymes localize at the *Chlamydia* inclusion membrane.

In order to investigate how *Chlamydia* hijacks host metabolism, specifically glycolysis,

we generated 3xFLAG-tagged constructs of two host enzymes involved in glycolysis

(Aldolase A and Pyruvate Kinase) and one acting directly on the end product of

glycolysis (Lactate Dehydrogenase) that were originally identified in a preliminary

proximity labeling screen for ER-inclusion MCS components (described in Chapter 2). In HeLa cells transfected with these constructs, the enzymes exhibited diffuse expression throughout the cytosol with enrichment at the leading edge of the cell (Figure 3.1). However, when HeLa cells expressing these constructs were infected with a strain of *C. trachomatis* serovar L2 expressing mCherry (mCherry CtL2) for 24 h, the signal corresponding to the enzymes appeared enriched as a ring around the inclusion (Figure 3.2A). Quantification of this enrichment revealed that the enzymes were enriched by 40% at the inclusion compared to the surrounding cytosol (Figure 3.2B). Moreover, quantification of the number of positive inclusions revealed that, for all three enzymes, 60% of the inclusions were positive (Figure 3.2C).

To determine if the enzymes were localized specifically at the inclusion membrane or simply to the periphery of the inclusion, HeLa cells expressing the 3xFLAG-tagged enzymes were infected with the mCherry CtL2 strain for 24h and stained with the IncA antibody to denote the inclusion membrane (82, 185). Confocal imaging and line intensity scan analysis showed that enrichment of the host glycolytic enzymes overlap with the IncA staining, indicating that the host glycolytic enzymes are localizing at the inclusion membrane (Figure 3.2D and E). Additionally, localization of host glycolytic enzymes extends to other *Chlamydia* species as the 3xFLAG-tagged enzymes were localized at *Chlamydia muridarum* inclusions at 24h pi (Figure 3.2F). Altogether, these results indicate that host glycolytic enzymes are localized at the *Chlamydia* inclusion membrane and that this localization is not species specific.
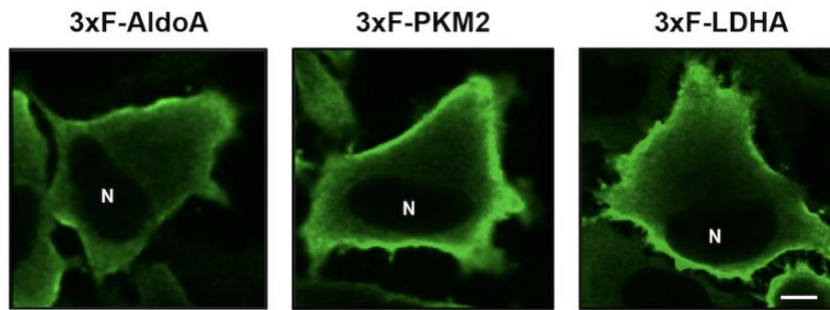
Figure 3.1 Expression of tagged host glycolytic enzymes in uninfected cells. Confocal micrographs of HeLa cells expressing 3xFLAG-tagged Aldolase A (AldoA), Pyruvate Kinase (PKM2), or Lactate Dehydrogenase (LDHA) (green). The cells were fixed at 42 h post-transfection and stained with anti-FLAG antibodies. N: Nucleus. Scale bar: 10µm.
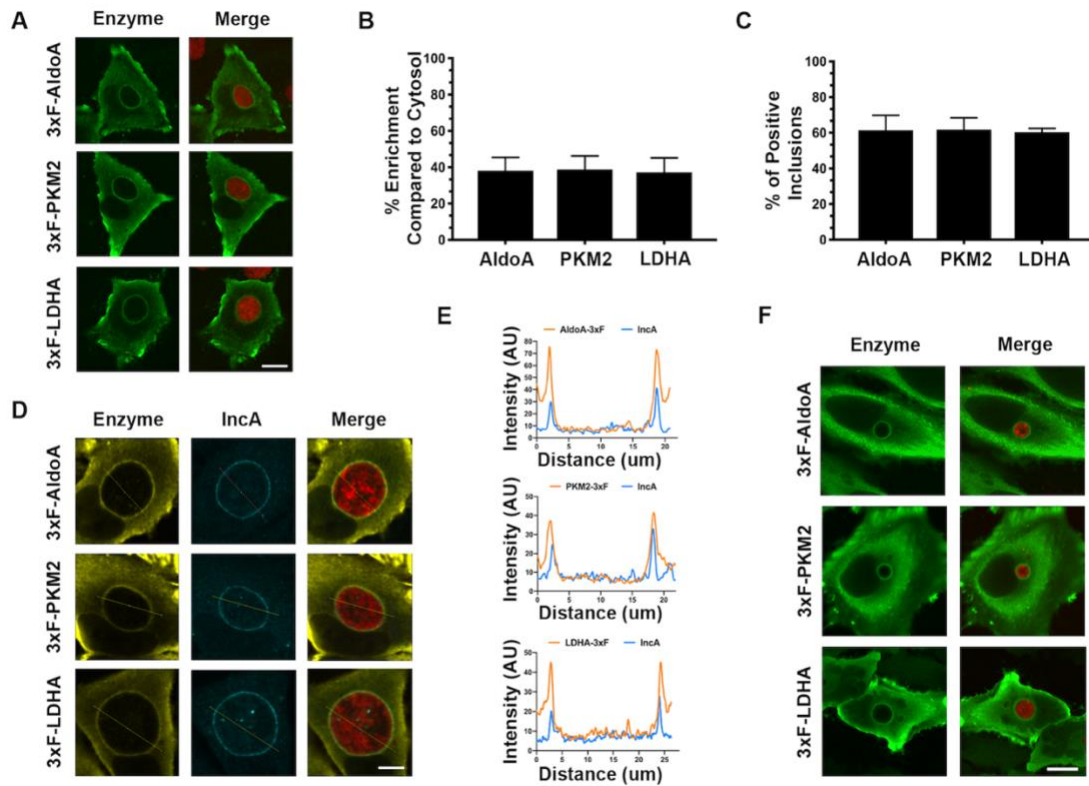
Figure 3.2 Host glycolytic enzymes are enriched at the *Chlamydia* inclusion membrane. (A) Confocal micrographs of HeLa cells expressing 3xFLAG-tagged Aldolase A (3xF-AldoA), Pyruvate Kinase (3xF-PKM2), or Lactate Dehydrogenase (3xF-LDHA), infected for 24 h with the mCherry CtL2 strain (red), and immunostained with anti-FLAG antibodies (green). The merge is shown on the right. Scale bar: 10μm. (B-C) For each of the indicated 3xFLAG-tagged host enzymes, quantification of the percent enrichment at the inclusion (B) and percentage of positive inclusions (C). Quantification methods are described in the Materials and Methods. Data show the mean and standard deviation of a combination of three independent experiments. (D) Confocal micrographs of HeLa cells expressing the indicated 3xFLAG-tagged enzyme, infected for 24 h with the mCherry CtL2 strain (red) and co-immunostained with anti-FLAG (yellow) and anti-IncA (blue) antibodies. The merge is shown on the right. Scale bar: 5μm. (E) Line intensity scan analyses of micrographs depicted in D, indicating the coincidence of 3xFLAG-tagged host enzyme constructs (yellow lines) and the inclusion membrane protein IncA (blue lines). (F) Confocal micrographs of HeLa cells expressing the indicated 3xFLAG-tagged enzyme, infected for 24 h with a *C. muridarum* strain expressing mCherry (red) and stained with anti-FLAG (yellow) antibodies. The merge is on the right. Scale bar: 10μm.

Host glycolytic enzymes localize together at the *C. trachomatis* inclusion membrane.

We next determined if the host glycolytic enzymes were localized together at the same

inclusions. HeLa cells were co-transfected to express both HA tagged Aldolase A and

3xFLAG-tagged Pyruvate kinase, or Lactate Dehydrogenase (Figure 3.3A).

Approximately 60% of inclusions were positive for both the HA- and 3xFLAG-tagged

enzymes, matching the level of localization observed for the individual enzymes in

Figure 3.2C. Less than 10% of inclusions were positive for only one enzyme, while

approximately 30% of inclusions were negative (Figure 3.3B). These results indicate that

host glycolytic enzymes are localized together at the same inclusions.
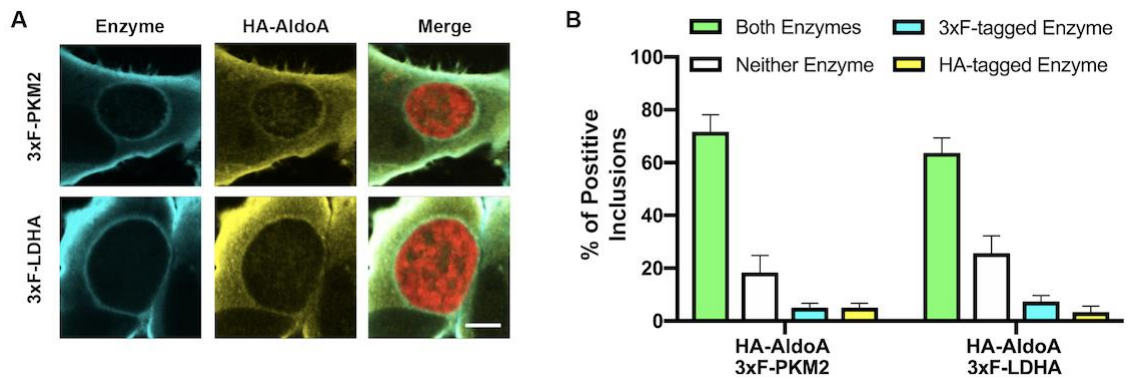
Figure 3.3 Host glycolytic enzymes localize together at the inclusion membrane. (A) Confocal micrographs of HeLa cells co-expressing HA-tagged AldoA (yellow) and 3xFLAG-tagged, PKM2, or LDHA (blue) and infected with the mCherry CtL2 strain (red). The infected cells were fixed at 24h pi and co-immunostained with anti-HA and anti-FLAG antibodies. The merge is shown on the right. Scale bar: 5µm. (B) Quantification of the percentage of inclusions positive for both the HA- and 3xFLAG-tagged enzyme (green bars), neither enzyme (white bars), the 3xFLAG-tagged enzyme alone (cyan bars), or the HA-tagged enzyme alone (yellow bars). Data show the mean and standard deviation of a combination of three independent experiments.
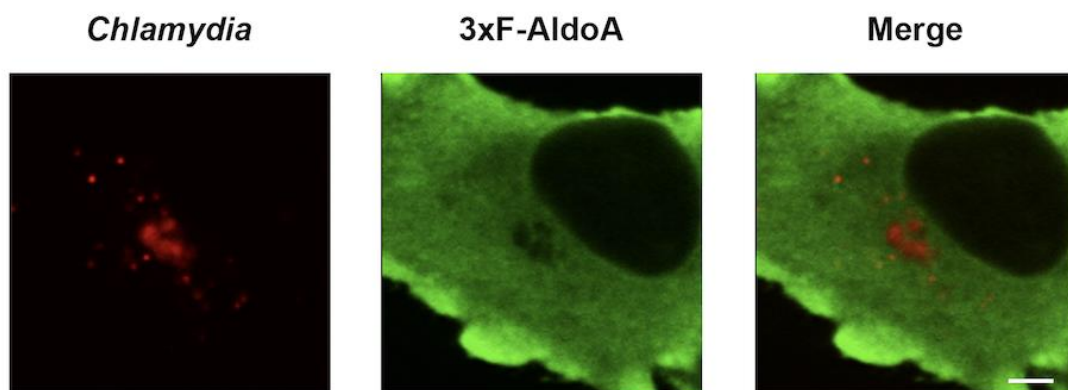
Figure 3.4 Inclusions are negative for Aldolase A at 8h pi. Confocal micrographs of HeLa cells expressing 3xFLAG-tagged Aldolase A (AldoA), infected for 8h with the mCherry CtL2 strain (red), and immunostained with anti-FLAG antibodies (green). The merge is shown on the right. Scale bar: 10µm.

The percentage of Aldolase A positive inclusions increases over time and is not due to nutrient deprivation or sustained *de novo* bacterial protein synthesis.

We next characterized the inclusion localization of the host glycolytic enzymes over time. Since our data showed that all three enzymes behaved similarly (Figure 3.2), we chose to focus on Aldolase A for further experiments. HeLa cells expressing 3xFLAG-Aldolase A were infected with the mCherry CtL2 strain and, at the indicated timepoint (8, 18, 24, or 32 h) pi, the cells were fixed, immunostained with anti-Flag antibodies, and processed for confocal microscopy. Inclusions were negative for Aldolase A at 8h pi (Figure 3.4). However, the number of positive inclusions steadily increased over time, with 48%, 66%, and 81% of inclusions exhibiting inclusion localization at 18, 24, and 32h pi respectively (Figure 3.5A). An increase in the number of positive inclusions over time was still observed when infection was performed in the presence of cycloheximide to inhibit eukaryotic protein synthesis (Figure 3.5A), ruling out that the phenotype was an artifact of increased overexpression of the Aldolase A over time. Moreover, overexpression of two metabolic enzymes involved in the purine biosynthesis pathway, and unrelated to glycolysis, (i.e. GFP-tagged Glycinamide ribonucleotide transformylase (GART) and Phosphoribosylaminoimidazole carboxylase (PAICS)) did not result in inclusion localization of these enzymes (Figure 3.6).

Since we observed an increase in the number of positive inclusions over time, we wondered if this increase could be due to depletion of nutrients as the bacteria and cells continued to grow and divide. To answer this question, HeLa cells expressing 3xFLAG-Aldolase A were infected with the mCherry CtL2 strain for 18 h, at which point nutrients were replenished, or not, by the addition of fresh media. The infected cells were fixed at

24h pi and the number of Aldolase A positive inclusions was determined (Figure 3.5B). If nutrient deprivation played a significant role in host glycolytic enzyme inclusion localization, we expected that at 24h pi, the percentage of positive inclusions in the media replacement condition would be that of an 18h infection. However, the number of positive inclusions did not significantly differ from conditions in which the media was not replaced (Figure 3.5B, 24h vs 24h*).

We next wanted to determine if continuous *de novo* bacterial protein synthesis was required to maintain Aldolase A localization at the inclusion. HeLa cells expressing 3xFLAG-Aldolase A were infected with the mCherry CtL2 strain for 24 h followed by 8 h of treatment with 40 µg/ml chloramphenicol to halt bacterial protein synthesis. At 32h pi, the cells were fixed and processed for confocal microscopy. Untreated cells, fixed at 24h pi, served as a control. Treatment with chloramphenicol did not result in a decrease in the number of positive inclusions compared to the untreated control (Figure 3.5C). Together, these results indicate that the number of Aldolase A positive inclusions increases throughout the development cycle and that this increase is not due to the depletion of nutrients. Moreover, continuous *de novo* bacterial protein synthesis is not required for sustained localization of Aldolase A at the inclusion.
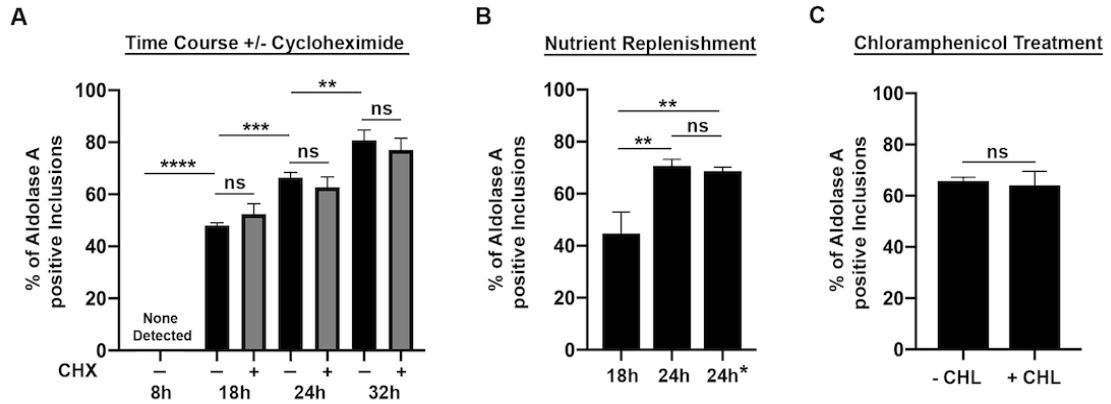
Figure 3.5 The percentage of Aldolase A positive inclusions increases over time and is not due to nutrient deprivation or sustained de novo bacterial protein synthesis. HeLa cells expressing 3xFLAG-tagged AldoA were infected with the mCherry CtL2 strain then fixed and stained with anti-FLAG antibodies at the indicated time pi. (A) Quantification of the percentage of inclusions positive for 3xFLAG-AldoA at 8, 18, 24, and 32h pi in the absence or presence of 1µg/mL Cycloheximide (CHX). (B) Quantification of the percentage of 3xFLAG-AldoA positive inclusions at 18h, 24h, or 24h pi with media replacement at 18h pi (24*). (C) Quantification of the percentage of 3xFLAG-AldoA positive inclusions at 24h pi (- CHL) or, following an additional 8h incubation with 40µg/mL chloramphenicol and fixed at 32h pi (+ CHL). Data show the mean and standard deviation of a combination of three independent experiments. **$P < 0.01$, *** $P < 0.001$, ****$P < 0.0001$, ns: not statistically significant. Student's t-test (Shapiro-Wilk normality test) or one-way ANOVA with multiple comparisons.
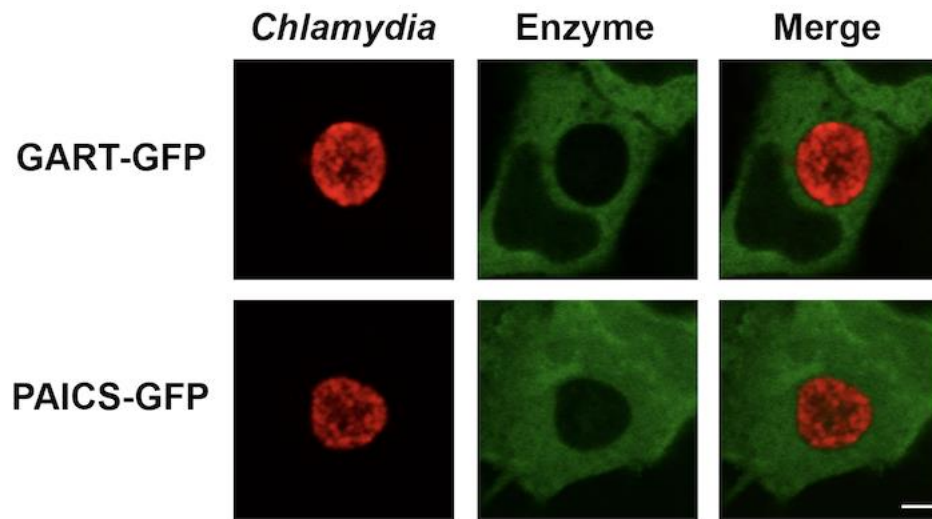
Figure 3.6 GFP-tagged purine biosynthesis enzymes do not localize at the inclusion membrane. Representative confocal micrographs of HeLa cells expressing GFP-tagged Glycinamide ribonucleotide transformylase (GART) or Phosphoribosylaminoimidazole carboxylase (PAICS) (green) and infected for 24 h with the mCherry CtL2 strain (red). No inclusion localization was detected for these constructs. The merge is shown on the right. Scale bar: 5μm.

F-actin, host cell microtubule dynamics, and vesicular trafficking do not play a role in Aldolase A localization at the inclusion.

Since sustained active bacterial protein synthesis did not appear to play a role in Aldolase A localization at the inclusion, we tested if host cell factors were responsible. Aldolase A has been previously shown to bind F-actin (186, 187). It has also been shown that *Chlamydia* inclusions are encased within a cage of F-actin filaments (107). To determine if host cell actin played a role in Aldolase A localization at the inclusion, HeLa cells expressing 3xFLAG-Aldolase A were infected with the mCherry CtL2 strain. At 23.5h pi, infected cells were incubated with or without Cytochalasin D to inhibit actin polymerization (Figure 3.8A). The cells were fixed at 24h pi, immunostained with anti-Flag antibodies, and the percentage of Aldolase A positive inclusions was determined. Treatment with Cytochalasin D did not significantly decrease the percentage of positive inclusions (Figure 3.7A). However, Cytochalasin D can affect cell morphology and have a confounding effect on quantification. Thus, we addressed a possible role for actin with two additional approaches. First, we utilized the R42A and R148A mutants of Aldolase A that have been previously shown to have minimal binding to F-actin (187). HeLa cells expressing either WT, R42A, or R148A Aldolase A were infected with the mCherry CtL2 strain. At 24h pi, the cells were fixed, immunostained with anti-Flag antibodies, and imaged by confocal microscopy (Figure 3.9A). The R42A and R148A mutants did not result in a significant decrease in the percentage of positive inclusions compared to the WT enzyme (Figure 3.7B). Second, we tested if actin cage formation is required for localization of Aldolase A to the inclusion by using an *inaC::aadA* mutant strain of *C. trachomtais*. It was previously shown that the bacterial inclusion membrane protein InaC

modulates F-actin assembly around the inclusion, and that *inaC* mutant inclusions lack

actin cages (46, 105). Aldolase A still localized to *inaC::aadA* mutant inclusions (Figure

3.9B) and no significant difference in the percentage of positive inclusions was observed

between WT and *inaC::aadA* mutant inclusions (Figure 3.7C). Next, we addressed

whether other major host cell factors could be mediating the localization of Aldolase A at

the inclusion. Short treatment with Nocodazole to inhibit microtubule polymerization

(Figure 3.8B) or overnight treatment with Brefeldin A to inhibit vesicular trafficking

(Figure 3.8C) had no observable effect on the percentage of inclusions positive for

Aldolase A (Figure 3.7D and E). Altogether, these results indicate that the actin

cytoskeleton or microtubules are not required for sustained localization of Aldolase A at

the inclusion and that vesicular trafficking or the *Chlamydia* actin cage do not mediate

the inclusion localization of Aldolase A.
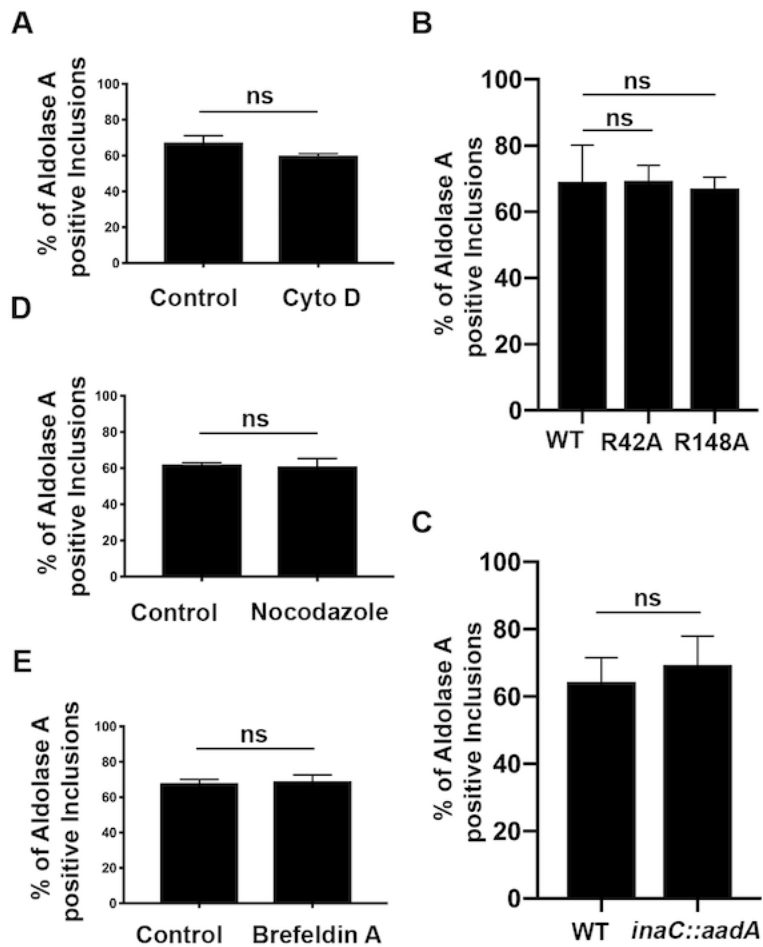
Figure 3.7 F-actin, host cell microtubule dynamics, and vesicular trafficking do not play a role in the localization of Aldolase A at the inclusion. HeLa cells expressing 3xFLAG-AldoA and infected with the mCherry CtL2 strain were fixed at 24h pi and immunostained with anti-FLAG antibodies. (A, D, E) Quantification of the percentage of inclusions postive for 3xFLAG-AldoA following treatment with 1µM Cytochalasin D (Cyto D) at 23.5h pi (A), 33µM Nocodazole at 23.5h pi (D), or 1µg/mL Brefeldin A at 6h pi (E). (B) Quantification of the percentage of inclusions postive for 3xFLAG- AldoA in HeLa cells expressing wild-type 3xFLAG-AldoA (WT), or point mutants no longer able to bind actin 3xFLAG-R42A AldoA (R42A) and 3xFLAG-R148A AldoA (R148A). (C) Quantification of the percentage of inclusions positive for 3xFLAG-AldoA in HeLa cells infected with wild-type C. trachomatis (WT) or an *inaC* mutant strain (*inaC::aadA*). Data show the mean and standard deviation of a combination of three independent experiments. ns: not statistically significant (Shapiro-Wilk normality test, Students t-test).
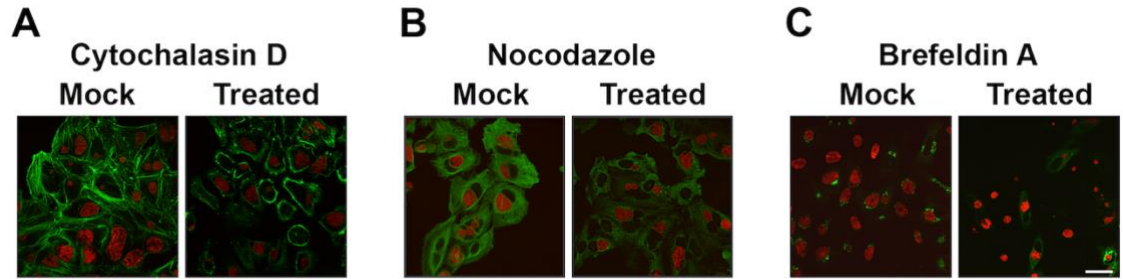
Figure 3.8 Validation of Cytochalasin D, Brefeldin A, and Nocodazole drug treatments. (A) Confocal micrographs of HeLa cells infected with the mCherry CtL2 strain (red) and fixed at 24 h pi following the absence (Mock, left panel) or presence of 1μM Cytochalasin D at 23.5h pi (Treated, right panel) and immunostained with Phalloidin (green). (B) Confocal micrographs of HeLa cells infected with the mCherry CtL2 strain (red) and fixed at 24h pi following the absence (Mock, left panel) or presence of 33μM Nocodazole at 23.5h pi (Treated, right panel) and immunostained with anti-α-tubulin antibodies (green). (C) Confocal micrographs of HeLa cells expressing YFP-Golgi (green), infected with the mCherry CtL2 strain (red), and fixed at 24h pi following the absence (Mock, left panel) or presence of 1μg/mL Brefeldin A at 6h pi (Treated, right panel). Scale bar: 20μm.
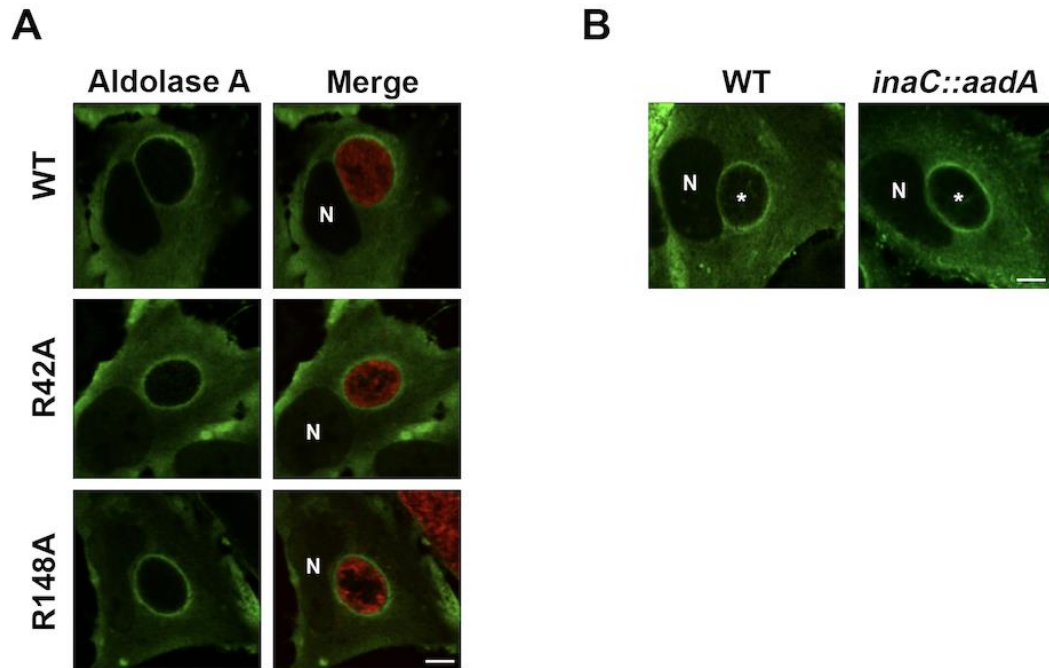
Figure 3.9 Host actin does not affect localization of Aldolase A at the inclusion membrane.
(A) Confocal micrographs of HeLa cells expressing wild-type 3xFLAG-AldoA (WT, top panels),
or point mutants no longer able to bind actin 3xFLAG-R42A AldoA (R42A, middle panels) and
3xFLAG-R148A AldoA (R148A, bottom panels) (green), infected with the mCherry CtL2 strain
(red) and fixed at 24h pi. (B) Confocal micrographs of HeLa cells expressing 3xFLAG-AldoA
(green) and infected with wild-type *C. trachomatis* (WT, left panel) or an *inaC* mutant strain
(*inaC::aadA,* right panel) that were fixed at 24h pi. The asterisk indicates the inclusion. N:
Nucleus. Scale bar: 10μm.

Aldolase A confers a developmental advantage to *C. trachomatis*.

To determine if Aldolase A played a role in *C. trachomatis* intracellular growth and development, we first assessed whether Aldolase A inclusion localization was associated with larger inclusion size. HeLa cells expressing 3xFLAG-Aldolase A were infected with the mCherry CtL2 strain. At 24h pi, the cells were fixed, immunostained with anti-Flag antibodies, and the size of Aldolase A positive and negative inclusions was determined. Aldolase A positive inclusions were significantly larger than Aldolase A negative inclusions (Figure 3.10A).

We next assessed whether depletion of host Aldolase A had an impact on *C. trachomatis* intracellular growth or infectious progeny production. Aldolase A was depleted by 4 independent siRNA duplexes, each of which exhibited greater than 90% efficacy of Aldolase knockdown (Figure 3.10B). Although duplex 2 exhibited over 90% efficacy, it was consistently the least efficient of the duplexes. In order to determine the effect of host Aldolase A depletion on inclusion establishment and bacterial replication, we assessed inclusion size. HeLa cells were treated with independent siRNA duplexes for three days prior to infection with the mCherry CtL2 strain. At 32h pi, the cells were fixed, imaged, and inclusion size was determined by computer-assisted image analysis. We noted that Aldolase A depletion affected cell number, and since cell density affects the multiplicity of infection and inclusion size, each siRNA duplex condition was matched to a control with equal cell number. Compared to mock treated cells, Aldolase A depletion lead to a significant, albeit modest, decrease in inclusion size for 3 of the 4 independent Aldolase A siRNA duplexes (duplex 1, duplex 3, and duplex 4) (Figure 3.10C).

Next, we wanted to determine if depletion of host Aldolase A affected infectious progeny production. HeLa cells depleted of host Aldolase A were infected with the mCherry CtL2 strain for 48 h. At 48h pi, lysates from infected cells were used to infect a fresh monolayer of HeLa cells to determine the number of infectious bacteria. The number of infectious bacteria recovered at 48h pi was significantly reduced following Aldolase A depletion compared to mock treated cells (Figure 3.10D). We note that AldoA siRNA duplex 2 did not significantly decrease inclusion size and had the smallest impact on infectious progeny production. We attribute this to the lower efficacy of this duplex compared to the other three. Nonetheless, we observed significant decrease in inclusion size and infectious progeny production with 3 independent siRNA duplexes, indicating that the observed phenotypes are specifically due to Aldolase A depletion. Altogether, our data shows that host Aldolase A plays a role in inclusion development and infectious progeny production, suggesting that host glycolysis is important for *C. trachomatis* intracellular growth.
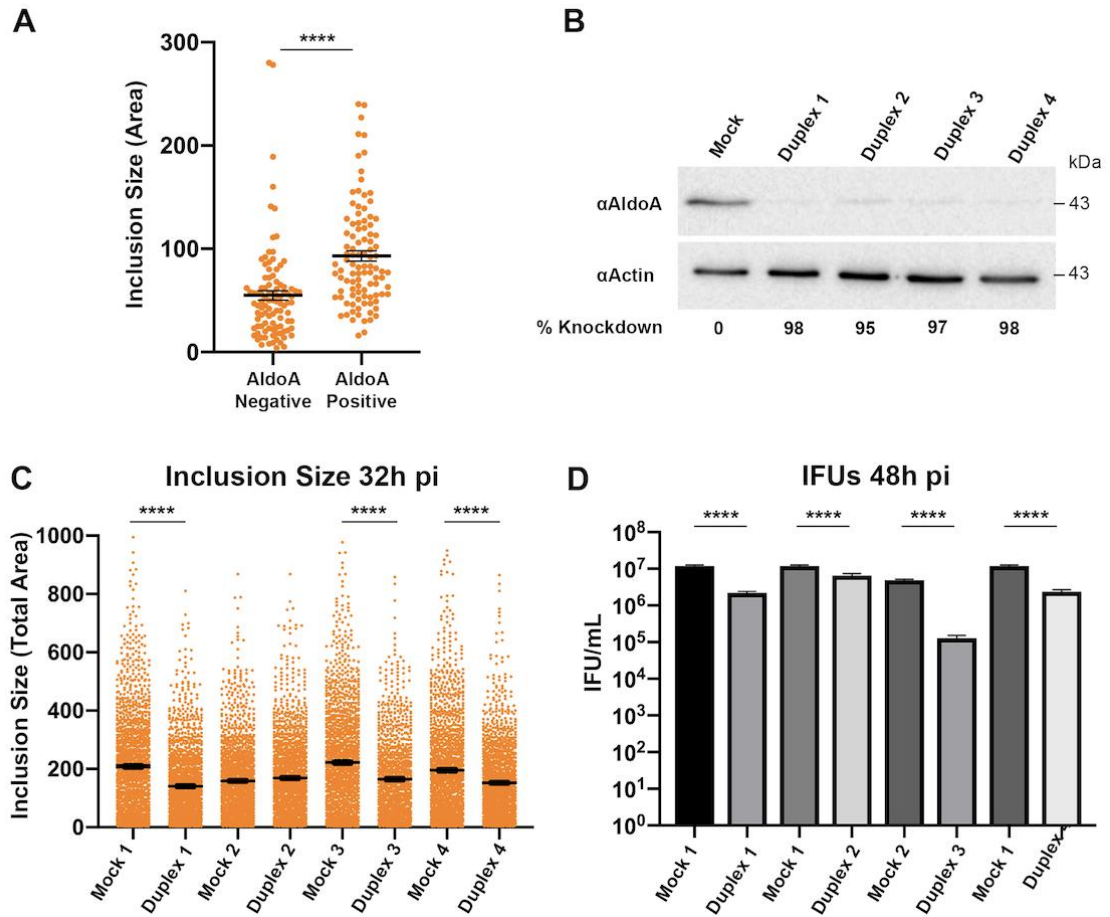
Figure 3.10 Aldolase A confers a developmental advantage to *C. trachomatis*. (A) HeLa cells expressing 3xFLAG-tagged AldoA were infected with the mCherry CtL2 strain and the area of 3xFLAG-AldoA positive and negative inclusions (Arbitrary Units, each circle represents data from a single inclusion) was quantified at 24h pi. (B-D) HeLa cells were transfected with individual Aldolase A siRNA duplexes or siRNA buffer alone (Mock) for 3 days. (B) Immuno-blots of the corresponding lysates were probed using antibodies against endogenous Aldolase A (top blot) and actin (bottom blot). The knockdown efficacy of each duplex targeting Aldolase A is indicated. (C-D) HeLa cells treated with the indicated siRNA duplexes targeting Aldolase A were infected with *C. trachomatis*. For each condition, the total area of the inclusions (Arbitrary Units, each circle represents data from a single inclusion) at 32h pi (C) and the number of infectious bacteria (IFUs/mL) at 48h pi (D) was determined. The cell density of the mock treated conditions was matched to the cell density of the siRNA treated conditions. Data in A show the mean and SEM of a representative experiment. Data in C show the mean and SEM of a combination of three independent experiments. Data shown in D is a representative experiment. Error bars are Standard Deviation. ****P < 0.0001 (Student's t-test).

Bacterial glycolytic enzyme expression is decreased during development.

Having shown that host glycolytic enzymes play a role in *C. trachomatis* intracellular

growth, and knowing that *C. trachomatis* possesses its own glycolytic enzymes, we

wanted to determine the pattern of bacterial glycolytic enzyme expression throughout

infection. Three bacterial glycolytic enzymes, Glucose-6-Phosphate Isomerase (*pgi*),

Fructose-bisphosphate aldolase (*dhnA*), and Pyruvate Kinase (*pykF*), were selected based

on their respective positions at the beginning, middle and end of the glycolytic pathway.

The mid- to late-cycle gene *omcA* served as a control. Gene expression of the bacterial

enzymes was measured at 8, 12, 24, 36, and 48h pi by quantitative reverse transcription

PCR (RT-qPCR). The expression of each gene was normalized to *Chlamydia* 16S

ribosomal RNA (rRNA) and relative to expression at 8h pi. As expected, *omcA*

expression was strongly upregulated at 36 and 48h pi (Figure 3.11, *omcA*). Although gene

expression of the bacterial glycolytic enzymes was detected throughout the time course of

infection, the mRNA levels of all three enzymes were significantly decreased over time

(Figure 3.11, *pgi*, *dhnA*, *pykF*). Interestingly, the decreased gene expression of bacterial

glycolytic enzymes over time correlated with the increase in the number of inclusions

that were positive for the host glycolytic enzyme Aldolase A (Figure 3.5A).
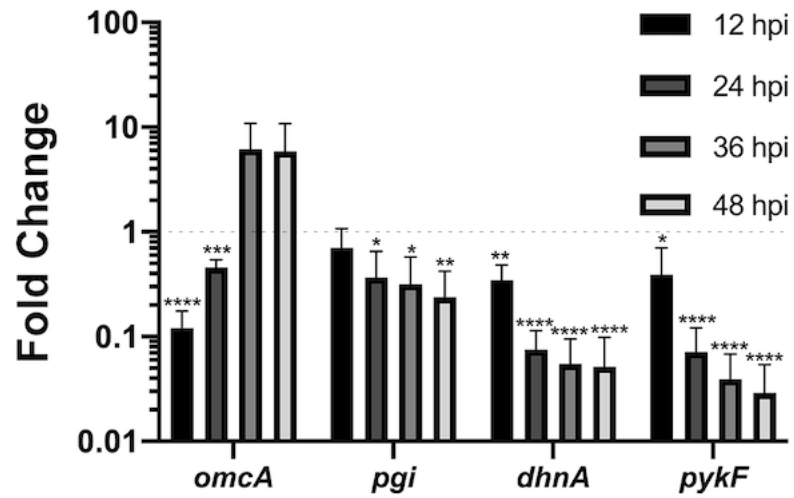
Figure 3.11 *Chlamydia* glycolytic enzyme mRNA levels are decreased during development.
Relative gene expression, determined by RT-qPCR, of a subset of *C. trachomatis* glycolytic
enzymes (Glucose-6-Phosphate Isomerase, *pgi*; Aldolase A, *dhnA*; Pyruvate Kinase, *pykF*) at 12,
24, 36, and 48h pi of HeLa cells. Gene expression was normalized to 16S rRNA levels and the
expression at 8h pi (dotted line). The late expressed gene encoding the outer membrane protein
OmcA (*omcA*) was included as a control. Y axis is a log scale. Data show the mean and standard
deviation of a combination of three independent experiments. *$P < 0.05$, **$P < 0.01$, *** $P <$
0.001, ****$P < 0.0001$ (Student's t-test comparing to 8h pi).

Discussion

Host glycolytic enzymes support *C. trachomatis* intracellular growth and replication.

In the present study, we showed that Aldolase A positive inclusions were significantly larger than Aldolase A negative inclusions and that depletion of host Aldolase A resulted in smaller inclusions and decreased infectious progeny production (Figure 3.10). These results suggest that the specific inclusion localization of Aldolase A is beneficial for *C. trachomatis*, however, we cannot rule out that Aldolase A function in general (i.e. Glycolysis) is responsible for the phenotype observed. Determining if an siRNA-resistant form of Aldolase A targeted to specific organelles or the plasma membrane can rescue the growth defect could address this question.

In line with our results, a recent study described a genome-wide RNA interference screen to identify host factors essential for *C. trachomatis* growth and identified the host glycolytic enzymes glucose-6-phosphate isomerase and phosphofructokinase as high confidence hits in the primary screen (53). Although not validated, these results further support the reliance of *C. trachomatis* on host glycolysis for propagation and growth. Moreover, systematic depletion of glycolytic enzymes will be required to unequivocally determine that host glycolysis is essential for *Chlamydia* intracellular development. The same study also profiled metabolites of central carbon metabolism and observed upregulation of pyruvate, lactate, and glutamate, features indicative of Warburg metabolism (54-56). During Warburg metabolism, pyruvate is converted into lactate and glycolytic intermediates are shuttled into the pentose phosphate pathway where they are converted to ribonucleotides. Thus, Rother et al. suggested that by shifting the cell into this hypermetabolic state, *C. trachomatis* is effectively forcing the host cell to generate

anabolic substrates that the bacteria can then scavenge from the host. This was supported by the observed upregulation of carbon flux through the pentose phosphate pathway upon *C. trachomatis* infection. The authors concluded that *C. trachomatis* is able to modulate host cell metabolism in order to meet the high energetic demand of bacterial replication.

Localization of host glycolytic enzymes at the inclusion membrane.

We showed that at least three different glycolytic enzymes localized at the *Chlamydia* inclusion (Figure 3.2). One of the limitations of our study is the overexpression of tagged constructs. While antibodies against eukaryotic glycolytic enzymes are widely available and successfully detect their targets via Western Blot, we were unable to determine the conditions that would allow for detection by immunofluorescence. This technical limitation precluded us from performing an important control and validating that endogenous enzymes localize at the *Chlamydia* inclusion. However, our results are strengthened by the fact that inclusion localization did not extend to other enzymes outside of the glycolytic pathway (Figure 3.6) and was not a result of increased expression of the construct over time (Figure 3.5A).

Our data also indicate that enzymes localized together at the same inclusions (Figure 3.3). The co-localization of multiple glycolytic enzymes is in line with the hypothesis that glycolytic enzymes form localized, multi-enzyme complexes. Although this hypothesis has existed for many years (188), it has lacked direct experimental evidence (189, 190). More recently, a model in which three separate glycolytic subcomplexes come together to form an active glycolytic complex has been proposed (191) and supports a dynamic complex formation.

Further supporting glycolytic enzyme complex formation, Kinetoplastid parasites, such as *Trypanosoma brucei*, possesses a glycosome, a membrane-bound organelle that specifically contains the majority of the enzymes of the glycolytic pathway (192-194). Glycosomes, and hence the compartmentalization of glycolytic enzymes, has also been shown to be essential for trypanosomatid metabolic regulation and viability (195). These glycosomes provide evidence that the compartmentalization of glycolytic enzymes can be advantageous to survival within a host. Although the localization of host glycolytic enzymes at the inclusion likely differs from that of the glycosomes, in that the glycolytic enzymes are not clustered within small membrane bound organelles, it is possible that the host enzymes may become bound to the surface of the inclusion membrane or associate with inclusion bound factors.

Additionally, work by Jang et al. demonstrated that under conditions of energy depletion or high energetic demand, the glycolytic enzymes of *C. elegans* neurons redistribute from a diffuse cytosolic localization to puncta localized to the presynaptic sites of neurons (196). Moreover, disrupting the localization of the glycolytic enzyme phosphofructokinase to the presynaptic sites fails to restore a phosphofructokinase mutant phenotype, indicating that localization of glycolytic enzymes to the presynaptic sites of neuron is necessary to meet the energy demands at *C. elegans* synapses. Similarly, the localization, and thus compartmentalization, of glycolytic enzymes at the *C. trachomatis* inclusion membrane could facilitate efficient channeling of substrates through the sequential enzymes of the pathway.

Mechanism of host glycolytic enzyme localization at the inclusion.

In the present study, we inhibited three major host cells factors that could be reasonable contributors to host glycolytic enzyme localization at the inclusion, the actin cytoskeleton, microtubules, and vesicular trafficking. Based on our results, we ruled out a role for the *Chlamydia* actin cage and for vesicular trafficking (Figure 3.7B, C and E). Moreover, host cell actin and microtubules were not necessary for sustained localization at the inclusion membrane (Figure 3.7A and D).

The results presented in Figure 3.5C indicate that sustained bacterial protein synthesis is not necessary to maintain inclusion localization of Aldolase A. However, it is possible that treatment with chloramphenicol at 24h pi may not affect the involvement of stable bacterial factors synthesized prior to treatment. Unfortunately, because Aldolase A did not localize to the inclusion at early time points (Figure 3.5A, Figure 3.4) and because inhibition of bacterial protein synthesis would halt the developmental cycle, this hypothesis could not be tested. Of particular interest would be the Inclusion membrane proteins (Incs), a family of *C. trachomatis* T3SS translocated effector proteins that are inserted into the inclusion membrane to allow for the interaction of the inclusion with host molecules and organelles (46, 68, 71, 74-76, 79, 94-99, 101, 114, 159, 197, 198).

A pulldown of 3xFLAG-tagged Pyruvate Kinase or Aldolase A to identify interacting partners that could play a role in inclusion localization of the host glycolytic enzymes did not identify any candidates (data not shown). However, we have only tested two of the glycolytic enzymes, and given that the enzymes could form individual subcomplexes that come together through interaction of these subcomplexes (191), it is difficult to predict which of the host enzymes could be interacting with bacterial and/or host factors at the inclusion. Therefore, testing each of the host glycolytic enzymes

systematically would be necessary to completely rule out a role for bacterial and/or host factors in the localization of host glycolytic enzymes at the inclusion.

Finally, it is also possible that inclusion localization of the enzymes is not actively mediated by inclusion localized bacterial or host factors. This hypothesis is harder to test because the cell biology of the glycolytic pathway has not been investigated and the tools are underdeveloped. However, one could envision a host response, where sensing of the depletion of glycolytic substrates (discussed below) in the proximity of the inclusion brings the host glycolytic enzymes together.

Potential role for host glycolytic enzyme localization at the *Chlamydia* inclusion.
The mRNA levels of *C. trachomatis* glycolytic enzymes were significantly decreased past 24h pi (Figure 3.11), when RBs are known to asynchronously transition into EBs (182, 199). The overall decrease in mRNA of bacterial glycolytic enzymes at mid-developmental cycle is consistent with previous RT- and quantitative RT-PCR data (45, 200). However, we do note that our data differ from previous publications in that we saw the highest level of gene expression at 8h pi rather than 24h pi. These differences could be due to differences in cell lines and normalization conditions used. Moreover, the reduced levels of mRNA are in line with the quantitative measurements of *C. trachomatis* encoded glycolytic enzymes indicating that they are more abundant in RBs than EBs (50). If the abundance of bacterial glycolytic enzymes is indicative of the pathway's activity, the above results would suggest that RBs rely more on bacterial glycolytic pathway than EBs. However, this hypothesis would have to be reconciled with the energy source requirements of purified RBs and EBs in axenic media, where RBs exclusively

used ATP and EBs preferentially required G6P, suggesting that RB are not reliant on substrate level phosphorylation and scavenge ATP from the host (52). One possibility is that energy source requirements differ in axenic media and *in vivo*, and that during infection RBs utilize both G6P and cellular ATP. The latter could be provided and made more readily accessible by the localization of host glycolytic enzymes at the inclusion. As bacteria transition into EBs their metabolic demand may be met by importing and using host G6P for substrate level phosphorylation by producing glycolytic enzymes, although at a lower level than RBs, or by using enzymes previously transcribed and translated by the RB form of the bacteria.

If *Chlamydia* can utilize its own glycolytic pathway, why would host glycolytic enzymes localize to the inclusion? One possibility mentioned above is that an increased local concentration of ATP around the inclusion could facilitate ATP import across the inclusion membrane for utilization in the lumen of the inclusion and in the cytosol of the bacteria. It is also possible that the ATP generated by host glycolysis is used at the surface of the inclusion to fuel the myriad of reactions that mediate host-inclusion interactions (12). The glycolytic pathway also generates glycolytic intermediates which are shuttled into the pentose phosphate pathway and converted to ribonucleotides. If these reactions were to occur in the close proximity of the inclusion, it would also increase the local pool of host synthesized nucleotides that *Chlamydia* relies on for replication. Alternatively, *Chlamydia* may directly use intermediate glycolytic substrates. While it is not clear whether these specific host metabolic intermediates can be taken up by the bacteria, there are examples that demonstrate *Chlamydia's* ability to acquire metabolites from the host cell. As discussed above, the glycolytic intermediate G6P must be obtained

from the host and is imported via the bacterial UhpC antiporter (43). Additionally, work by Mehlitz et al. demonstrated that the TCA derived dicarboxylate malate is also taken up and metabolized by *C. trachomatis (42)*. Moreover, while the inclusion membrane was originally thought to be impermeable to low-molecular weight compounds, such as microinjected fluorophores greater than 520 Da (201), further studies showed that the inclusion membrane is permeable to ions (202). Thus, host metabolites such as glycolytic substrates, which are smaller than 520 Da, may also be able to passively enter the inclusion. Further experiments would be required to validate that it is indeed the case and if and how these metabolites can be used to support bacterial growth.

Altogether, our study further highlights the complex and elaborate metabolic relationship between *Chlamydia* and its host and reveal that the spatial and temporal distribution of host glycolytic enzymes around the inclusion may facilitate the intracellular development of this obligate intracellular pathogen and therefore identify potential routes for future therapeutic drug development.

Materials and Methods

Ethics Statement.

All genetic manipulations and containment work were approved by the University of Virginia Biosafety Committee and are in compliance with the section III-D-1-a of the NIH guidelines for research involving recombinant DNA molecules.

Cell Lines and Bacterial Strains.

HeLa cells were obtained from the ATCC (CCL-2) and cultured at 37°C with 5% CO_2 in high-glucose Dulbecco's modified Eagle's medium (DMEM; Invitrogen) supplemented

with 10% heat-inactivated fetal bovine serum (FBS; Invitrogen). *C. trachomatis* lymphogranuloma venereum (LGV) type II was obtained from the ATCC (L2/434/Bu VR-902B). *C. trachomatis* propagation and infection were performed as previously described (181). *C. muridarum* was obtained from Michael Starnbach (Harvard Medical School, Boston, MA). mCherry expressing *C. trachomatis* (mCherry CtL2) and *C. muridarum* strains were described previously (182).

Plasmid construction.

Restriction enzymes and T4 DNA ligase were obtained from New England BioLabs (Ipswich, MA). PCR was performed using Herculase DNA polymerase (Stratagene). PCR primers were obtained from Integrated DNA Technologies.

Vectors for Expression in Mammalian Cells.

DNA fragments corresponding to Pyruvate Kinase, Aldolase A, and the R42A and R148A mutants of Aldolase A were amplified by PCR and cloned into the *BamH*I and *Xho*I restriction sites of pCDNA 4/TO 3xFLAG. Lactate dehydrogenase was cloned into the *EcoR*I and *Xho*I restriction sites of pCDNA 4/TO 3xFLAG. HA-Aldolase A was cloned into the *Kpn*I and *Not*I restriction sites of pCDNA3.1+. Pyruvate Kinase, Aldolase A and Lactate dehydrogenase DNA fragments were amplified using uninfected HeLa cell cDNA as template and the primers are listed in Table 3.1.

DNA Transfection.

DNA transfection was performed using X-tremeGENE 9 DNA Transfection Reagent (Roche), according to the manufacturer's recommendations.

Immunofluorescence and Confocal Microscopy.

All steps were performed at room temperature. At the indicated times, HeLa cells seeded on glass coverslips were fixed with 4% paraformaldehyde in 1× PBS for 30 min. Coverslips were sequentially incubated with primary and secondary antibodies diluted in 0.1% Triton X-100 in 1× PBS for 1 h. Coverslips were washed with 1× PBS and mounted with DABCO antifade-containing mounting media. Imaging was performed using the Leica DMi8 microscope equipped with the Andor iXon ULTRA 888BV EMCCD camera and the confocal scanner unit CSU-W1, and driven by the IQ software. Images were processed using the Imaris software (Bitplane, Belfast, United Kingdom). Line intensity scan analyses presented in Figure 3.2E were performed using ImageJ (NIH).

Antibodies.

The following primary antibodies were used for immunofluorescence microscopy (IF) and immunoblotting (Western blot): mouse monoclonal anti-FLAG (1:1,000 for IF; Sigma), rabbit polyclonal anti-*C. trachomatis* IncA (1:200 for IF; kindly provided by T. Hackstadt, Rocky Mountain Laboratories), rabbit polyclonal anti-HA (1:100 for IF; Sigma), mouse monoclonal anti-Aldolase A (1:1,000 for Western blot; Santa Cruz), rabbit polyclonal anti-actin (1:10,000 for Western blot; Sigma), mouse monoclonal anti-α-tubulin (1:2000 for IF; Sigma), Alexa Fluor 514-conjugated Phalloidin (1:200 for IF; Invitrogen). The following secondary antibodies were used: Alexa Fluor 488-, Alexa Fluor 514-, or Pacific Blue-conjugated goat anti-mouse antibody (1:500 for IF; Molecular Probes), Pacific Blue-, or Alexa Fluor 514-conjugated goat anti-rabbit antibody (1:500 for IF; Molecular Probes), peroxidase-conjugated goat anti-mouse IgG (1:10,000 for Western blot; Jackson ImmunoResearch), peroxidase-conjugated goat anti-rabbit IgG (1:10,000 for Western blot; Jackson ImmunoResearch).

Quantification of host glycolytic enzyme enrichment at the inclusion.

HeLa cells were transfected with the indicated 3xFLAG-tagged enzyme construct 18 h before infection with the mCherry CtL2 strain. The samples were processed for confocal microscopy and analyzed using the Imaris imaging software. For each inclusion, the quantification was performed on a 1μm slice located in the middle of the inclusion. Three-dimensional reconstructions of the raw signal corresponding to the enzyme signal at the inclusion and to the enzyme signal in the surrounding cytosol were generated using the Imaris imaging software. The average intensity of these three-dimensional objects was calculated using Imaris imaging software. The average intensity of the enzyme signal at the inclusion divided by the average intensity of the surrounding cytosol was used to determine the percent enrichment of the enzyme at the inclusion. Each experiment was performed in triplicate. Fifteen to 30 inclusions were analyzed per condition. The graphs were generated using GraphPad Prism. Average and standard deviation (SD) are shown. A Student's t test was performed and statistical significance was set to $P < 0.05$.

Quantification of the percentage of inclusion positive for a given enzyme.

HeLa cells were transfected with the indicated 3xFLAG-tagged enzyme construct 18 h before infection with the mCherry CtL2 strain. The samples were processed for immunofluorescence microscopy and analyzed using an epifluorescence microscope. Transfected cells were scored for the presence (positive) or absence (negative) of a ring of enzyme enrichment at the inclusion (as seen in Figure 3.2A). One hundred inclusions were analyzed per condition. The average percent of positive inclusions and SD from three replicate experiments is presented. A Student's t test was performed and statistical significance was set to $P < 0.05$.

Quantification of the graph presented in Figure 3.3B was performed as described above, except that HeLa cells were co-transfected with HA-Aldolase A and the indicated 3xFLAG-tagged enzyme construct 18h before infection with the mCherry CtL2 strain. Inclusions in co-transfected cells were scored for the presence or absence the HA and 3xFLAG-tagged constructs.

Quantification of the graph presented in Figure 3.7B was performed as described above, except that the cells were transfected with the R42A, R148A, or WT Aldolase A.

Quantification of the graph presented in Figure 3.7C was performed as described above, except that the cells were infected the *inaC::aadA* mutant or corresponding WT *C. trachomatis* strain.

Inhibition of eukaryotic protein synthesis.

HeLa cells were transfected with the 3xFLAG-tagged Aldolase A construct 18h before infection with the mCherry CtL2 strain. At the time of infection, cells were incubated in the presence or absence of 1μg/mL cycloheximide for 18, 24, or 32h. At the indicated time point, the samples were processed for confocal microscopy and the percentage of positive inclusions was determined. One hundred inclusions were analyzed per condition. The average percent of positive inclusions and SD from three replicate experiments is presented. A one-way ANOVA with multiple comparisons was performed and statistical significance was set to $P < 0.05$.

Inhibition of *C. trachomatis* protein synthesis.

HeLa cells were transfected with the 3xFLAG-tagged Aldolase A construct 18 h before infection with the mCherry CtL2 strain. At 24h pi, infected cells were incubated in the presence of 40μg/ml of chloramphenicol for 8h. At 32h pi, the samples were processed

for confocal microscopy and the percentage of positive inclusions was determined. One hundred inclusions were analyzed per condition. The average percent of positive inclusions and SD from three replicate experiments is presented. A Student's *t* test was performed and statistical significance was set to $P < 0.05$.

Drug treatments.

HeLa cells were transfected with the indicated 3xFLAG-tagged enzyme construct 18h before infection with the mCherry CtL2 strain. For Cytochalasin D and Nocodazole treatment, at 23.5h pi, infected cells were incubated in the presence of 1μM Cytochalasin D or 33μM Nocodazole for 30 min. For Brefeldin A treatment, at 6h pi, infected cells were incubated in the presence of 1μg/mL Brefeldin A overnight. At 24h pi the samples for all drug treatments were processed for confocal microscopy and the percentage of positive inclusions was determined. One hundred inclusions were analyzed per condition. The average percent of positive inclusions and SD from three replicate experiments is presented. A Student's *t* test was performed and statistical significance was set to $P < 0.05$.

***inaC* mutant generation**

An *inaC::aadA* mutant was generated in our lab *C. trachomatis* LGV L2 strain background using TargeTron, as described by previous studies (46, 105). Using PCR, the GrpII intron was retargeted for *C. trachomatis* 434/Bu *inaC* using primers CTL0184 129 130 IBS1/2, CTL0184 129 130 EBS1/delta, and CTL0184 129 130 EBS2 designed by the TargeTron computer algorithm (TargeTronics) (Primer sequences are listed in Table 3.1). The resulting PCR product was digested with BsrGI and HindIII and cloned into the BsrGI/HindIII site of the pDFTT3-*aadA* suicide vector (203). *C. trachomatis* serovar L2

was transformed with pDFTT3-*aadA-inaC* following our calcium-based transformation protocol as previously described (182). Following three passages, transformants were plaque purified and amplified. Genomic DNA was prepared using an illustra bacteria genomicPrep Mini Spin Kit (GE Healthcare), according the manufacturer recommendations. The *inaC* open reading frame was amplified from WT or *inaC::aadA* mutant genomic DNA by PCR using primers CTL0184 Up and CTL0184 Dwn (Table 3.1). The resulting PCR products were analyzed by DNA gel electrophoresis and sequenced to verify proper insertion of the group II intron (Figure 3.12).
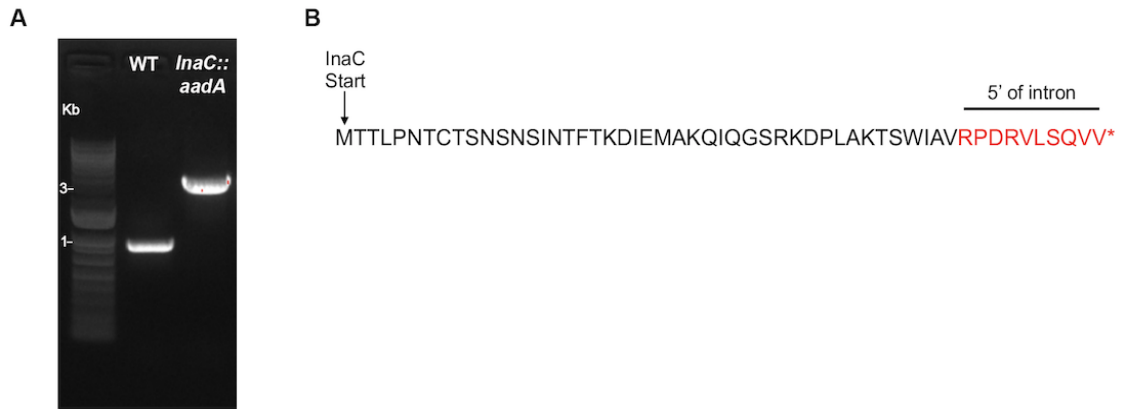
Figure 3.12 Validation of group II intron insertion in the *C. trachomatis inaC::aadA* mutant.
(A) PCR analysis of the *inaC::aadA* mutant. The *inaC* ORF was amplified from genomic DNA
extracted from WT *C. trachomatis* (WT) or the *inaC::aadA* mutant and the corresponding PCR
products were resolved on a 1% DNA agarose gel stained with ethidium bromide. Lane 1:
molecular weight marker; lane 2: WT; lane 3: *inaC::aadA* mutant. The marker sizes are listed in
kilo base pairs to the left. (B) The site of insertion of the group II intron was determined by
Sanger sequencing. A translation of the resulting InaC truncated peptide is presented. The asterisk
denotes the early stop codon introduced by insertion of the group II intron (black: InaC, red:
group II intron).

Aldolase A depletion.

The protocol for siRNA transfection has been described previously (181). Aldolase A

depletion was performed by transfection of four independent siRNA duplexes. The

sequences of the Aldolase A siRNA duplexes were: Duplex 1

(GGACAAAUGGCGAGACUAC), Duplex 2 (UUGAAGCGCUGCCAGUAUG),

Duplex 3 (GGCGUUGUGUGCUGAAGAU), Duplex 4

(UGACAUCGCUCACCGCAUC).

Immunoblotting.

Protein samples were separated by SDS-PAGE and transferred to nitrocellulose

membranes. The membranes were blocked for 1h at room temperature in 1xPBS

containing 0.05% Tween and 5% fat-free milk. Primary and HRP-conjugated secondary

antibodies were diluted in 1xPBS containing 0.05% Tween and 5% fat-free milk and

incubated overnight at 4°C and 1h at room temperature, respectively. Proteins were

detected using the Amersham ECL immunoblotting detection reagent, as per

manufacturer recommendation, and a Bio-Rad ChemiDoc imaging system. Immunoblots

were quantified using ImageJ (NIH) software.

Inclusion size quantification and computer-assisted image analysis.

HeLa cells were transfected with the indicated 3xFLAG-tagged enzyme construct 18-24h

before infection with the mCherry CtL2 strain. The samples were processed for

immunofluorescence microscopy and imaged using an epifluorescence microscope.

Computer-assisted image analysis, using the analytical tools of the MetaExpress

software, was used to determine the area of each Aldolase A positive and negative

inclusion. One hundred inclusions were analyzed per condition.

For quantification of the graph presented in Figure 3.10C, siRNA treated cells were infected with the mCherry CtL2 strain and fixed 32h pi. The nuclei were labeled with the DNA dye Hoechst. The cells were subjected to automated fluorescence microscopy using an ImageXpress automated system to capture images corresponding to the cell nuclei and the inclusion. Computer-assisted image analysis, using the analytical tools of the MetaExpress software, was used to determine the number of nuclei and the total area of each inclusion.

Infectious progeny production.

HeLa cells incubated with the indicated siRNA duplexes for 3 days were collected 48h pi, lysed with water and dilutions of the lysate were used to infect fresh HeLa cells. The cells were fixed 24h pi and the number of inclusion forming units (IFUs) was determined after assessment of the number of infected cells by automated imaging using an ImageXpress automated system.

Real-time PCR analysis of bacterial glycolytic gene expression.

At the indicated time point, infected cells were homogenized with TRIzol (Thermo Fisher Scientific) to extract RNA from infected cells. Each RNA sample was treated with DNase following the TURBO DNA-free kit protocol (Thermo Fisher Scientific). Complementary DNA (cDNA) was synthesized using SuperScript II reverse transcriptase (Thermo Fisher Scientific), following the manufacturer's protocol. Samples were primed using random primers (Thermo Fisher Scientific). mRNA levels were determined by quantitative real-time PCR using the Universal Probe Library (Roche Biochemicals, Indianapolis, IN) and Luna Universal qPCR master mix (New England Biolabs). Thermal cycling was carried out using a Light Cycler 96 instrument (Roche Diagnostics) under the

following conditions: 95°C for 5 min and 45 cycles of 95°C for 10 s and 56°C for 25 s. Cq values were derived using the LightCycler 96 software and fold changes were calculated using Ct 16S rRNA for normalization (204, 205). Statistical analysis was performed by Student's *t* test and statistical significance was set to *P* < 0.05. PCR primers used for quantitative real-time PCR were obtained from Integrated DNA Technologies. Primer sequences and corresponding probes are listed in Table 3.2 in the supplemental material.

Acknowledgments

Chapter 4:

Phospho-regulation accommodates Type III secretion and assembly of a tether of ER-*Chlamydia* inclusion membrane contact sites

Data presented in Figures 4.1, 4.2, 4.3, 4.4A-B, 4.11A, and 4.12 generated by R.Murray

Data presented in Figures 4.19B-C, 4.20, and 4.21 generated by S. D'Spain

Data presented in Figures 4.10G-H, and 4.13 generated by I. Coppens

All other data presented in this chapter generated by R. Ende

Abstract

Membrane contact sites (MCS) are crucial for non-vesicular trafficking-based inter-organelle communication. ER-organelle tethering occurs in part through the interaction of the ER resident protein VAP with FFAT-motif containing proteins. FFAT motifs are characterized by a seven amino acidic core surrounded by acid tracks. We have previously shown that the human intracellular bacterial pathogen *Chlamydia trachomatis* establishes MCS between its vacuole (the inclusion) and the ER through expression of a bacterial tether, IncV, displaying molecular mimicry of eukaryotic FFAT motif cores. Here, we show that multiple layers of host cell kinase-mediated phosphorylation events govern the assembly of the IncV-VAP tethering complex and the formation of ER-Inclusion MCS. Via a C-terminal region containing three CK2 phosphorylation motifs, IncV recruits CK2 to the inclusion leading to IncV hyperphosphorylation of the non-canonical FFAT motif core and serine-rich tracts immediately upstream of IncV FFAT motif cores. Phosphorylatable serine tracts, rather than genetically-encoded acidic tracts, accommodate T3SS-mediated translocation of IncV to the inclusion membrane, while achieving full mimicry of FFAT motifs. Thus, regulatory components and post-translational modifications are integral to MCS biology, and intracellular pathogens such as *C. trachomatis* have evolved complex molecular mimicry of these eukaryotic features.

Introduction

In naïve cells, membrane contact sites (MCS) are points of contact between the membrane of two adjacent organelles (10-30 nm apart). They provide physical platforms for the non-vesicular transfer of lipids and ions, and cell signaling events important for inter-organelle communication and organelle positioning and dynamics (206). Since their discovery and implication in cell homeostasis, MCS dysfunction has been linked to several human diseases (207-209). At the molecular level, depending on the contacting organelles [endoplasmic reticulum (ER)-Golgi, ER-mitochondria, ER-plasma membrane (PM), etc…], each MCS is enriched in specific proteinaceous factors that contribute to the specialized biological function of a given MCS (206). By bridging the membrane of apposed organelles, either via protein-protein or protein-lipid interactions, MCS components also form tethering complexes that increase the affinity of one organelle to another and thereby keep their membranes in close proximity (131, 206, 210). Although the overall molecular composition of each MCS is different, one integral ER protein, the vesicle-associated membrane protein (VAMP)-associated protein (VAP) (211), engages in tethering complexes at several MCS. This is accomplished by interaction of the cytosolic major sperm protein (MSP) domain of VAP with proteins containing two phenylalanine (FF) in an acidic tract (FFAT) motifs (154, 211). FFAT motif containing proteins include soluble proteins, such as lipid transfer proteins that contain an additional domain for targeting to the opposing membrane, and transmembrane proteins anchored to the contacting organelle (178). The molecular determinants driving the VAP-FFAT interaction have been investigated at the cellular and structural level. A consensus of the FFAT motif core was first defined as seven amino acids, $E^1F^2F^3D^4A^5x^6E^7$; however, the

core motif of many identified VAP interacting proteins deviates from this canonical sequence (154, 178). In addition to the core, acidic residues surrounding the core motif are proposed to facilitate the VAP-FFAT interaction through electrostatic interactions (212).

In addition to their critical role in inter-organelle communication, MCS are exploited by intracellular pathogens for replication (213-216). One example is the obligate intracellular bacterium *Chlamydia trachomatis,* the causative agent of the most commonly reported bacterial sexually transmitted infection. Upon invasion of the genital epithelium, *C. trachomatis* replicates within a membrane-bound vacuole called the inclusion (26). Maturation of the inclusion relies on *Chlamydia* effector proteins that are translocated across the inclusion membrane *via* a bacterially encoded T3SS (217). A subset of *Chlamydia* T3SS effector proteins, known as the inclusion membrane proteins (Inc), are inserted into the inclusion membrane and are therefore strategically positioned to mediate inclusion interactions with host cell organelles (29, 62, 64, 65). These interactions include points of contact between the ER and the inclusion membrane, without membrane fusion (74, 127), which are referred to as ER-Inclusion MCS based on their similarities to MCS between cellular organelles (74, 160).

Characterization of the protein composition of ER-Inclusion MCS led to the identification the Inc protein IncV, which constitutes a structural component that tethers the ER membrane to the inclusion membrane through interaction with VAP (68). The IncV-VAP interaction relies on the presence of two FFAT motifs in the C-terminal cytosolic tail of IncV. The core sequence of one of the motifs ($_{286}E^1Y^2M^3D^4A^5L^6E^7_{292}$) is similar to the canonical sequence, whereas a second motif ($_{262}S^1F^2H^3T^4P^5P^6N^7_{268}$)

deviates significantly and was originally defined as a non-canonical FFAT. Similar to eukaryotic FFAT, the residue in position 2 in each motif (Y_{287} and F_{263}, respectively) are essential for the IncV-VAP interaction during infection. However, it remains unclear whether additional determinants promote the assembly of this bacterial tether.

Here, we show that multiple layers of host cell kinase-mediated phosphorylation govern the assembly of the IncV-VAP tethering complex and ER-Inclusion MCS formation. IncV phosphorylation supports the IncV-VAP interaction through FFAT motifs displaying core domains immediately downstream of phosphorylation-mediated acidic tracts. Since the substitution for genetically encoded acidic tracts interfered with IncV translocation, we propose that *Chlamydia* evolved a post-translocation phosphorylation strategy in order to accommodate proper secretion via the T3SS, while achieving full mimicry of eukaryotic FFAT motifs.

Results

IncV is modified by phosphorylation

When subjected to anti-FLAG western blot analysis, we noticed that lysates of HEK293 eukaryotic cells infected with wild type *C. trachomatis* expressing IncV-3xFLAG displayed a doublet consisting of a 50kDa and 60 kDa band (Figure 4.1A, middle lane, 293 + *Ct*). By contrast, IncV-3xFLAG ectopically expressed in HEK293 cells had an apparent molecular weight that was shifted toward the 60k Da band of the doublet (Figure 4.1A, left lane, 293), while IncV-3xFLAG expressed in *E. coli* had an apparent molecular weight equivalent to the 50 kDa band of the doublet (Figure 4.1A, right lane,

Ec). This result led us to hypothesize that IncV is post-translationally modified by a host factor.

To determine if phosphorylation could account for the increase in the apparent molecular weight of IncV, we performed a phosphatase assay. IncV-3xFLAG was immunoprecipitated, using anti-FLAG-conjugated Sepharose beads, from lysates of HEK293 cells infected with *C. trachomatis* expressing IncV-3xFLAG. Following the release of IncV-3xFLAG from the beads by FLAG peptide competition, the eluate was treated with lambda (λ) phosphatase or phosphatase buffer alone, and subsequently subjected to anti-FLAG western blot analysis (Figure 4.1B). In the absence of λ phosphatase, the apparent molecular weight of IncV-3xFLAG was approximately 60 kDa (Figure 4.1B, left lane). Upon phosphatase treatment, we observed a decrease in the apparent molecular weight of IncV-3xFLAG to approximately 50 kDa, similar to what was observed when IncV-3xFLAG was expressed in *E. coli* (Figure 4.1B, right lane). Altogether, these results demonstrate that IncV is phosphorylated by a host cell kinase.

The host kinase CK2 phosphorylates IncV

We next focused on identifying the host cell kinase(s) responsible for phosphorylating IncV. All three subunits of Protein Kinase CK2 were identified as potential interacting partners of IncV in an Inc-human interactome (198). To determine if CK2 associated with IncV at ER-Inclusion MCS, HeLa cells transfected with YFP-CK2α or YFP-CK2β constructs and infected with *C. trachomatis* wild type expressing mCherry under a constitutive promoter and IncV-3xFLAG under the aTc-inducible promoter were analyzed by confocal immunofluorescence microscopy (Figure 4.2). In the absence of

IncV-3xFLAG expression, YFP-CK2α and YFP-CK2β were undetectable at the inclusion (Figure 4.2A and B, -aTc). However, upon expression of IncV-3xFLAG, YFP-CK2α and YFP-CK2β were recruited to the inclusion membrane and colocalized with IncV (Figure 4.2A and B, +aTc). To confirm that this phenotype was not the result of overexpression of the CK2 subunits, we used antibodies that recognized the endogenous CK2β subunit and showed that endogenous CK2β colocalized with IncV at the inclusion, when IncV-3xFLAG expression was induced (Figure 4.1C). Altogether, these results demonstrate that CK2 is a novel component of ER-Inclusion MCS that is recruited to the inclusion in an IncV-dependent manner.

Having established that IncV is phosphorylated and that CK2 localizes to ER-Inclusion MCS in an IncV-dependent manner, we next tested if CK2 phosphorylates IncV. We performed an *in vitro* kinase assay using recombinant CK2 and the cytosolic domain of IncV (amino acids 167-363 of IncV) fused to GST (GST-IncV$_{167-363}$) or GST alone, purified from *E. coli*. To detect phosphorylation, we used ATPγS, which can be utilized by kinases to thiophosphorylate a substrate, followed by an alkylation reaction of the thiol group to generate an epitope that is detected using an antibody that recognizes thiophosphate esters (218). When GST alone was provided as a substrate, there was no detectable phosphorylation, regardless of the presence of CK2 and ATPγS (Figure 4.1D, lanes 1 and 2). A similar result was observed with GST-IncV$_{167-363}$ in the absence of CK2 and/or ATPγS (Figure 4.1D, lanes 3 - 5). However, in the presence of both ATPγS and CK2, GST-IncV$_{167-363}$ was phosphorylated (Figure 4.1D, lane 6). Altogether, these results demonstrate that CK2 directly phosphorylates IncV *in vitro*.
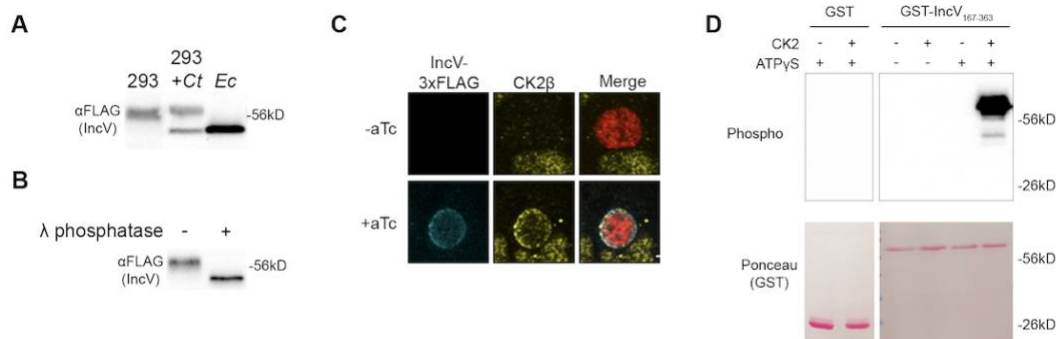
Figure 4.1 CK2 localize to the inclusion and phosphorylates IncV. (A) Western blot of IncV-3xFLAG from lysates of HEK293 cells expressing IncV-3xFLAG (293), HEK293 cells infected with *C. trachomatis* expressing IncV-3xFLAG (293 + *Ct*), or *E. coli* expressing IncV-3xFLAG (*Ec*). (B) Western blot of IncV-3xFLAG purified from lysates of HEK293 cells infected with *C. trachomatis* expressing IncV-3xFLAG and treated with lambda (λ) phosphatase (+) or phosphatase buffer alone (-). (C) 3-dimensional reconstruction of confocal images of HeLa cells infected with *C. trachomatis* expressing mCherry constitutively (red) and IncV-3xFLAG (blue) under the control of an anhydrotetracycline (aTc)-inducible promoter in the absence (-aTc) or presence (+aTc) of aTc and stained to detect endogenous CK2β (Yellow). The merge is shown on the right. Scale bar is 5μm. (D) *In vitro* kinase assay using GST or GST-IncV$_{167-363}$ purified from *E. coli* as a substrate in the presence (+) or absence (-) of recombinant CK2 and in the presence (+) or absence (-) of ATPγS. The top panel shows phosphorylated proteins detected with anti-Thiophosphate antibodies and the bottom panel is the same membrane stained with Ponceau S to detect total proteins. Data generated by Rebecca Murray.
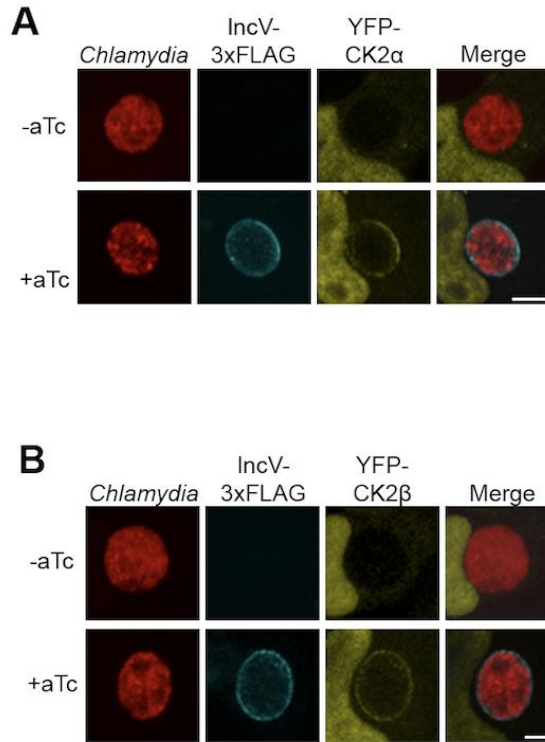
Figure 4.2 IncV recruits CK2 to the inclusion membrane. (A-B) 3-dimensional reconstruction of confocal images of HeLa cells overexpressing YFP-CK2α (A) or YFP-CK2β (B) (yellow) and infected with *C. trachomatis* expressing mCherry constitutively (red) and IncV-3xFLAG (blue) under the control of an anhydrotetracycline (aTc)-inducible promoter in the absence (-aTc) or presence (+aTc) of aTc. The merge is shown on the right. Scale bar is 5μm. Data generated by Rebecca Murray.

Phosphorylation of IncV is necessary and sufficient to promote the IncV-VAP interaction *in vitro*

We have previously reported an IncV-VAP interaction *in vitro* upon incubation of IncV$_{167-363}$ with the cytosolic MSP domain of VAP (GST-VAP$_{MSP}$) purified from *E. coli* (68). However, this interaction was only detected when IncV$_{167-363}$ was produced in eukaryotic cells, which, based on the above results, led us to hypothesize that IncV phosphorylation is required for the IncV-VAP interaction. We assessed the role of phosphorylation in the IncV-VAP interaction by performing lambda (λ) phosphatase dephosphorylation of IncV coupled with a GST-VAP$_{MSP}$ pull-down assay (Figure 4.3A). IncV-3xFLAG was immunoprecipitated from lysates of HEK293 cells using anti-FLAG-conjugated Sepharose beads, released from the beads using FLAG peptide competition, and treated with λ phosphatase or buffer alone. Treated and untreated IncV-3xFLAG samples were then incubated with GST-VAP$_{MSP}$ or GST alone bound to glutathione Sepharose beads. The protein-bound beads were subjected to western blot analysis using an anti-FLAG antibody (Figure 4.3B). Untreated IncV-3xFLAG was pulled down by GST-VAP$_{MSP}$ but not by GST alone, demonstrating a specific interaction between IncV and VAP (Figure 4.3B, lanes 1 - 3). However, when the eluate containing IncV-3xFLAG was treated with λ phosphatase prior to incubation with GST-VAP$_{MSP}$, the two proteins failed to interact (Figure 4.3B, lane 4), indicating that phosphorylation of IncV is necessary for the IncV-VAP interaction *in vitro.*

We next determined if IncV phosphorylation by CK2 was sufficient to promote the IncV-VAP interaction in an *in vitro* binding assay (Figure 4.3C). MBP-tagged VAP$_{MSP}$ (MBP-VAP$_{MSP}$) and GST-IncV$_{167-363}$ were expressed separately in *E. coli* and

purified using amylose resin and glutathione Sepharose beads, respectively. GST-IncV$_{167-363}$ was left attached to glutathione Sepharose beads and was phosphorylated by incubation with recombinant CK2 and ATP before being combined with purified MBP-VAP$_{MSP}$. GST-IncV$_{167-363}$ was pulled down and the samples were subjected to western blot using anti-MBP antibodies (Figure 4.3D). Neither the beads alone, nor GST alone pulled down MBP-VAP$_{MSP}$, regardless of whether CK2 and ATP were present or not (Figure 4.3D, lanes 1 - 4). In the absence of CK2 and ATP, we observed minimal binding of MBP-VAP$_{MSP}$ to GST-IncV$_{167-363}$ (Figure 4.3D, lane 5). However, when GST-IncV$_{167-363}$ was treated with CK2 and ATP prior to GST-pull-down, MBP-VAP$_{MSP}$ and GST-IncV$_{167-363}$ co-immuno-precipitated, indicating that phosphorylation of IncV by CK2 is sufficient to promote the IncV-VAP interaction *in vitro* (Figure 4.3D, lane 6). Altogether, these results demonstrate that IncV phosphorylation is necessary and sufficient for the IncV-VAP interaction *in vitro*.
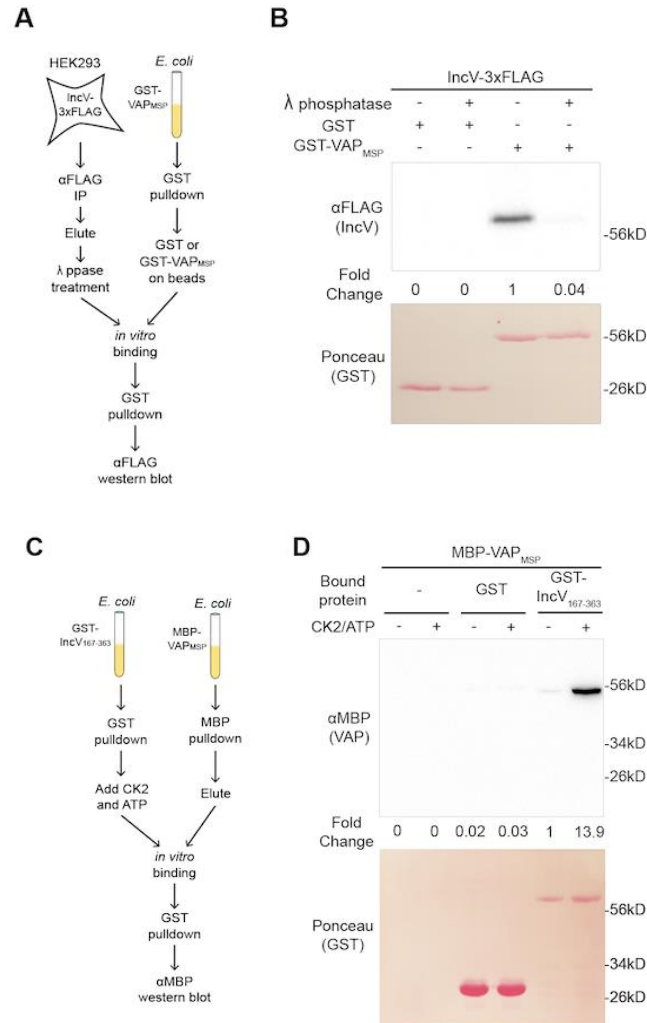
Figure 4.3 Phosphorylation of IncV is necessary and sufficient to promote the IncV-VAP interaction *in vitro*. (A) Schematic depicting the experimental setup for results in B. (B) *In vitro* binding assay using IncV-3xFLAG purified from HEK293 lysates and treated with lambda (λ) phosphatase (+) or phosphatase buffer alone (-) combined with GST or GST-VAP$_{MSP}$ purified from *E. coli* and immobilized on glutathione beads. The top panel shows proteins detected with anti-FLAG anti-bodies and the bottom panel is the same membrane stained with Ponceau S to detect total protein. (C) Schematic depicting the experimental setup for results in D. (D) *In vitro* binding assay using GST or GST-IncV$_{167-363}$ purified from *E. coli*, and immobilized on glutathione beads, as a substrate for CK2 in the presence (+) or absence (-) of CK2 and ATP, combined with MBP-VAP$_{MSP}$ purified from *E. coli*. The top panel was probed with anti-MBP and the bottom panel was the same membrane stained with Ponceau S to detect the GST construct. Data generated by Rebecca Murray.

107

CK2 kinase activity is required for IncV phosphorylation and IncV-VAP interaction at the inclusion

We next determined the contribution of CK2 to IncV phosphorylation and the subsequent assembly of the IncV-VAP tether at the inclusion. We first used a genetic approach to deplete CK2β. Because CK2 is essential (219, 220), we favored a gene silencing approach over a CRISPR-based knock out approach. HeLa cells treated with individual siRNA duplexes targeting *CSNK2B* (A, B, C, or D), or a pool of all four siRNA duplexes (pool), were infected with a previously characterized *incV* mutant strain of *C. trachomatis* (68, 99), expressing IncV$_{WT}$-3xFLAG from an aTc inducible promoter. The cells were lysed and subjected to western blot analysis. The efficacy of *CSNK2B* knockdown was confirmed by western blot, demonstrating that, in siRNA treated cells, CK2β protein levels ranged from 9.3% to 53.3% compared to control cells (Figure 4.4A, middle blot). As shown in Figure 4.1A, in control cells, IncV$_{WT}$-3xFLAG appeared as a doublet (Figure 4.4A, top blot, left lane, ooo and o). In contrast, depletion of CK2β led to the appearance of additional bands of intermediate apparent molecular weight (Figure 4.4A, top and middle blots, pool, A, B, C, D lanes, oo). A line scan analysis of the control sample revealed two peaks corresponding to the top band, corresponding to hyper-phosphorylated IncV (Figure 4.4B, black line, left peak, ooo) and to the bottom band, corresponding to unphosphorylated IncV (Figure 4.4B, black line, right peak, o). A similar analysis of the banding pattern of IncV upon CK2β depletion, with the pooled or individual siRNA duplexes, revealed the appearance of intermediate peaks between the top and bottom bands, suggesting the formation of hypo-phosphorylated species of IncV (Figure 4.4B, middle peaks, oo). These results provided a first indication that CK2

mediates IncV phosphorylation during infection. However, none of the siRNA duplex treatments led to a complete dephosphorylation of IncV, which could be due to the incomplete knockdown of CK2β (Figure 4.4A, middle blot).

To complement the genetic approach described above, we conducted a pharmacological approach using the CK2-specific inhibitor CX-4945 (221). HeLa cells infected with a *C. trachomatis incV* mutant expressing IncV$_{WT}$-3xFLAG under the control of the aTc inducible promoter were treated with increasing concentrations of CX-4945 (0, 0.625, 10 µM) at 18h pi, prior to the induction of IncV$_{WT}$-3xFLAG expression at 20h pi. This experimental set up allowed for CK2 inhibition, prior to IncV$_{WT}$-3xFLAG synthesis, translocation, insertion into the inclusion membrane and exposure to the host cell cytosol. The cells were lysed 24h pi and subjected to western blot analysis to determine the effect of CK2 inhibition on the apparent molecular weight of IncV. The apparent molecular weight of IncV decreased in a dose-dependent manner (Figure 4.4C, top blot), leading to an apparent molecular weight corresponding to unphosphorylated IncV at the 10 µM concentration. These results demonstrate that CK2 activity is essential for IncV phosphorylation during infection.

We next determined whether inhibition of CK2 kinase activity affected the IncV-dependent VAP recruitment to the inclusion and, therefore, the assembly of the IncV-VAP tether. We used the same experimental setup as above, except that the cells expressed CFP-VAP. At 24h pi, the cells were fixed, immuno-stained with anti-FLAG antibody, and processed for confocal microscopy. Qualitative and quantitative assessment of the micrographs indicated that CX-4945 did not interfere with IncV translocation and insertion into the inclusion membrane (Figure 4.4D and Figure 4.5). The quantification

method is illustrated in Figure 4.6. As previously observed (68), IncV$_{WT}$-3xFLAG

expression correlated with a strong CFP-VAP association with the inclusion (Figure

4.4D, top panels). In comparison, pre-treatment of the cells with 10µM of CX-4945

abolished VAP recruitment to the inclusion (Figure 4.4D, bottom panels). Quantification

of the CFP-VAP signal associated with IncV at the inclusion membrane confirmed the

qualitative analysis and also revealed an intermediate phenotype for cells treated with

0.625µM of CX-4945 (Figure 4.4D-E). To rule out any off-target effect of CX-4945, we

tested an independent CK2-specific inhibitor, GO289 (222). As observed with CX-4945,

GO289-mediated CK2 inhibition led to the dose dependent dephosphorylation of IncV

(Figure 4.7A) and a significant reduction in the percentage of inclusions associated with

VAP (Figure 4.7B-C). Altogether, these results demonstrate that phosphorylation of IncV

by CK2 is required for the IncV-dependent VAP recruitment to the inclusion.
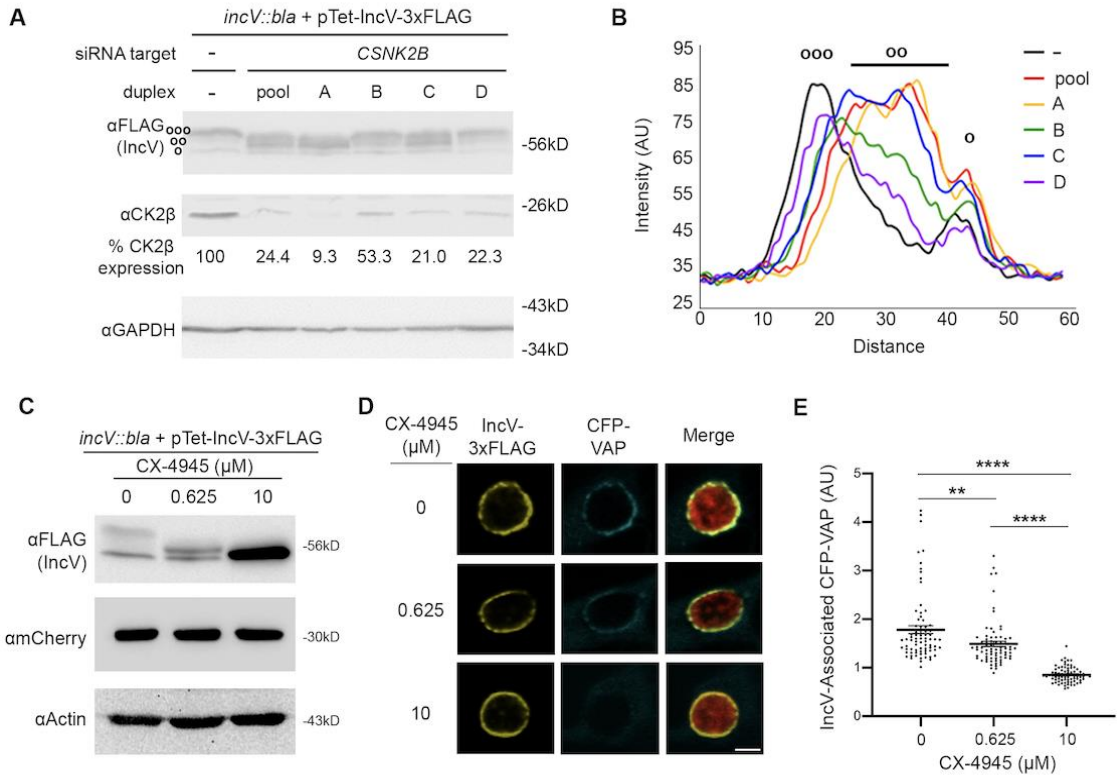
Figure 4.4 CK2 plays a role in the IncV-VAP interaction during infection. (A) Western blot of lysates of HeLa cells treated with siRNA buffer alone (-) or with siRNA duplexes targeting *CSNK2B* (pool of 4 duplexes or individual duplexes A, B, C, or D) and infected with a *C. trachomatis incV* mutant expressing IncV-3xFLAG. The top panel was probed with anti-FLAG. The middle panel was probed with anti-CK2β. The bottom panel was probed with anti-GAPDH. Relative expression levels of CK2β normalized to GAPDH loading controls are shown as a percentage of no siRNA control expression. (ooo) hyperphosphorylated IncV, (oo) intermediate hypophosphorylated IncV, (o) unphosphorylated IncV. (B) Line Scan analysis of FLAG signal detected in A. The peak on the left (ooo) corresponds to the hyperphosphorylated species of IncV, and the peak on the right (o) corresponds to the unphosphorylated species of IncV. Intermediate hypophosphorylated species are indicated by any peak between the left and right peaks (oo). Each line represents a different condition: Control, black; siRNA pool of duplexes A-D, red; siRNA duplex A, yellow; siRNA duplex B, green; siRNA duplex C, blue; siRNA duplex D, purple. (C-E) HeLa cells, expressing CFP-VAP (D-E only), were infected with *C. trachomatis incV* mutant expressing IncV-3xFLAG under the control of the aTc inducible promoter and treated with increasing concentrations of the CK2 inhibitor CX-4945 (0, 0.625, 10 µM) for two hours at 18h pi and prior to the induction of IncV-3xFLAG expression at 20h pi. The samples were processed 24h pi for western blot (C) or confocal microscopy (D-E). (C) Cell lysates were probed with anti-FLAG (top blot), anti-mCherry (middle blot), or anti-actin (bottom blot) antibodies. (D) Single plane confocal micrographs of HeLa cells expressing CFP-VAP (blue), infected with *incV* mutant expressing IncV-3xFLAG (yellow) and mCherry (red). The merge is shown on the right. Scale bar is 5µm. (E) Quantification of the mean intensity of the CFP-VAP signal within an object generated from the IncV-3xFLAG signal and normalized to the mean intensity of CFP-VAP in the ER. Each dot represents one inclusion. Data show the mean and SEM of a combination of

111

three independent experiments. One-way ANOVA and Tukey's post hoc test was performed. ** $P <0.01$, **** $P <0.0001$. Data presented in A and B generated by Rebecca Murray.
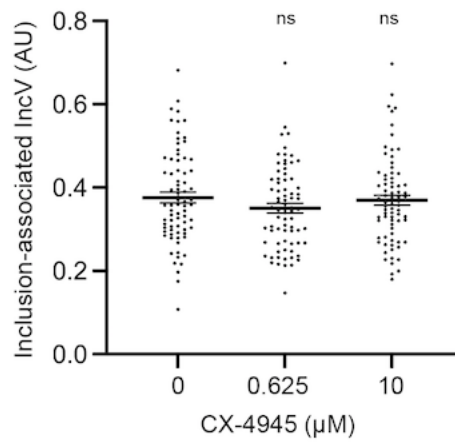
Figure 4.5 IncV inclusion localization is not affected upon CX-4945 treatment.
Quantification of the volume of the indicated IncV-3xFLAG signal associated with the inclusion normalized to the volume of an object generated from the mCherry signal of the bacteria. Each dot represents one inclusion. The mean and SEM are shown. One-way ANOVA and Tukey's post hoc test was performed comparing drug treated cells to control cells. ns non-significant.
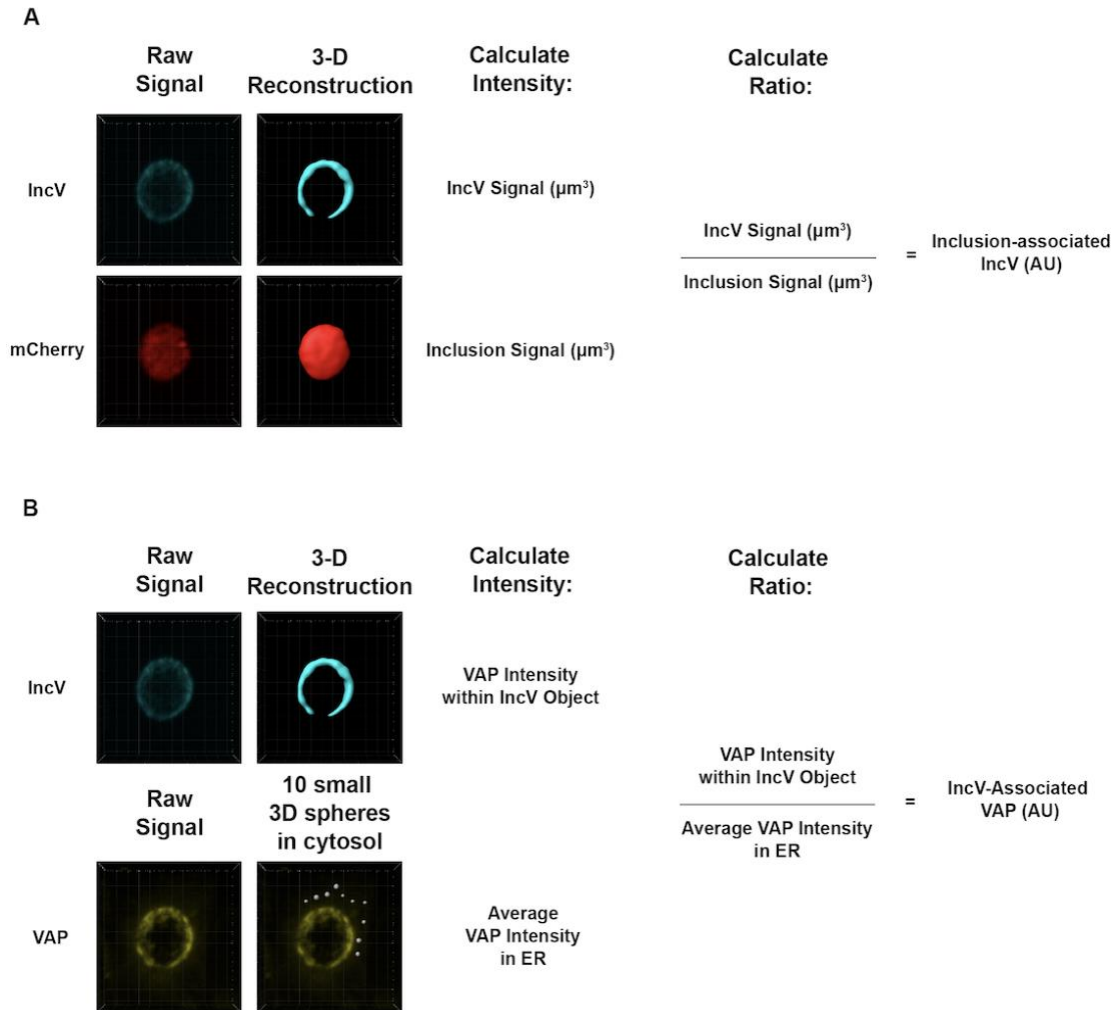
Figure 4.6 Method to quantify the inclusion association of a given marker. (A) Three-dimensional (3D) objects were reconstructed from the raw signal corresponding to the IncV (blue) and the mCherry positive inclusion (red) signals. The ratio of the IncV signal over the inclusion signal was calculated to determine IncV association with the inclusion in arbitrary units [AU]. (B) The signal intensity of a given marker (VAP in yellow is shown here) within the reconstituted 3D IncV object (blue), and within the cytosol (deterposmined by the average of 10 small 3D spheres throughout the ER), were determined. The IncV association of the given marker was determined by normalizing the signal intensity of the marker of interest within the IncV 3D object to the average signal intensity of the marker of interest within the ER (VAP) or cytosol (CK2).
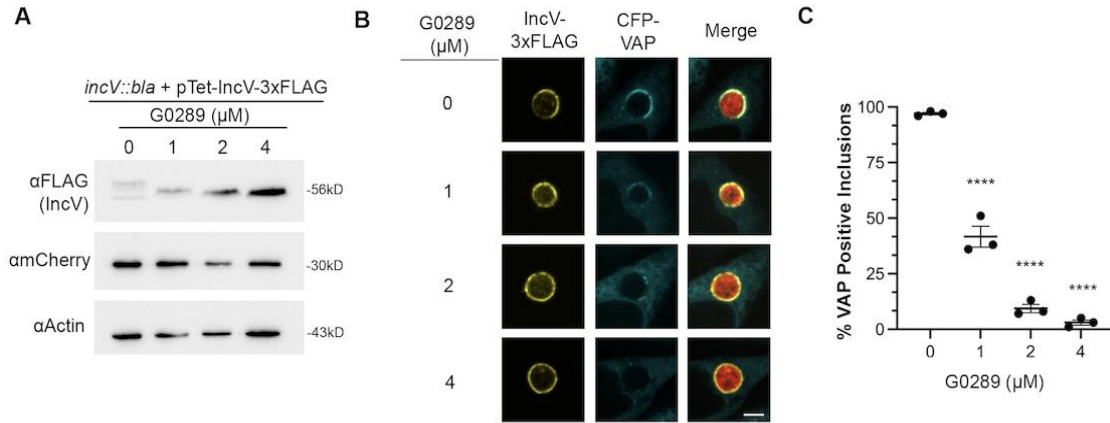
Figure 4.7 The CK2 kinase inhibitor GO289 inhibits IncV phosphorylation and VAP recruitment to the inclusion. (A) Cell lysates of HeLa cells infected for 24h with a *C. trachomatis incV* mutant expressing IncV-3xFLAG under the control of the aTc inducible promoter and treated with increasing concentrations of the CK2 inhibitor G0289 (0, 1, 2, 4 μM) for two hours at 18h pi and prior to the aTc induction of IncV-3xFLAG expression at 20h pi, probed with anti-FLAG (top blot), anti-mCherry (middle blot), or anti-actin (bottom blot) antibodies. (B) Single plane confocal micrographs of HeLa cells expressing CFP-VAP (blue), infected with *incV* mutant expressing IncV-3xFLAG (yellow) and mCherry (red) and treated with GO289 as described in A. The merge is shown on the right. Scale bar is 5μm. (C) Quantification of the percentage on inclusions exhibiting VAP recruitment to the inclusion. Data show the mean and SEM of three independent experiments. One-way ANOVA and Tukey's post hoc test was performed. **** $P < 0.0001$.

CK2 kinase activity is dispensable for CK2 localization to the inclusion and

reversing CK2 inhibition restores VAP recruitment to the inclusion

To further investigate the sequence of events leading to the CK2- and IncV

phosphorylation-dependent VAP recruitment to the inclusion, we first determined if CK2

kinase activity was required for CK2 recruitment to the inclusion. HeLa cells expressing

YFP-CK2β were infected with the *C. trachomatis incV* mutant expressing IncV$_{WT}$-

3xFLAG. 10 µM CX-4945 was added, or not, at 18h pi, and IncV expression was

induced at 20h pi by addition of aTc, as described in Figure 4.4D-E. At 24h pi, the cells

were fixed, immuno-stained with anti-FLAG antibody, and processed for confocal

microscopy. Qualitative and quantitative assessment of the micrographs indicated that

CX-4945 did not interfere with CK2 association with the inclusion (Figure 4.8A-B).

Thus, CK2 kinase activity is dispensable for the IncV-dependent CK2 localization to the

inclusion.

Altogether, our results suggest that CK2 is recruited first and that VAP

recruitment only occurs once CK2 phosphorylates IncV. To test this model, we

determined if reversing CK2 inhibition, after CK2 had been recruited to the inclusion,

would restore VAP association with the inclusion (Figure 4.8C). HeLa cells expressing

YFP-CK2β and CFP-VAP, and infected with the *C. trachomatis incV* mutant expressing

IncV$_{WT}$-3xFLAG, were treated with CX-4945 at 18h pi. *incV* expression was induced at

20h pi by addition of aTc, in the presence of CX-4945. At 24h pi, the cells were washed

and incubated with media containing either aTc and CX-4945 (CX-4945 replaced) or aTc

only (CX-4945 washout) for an additional hour (25h pi). Samples where CX-4945 was

omitted and collected at 25h pi (No CX-4945), and samples processed in the presence of

CX-4945 and collected at 24h pi prior to the wash (CX-4945) were used as controls.

None of the treatment prevented IncV localization to the inclusion (Figure 4.9).

Qualitative and quantitative assessment of the micrographs confirmed that, as observed

before, CX-4945 had no effect on CK2 association with the inclusion but strongly

prevented VAP recruitment (Figure 4.8D-E, compare CX-4945 to No CX-4945). A

similar result was observed when the media was replenished with CX-4945 after the

wash (Figure 4.8D-E, compare CX-4945 replaced to CX-4945). In comparison, CX-4945

washout post CK2 association with the inclusion, led to a robust VAP recruitment to the

inclusion, similar to the one observed in the absence of CX-4945 (Figure 4.8D-E,

compare CX-4945 washout to No CX-4945). Altogether, these results indicate that the

IncV-dependent CK2 association with the inclusion does not require CK2 kinase activity

and precedes VAP recruitment, which requires an active CK2 kinase.
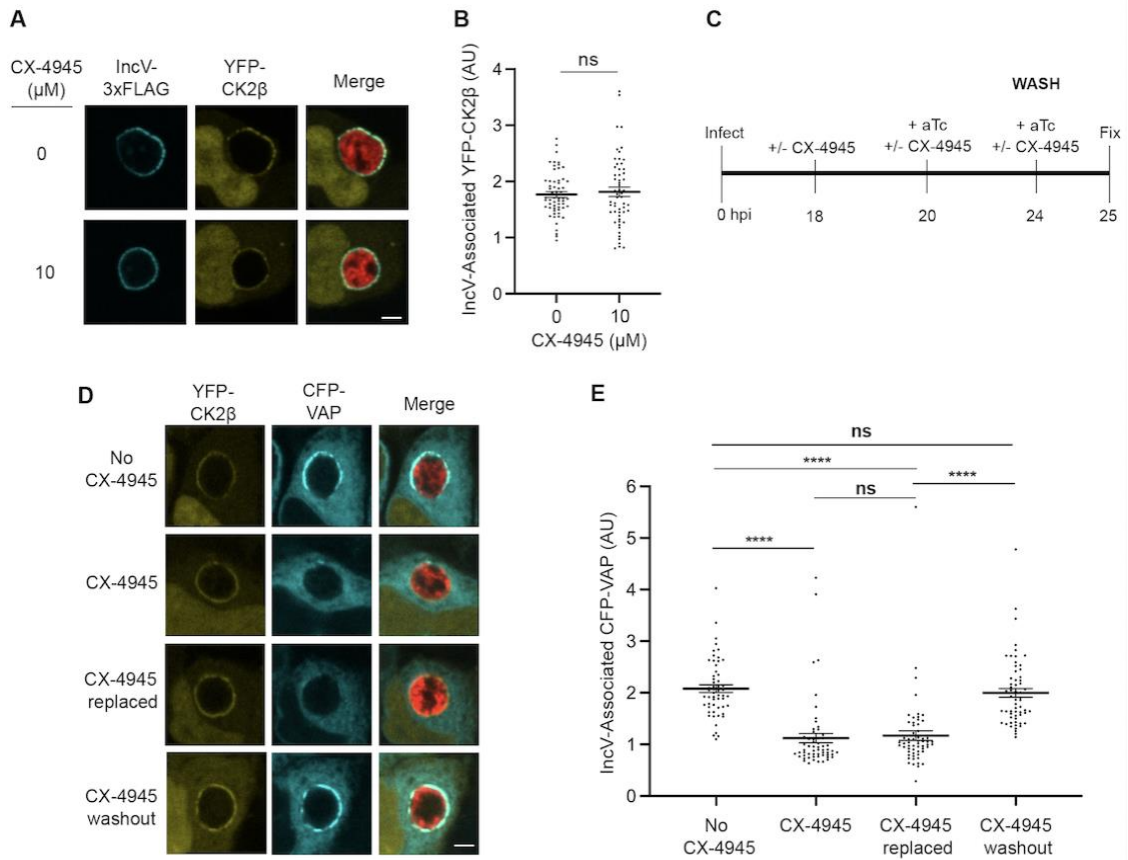
Figure 4.8 CK2 kinase activity is dispensable for CK2 localization to the inclusion and reversing CK2 inhibition allows for VAP recruitment. (A) Single plane confocal micrographs of HeLa cells expressing YFP-CK2β (yellow), infected with an *incV* mutant expressing IncV-3xFLAG (blue) and mCherry (red), and treated with 10μM CX-4945 (bottom panels), or not (top panels), for two hours at 18h pi and prior to the induction of IncV-3xFLAG expression at 20h pi. The merge is shown on the right. Scale bar is 5μm. (B) Quantification of the mean intensity of the YFP-CK2β signal within an object generated from the IncV-3xFLAG signal and normalized to the mean intensity of YFP-CK2β in the cytosol. Each dot represents one inclusion. Data show the mean and SEM of a combination of three independent experiments. ns, non-significant (Student's t-test). (C) Schematic depicting the experimental setup for the results in D-E. (D) Single plane confocal micrographs of HeLa cells expressing CFP-VAP (blue) and YFP-CK2β (yellow), infected with an *incV* mutant expressing IncV-3xFLAG under the control of the aTc inducible promoter and mCherry (red). Infections were performed in the absence of CX-4945 (No CX-4945) or presence of 10μM CX-4945 for the duration of the experiment (CX-4945). Alternatively, CX-4945 was present until 24h pi, when the cells were washed and incubated with media containing either aTc and CX-4945 (CX-4945 replaced) or aTc only (CX-4945 washout) for an additional hour. The merge is shown on the right. Scale bar is 5μm. (E) Quantification of the mean intensity of the CFP-VAP signal within an object generated from the YFP-CK2β signal and normalized to the mean intensity of CFP-VAP in the ER. Each dot represents one inclusion. Data show the mean and SEM of a combination of three independent experiments. One-way ANOVA and Tukey's post hoc test was performed. **** $P < 0.0001$; ns, non-significant.
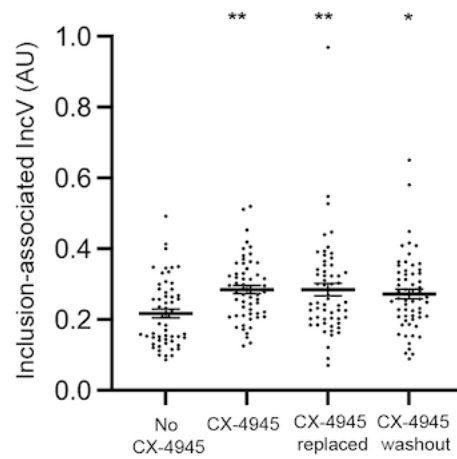
Figure 4.9 IncV inclusion localization is not affected upon CX-4945 replacement/washout treatment. Quantification of the volume of the indicated IncV-3xFLAG signal associated with the inclusion normalized to the volume of an object generated from the mCherry signal of the bacteria. Each dot represents one inclusion. The mean and SEM are shown. One-way ANOVA and Tukey's post hoc test was performed comparing drug treated cells to control cells. $P < 0.05$, ** $P < 0.01$.

Three serine residues in a C-terminal domain of IncV control CK2 and VAP recruitment to the inclusion, IncV hyper-phosphorylation and ER-Inclusion MCS formation.

To gain further mechanistic insight about the CK2-IncV-VAP interplay, and its role in ER-Inclusion MCS formation, we next determined which domain of IncV was important for the recruitment of CK2 to the inclusion by generating a series of C-terminal truncated IncV constructs (Figure 4.10A). These constructs, as well as the full length IncV (FL, 1-363), were cloned under the aTc inducible promoter and expressed from the *C. trachomatis incV* mutant strain. All IncV constructs similarly localized to the inclusion membrane (Figure 4.11A). HeLa cells expressing YFP-CK2β were infected with each of the complemented strains, and the ability of the truncated versions of IncV to recruit YFP-CK2β to the inclusion was assessed by confocal microscopy. Qualitative and quantitative analysis revealed that, compared to full length IncV$_{FL}$-3xFLAG, IncV$_{1-341}$-3xFLAG was no longer capable of recruiting YFP-CK2β to the inclusion, whereas IncV$_{1-356}$-3xFLAG was moderately affected (Figure 4.12A-B). Additionally, strains expressing IncV$_{1-341}$-3xFLAG also exhibited a significant reduction in IncV-associated VAP compared to IncV$_{FL}$- or IncV$_{1-356}$-3xFLAG (Figure 4.12C-D). Altogether, these results demonstrate that a C-terminal region of IncV, between amino acids 342 and 356, is required for the IncV-dependent CK2 recruitment to the inclusion and subsequent VAP association with the inclusion.

The primary amino acid structure of the IncV domain necessary for CK2 recruitment ($_{342}$SSESSDEESSSDSS$_{356}$) contains seven CK2 recognition motifs (S/T-x-x-D/E/pS/pY) (223) (Figure 4.10A). Three of them do not require priming by

phosphorylation of the fourth serine or tyrosine residue and could result in the direct CK2-dependent phosphorylation of IncV on serine residues S_{345}, S_{346}, and S_{350}, hereby facilitating the assembly of the IncV-VAP tether. To test this hypothesis, all three serine residues were substituted for unphosphorylatable alanine residues (IncV$_{S345A-S346A-S350A}$ referred to as IncV$_{S3A}$). HeLa cells expressing YFP-CK2β or YFP-VAP were infected with *C. trachomatis incV* mutant strains expressing IncV$_{WT}$- or IncV$_{S3A}$-3xFLAG. The cells were fixed at 24h pi, immunostained with anti-FLAG antibody, and analyzed by confocal immunofluorescence microscopy. IncV$_{WT}$- and IncV$_{S3A}$-3xFLAG displayed similar inclusion localization (Figure 4.11B). However, qualitative and quantitative analysis revealed that in comparison to IncV$_{WT}$-3xFLAG, IncV$_{S3A}$-3xFLAG expression resulted in a significant decrease in both CK2β and VAP recruitment to the inclusion (Figure 4.10B-E). Altogether, these results indicate that serine residues S_{345}, S_{346}, and S_{350} located in a C-terminal motif of IncV, are critical for CK2 and VAP recruitment to the inclusion.

To determine if IncV$_{S3A}$ failed to recruit VAP to the inclusion because of a lack of IncV phosphorylation, we assessed IncV$_{S3A}$ apparent molecular weight by western blot analysis of lysates from HeLa cells infected with a *C. trachomatis incV* mutant expressing IncV$_{WT}$- or IncV$_{S3A}$-3xFLAG. Compared to IncV$_{WT}$-3xFLAG, which as previously observed ran as a doublet corresponding to both phosphorylated and unphosphorylated species of IncV (Figure 4.10F, lane 1), the apparent molecular weight of IncV$_{S3A}$-3xFLAG (Figure 4.10F, lane 2), was identical to that of unphosphorylated IncV$_{WT}$-3xFLAG upon treatment with the CK2 inhibitor CX-4945 (Figure 4.10F, lane 3). These results indicated that IncV$_{S3A}$ is unphosphorylated.

To more directly demonstrate that, in absence of IncV hyper-phosphorylation, the lack of VAP association with the inclusion membrane correlates with a defect in ER-Inclusion MCS formation, cells infected with a *C. trachomatis incV* mutant expressing IncV$_{WT}$- or IncV$_{S3A}$-3xFLAG were processed for electron microscopy. Qualitative assessment of the micrographs revealed that the integrity of the inclusion membrane and ER-Inclusion MCS were preserved in both conditions, based on the intermembrane distance of 10-20 nm between the ER tubules and the inclusion membrane, and on the presence of ribosomes on the cytosolic face of the ER tubules (Figure 4.13A-B). However, 61.9% (39/63) of the S3A inclusion sections displayed no ER in association with the inclusion membrane, compared to only 6.6% (4/61) of the WT inclusion sections. Additionally, quantification of the proportion of inclusion membrane associated with the ER indicated a significant reduction of ER-Inclusion MCS formation upon IncV$_{S3A}$ expression, compared to IncV$_{WT}$ (Figure 4.10G-H and Figure 4.13C-D). We note that some levels of ER-Inclusion MCS is expected with IncV$_{S3A}$ because of redundant tethering mechanism(s) (68). Altogether, these results indicate that the CK2-dependent phosphorylation of IncV controls assembly of the IncV-VAP tether and ER-Inclusion MCS formation.

Finally, we determined if phosphorylation of S$_{345}$, S$_{346}$, and S$_{350}$ was sufficient to mediate the *in vitro* IncV-VAP interaction observed upon CK2 phosphorylation of IncV (Figure 4.1D), by substituting S$_{345}$, S$_{346}$, and S$_{350}$ for phosphomimetic aspartic acid residues. The corresponding IncV construct, referred to as IncV$_{S3D}$, was purified from *E. coli* and tested for VAP binding *in vitro*. IncV$_{S3D}$ did not result in a significant increase in VAP binding compared to IncV$_{WT}$ (Figure 4.14). While we cannot exclude that the

phosphomimetic mutations failed to mimic phosphorylation, these results indicated that, although critical for CK2 recruitment, IncV hyper-phosphorylation status, and assembly of the IncV-VAP tether at the ER-inclusion MCS, phosphorylation of S_{345}, S_{346}, and S_{350} alone is not sufficient to promote VAP binding *in vitro*, suggesting that additional IncV phosphorylation sites are required to promote optimal interaction between IncV and VAP.
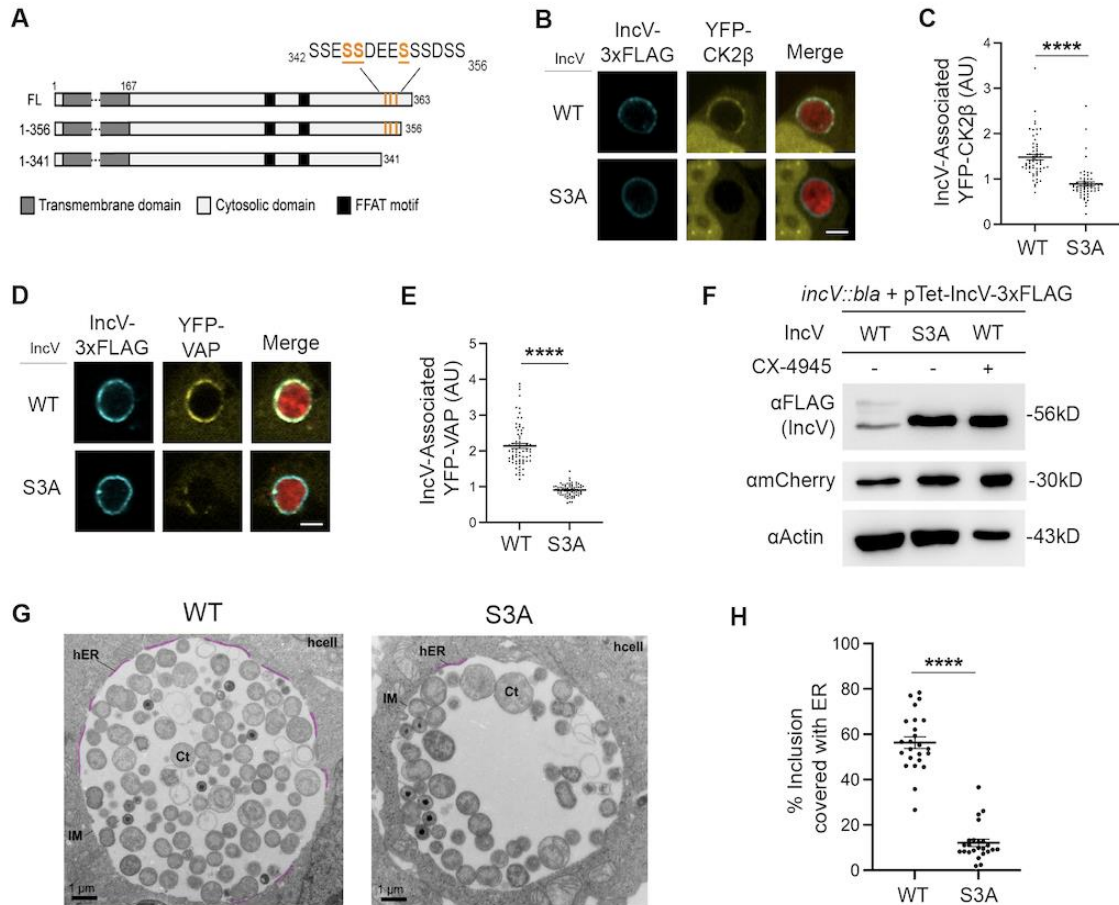
Figure 4.10 Three serine residues in a C-terminal domain of IncV mediate CK2 and VAP recruitment to the inclusion, IncV phosphorylation, and ER-Inclusion MCS formation. (A) Schematic depicting truncated IncV constructs. The numbers indicate the amino acid position within the IncV protein sequence. CK2 phosphorylation sites that do not require priming are indicated in orange. (B, D) Single plane confocal images of HeLa cells expressing YFP-CK2β (B) or YFP-VAP (D) (yellow), infected with a *C. trachomatis incV* mutant expressing mCherry (red) and IncV$_{WT}$- (WT) or IncV$_{S345A/S346A/S350A}$-3xFLAG (S3A) (blue). The merge is shown on the right. Scale bar is 5µm. (C, E) Quantification of the mean intensity of YFP-CK2β (C) and YFP-VAP (E) within the IncV object normalized to the mean intensity of YFP-CK2β in the cytosol and YFP-VAP in the ER, respectively. Data show the mean and SEM of a combination of three independent experiments. ****$P < 0.0001$ (Student's t-test). (F) Western blot of lysates of HeLa cells infected with a *C. trachomatis incV* mutant expressing IncV$_{WT}$-3xFLAG (WT), IncV$_{S3A}$-3xFLAG (S3A), or expressing IncV$_{WT}$-3xFLAG and treated with 10 µM CX-4945 as described in Figure 3C (WT; CX-4945 +) and probed with anti-FLAG (top blot), anti-mCherry (middle blot), and anti-actin (bottom blot) antibodies. (G) Transmission electron micrographs of sections of HeLa cells infected with a *C. trachomatis incV* mutant expressing IncV$_{WT}$- (WT) or IncV$_{S3A}$-3xFLAG (S3A). Representative sections across a whole inclusion are shown. ER-Inclusion MCS are highlighted in pink. Corresponding images without the highlighted MCS are shown in Figure 4.13C-D. Ct: *Chlamydia trachomatis*; IM: inclusion membrane; hER: host endoplasmic reticulum; hcell: host cell cytosol. Scale bars are 1 µm. (H) Quantification of the

percentage of the inclusion membrane covered with host ER. Each dot represents one section across a whole inclusion. Data show the mean and SEM for 24 representative electron micrographs per condition. **** P <0.0001 (Student's t-test). Data presented in G and H generated by Isabelle Coppens.
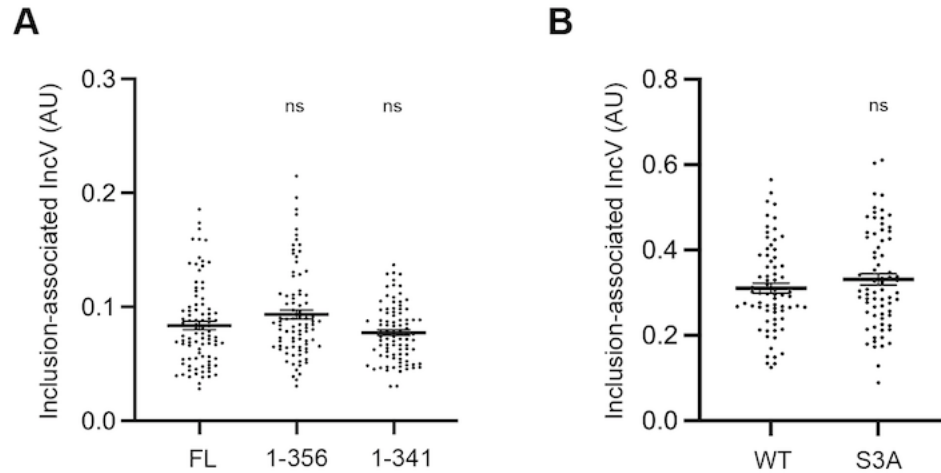
Figure 4.11 Truncation and alanine substitution of S245, S346 and S350 does not affect IncV localization to the inclusion membrane. (A-B) Quantification of the volume of the indicated IncV-3xFLAG signal associated with the inclusion normalized to the volume of an object generated from the mCherry signal of the bacteria. Each dot represents one inclusion. The mean and SEM are shown. One-way ANOVA and Tukey's post hoc test (A) were performed Student's t-test (B) comparing truncations to full length (A), and alanine substitution mutant to wild type (B). ns non-significant. Data presented in A generated by Rebecca Murray.
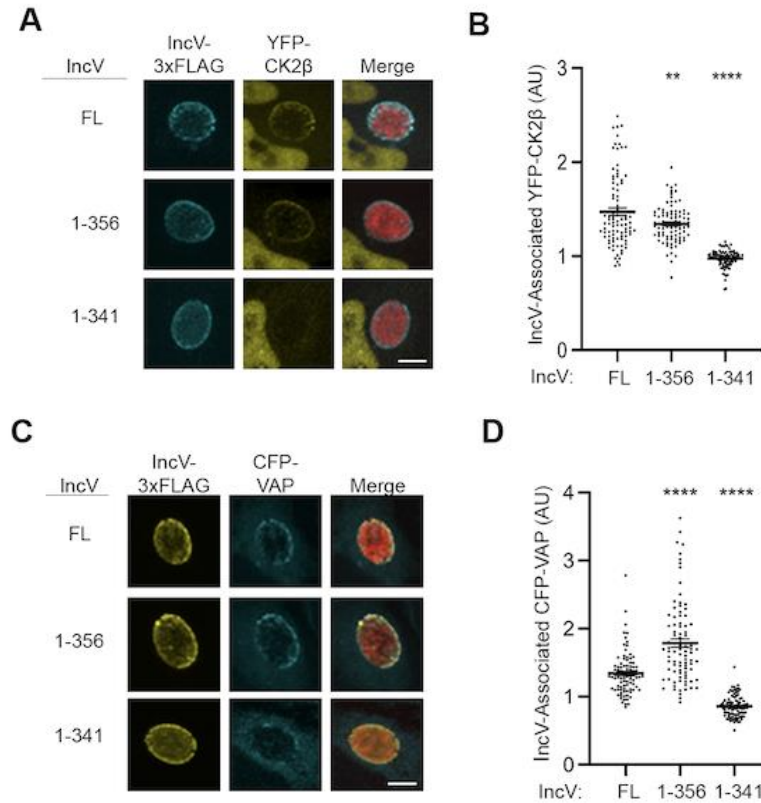
Figure 4.12 A C-terminal domain of IncV mediates VAP recruitment to the inclusion. (A) 3-dimensional reconstruction of confocal images of HeLa cells expressing YFP-CK2β (yellow) and infected with a *C. trachomatis incV* mutant expressing mCherry constitutively (red) and IncV-3xFLAG (full length (FL) or truncated (1-356, or 1-341) (blue). The merge is shown on the right. Scale bar is 5μm. (B) Quantification of the mean intensity of YFP-CK2β within an object generated from the IncV-3xFLAG signal and normalized to the mean intensity of YFP-CK2β in the cytosol. Each dot represents one inclusion. Data show the mean and SEM of a combination of three independent experiments. One-way ANOVA and Tukey's post hoc test was performed comparing truncations to full length. ** $P < 0.01$, **** $P < 0.0001$. (C) 3-dimensional reconstruction of confocal images of HeLa cells expressing CFP-VAP (blue) and infected with a *C. trachomatis incV* mutant expressing mCherry constitutively (red) and IncV-3xFLAG (full length (FL) or truncated (1-356, or 1-341) (yellow). The merge is shown on the right. Scale bar is 5μm. (D) Quantification of the mean intensity of CFP-VAP within an object generated from the IncV-3xFLAG signal and normalized to the mean intensity of CFP-VAP in the cytosol. Each dot represents one inclusion. Data show the mean and SEM of a combination of three independent experiments. One-way ANOVA and Tukey's post hoc test was performed comparing truncations to full length. **** $P < 0.0001$. Data generated by Rebecca Murray.
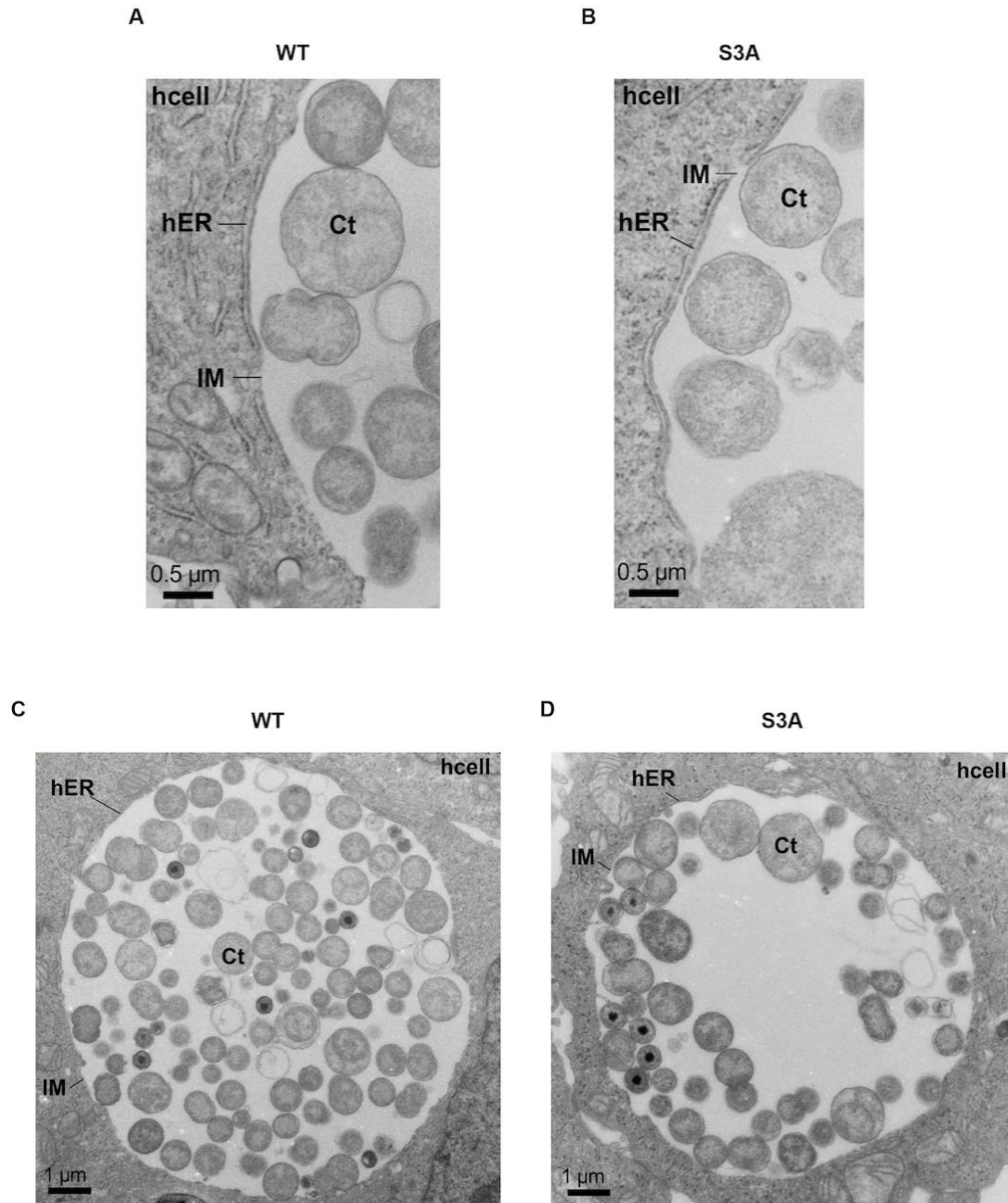
Figure 4.13 Ultrastructural analysis of ER-Inclusion MCS. (A-B) High magnification transmission electron micrographs of sections of MCS between the ER and the inclusion of *C. trachomatis incV* mutant expressing IncV$_{WT}$- (WT) or IncV-$_{S3A}$3xFLAG (S3A). Scale bar, 0.5 µm. (C-D) Transmission electron micrographs of sections of HeLa cells infected with a *C. trachomatis incV* mutant expressing IncV$_{WT}$- (WT) or IncV$_{S3A}$-3xFLAG (S3A) as shown in Figure 4.10G but without the mask highlighting the ER-inclusion MCS. Section across a whole inclusion is shown. Scale bars are 1 µm. Ct: *Chlamydia trachomatis*; IM: inclusion membrane; hER: host endoplasmic reticulum; hcell: host cell cytosol. Data generated by Isabelle Coppens.

128
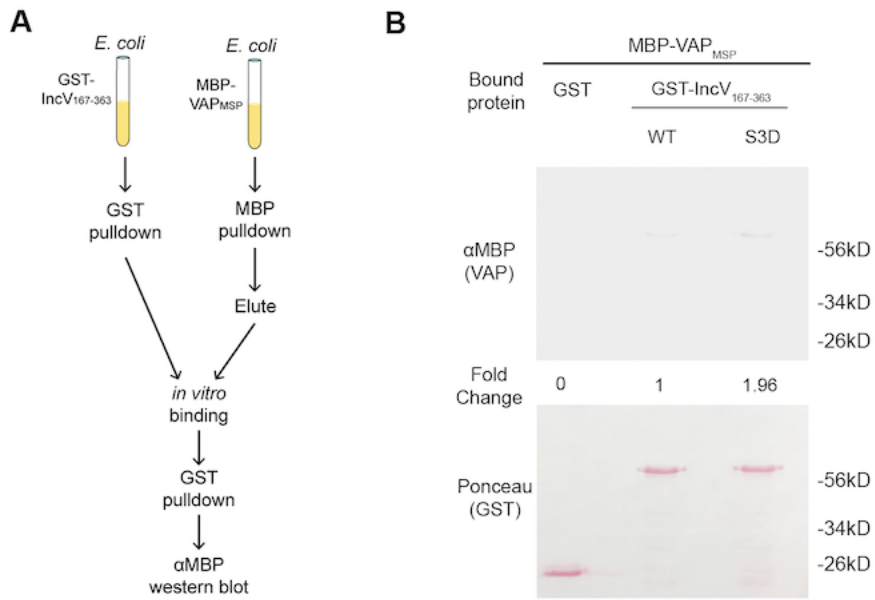
Figure 4.14 Phosphomimetic mutation of three serine residues in the C-terminal domain of IncV is not sufficient to promote the IncV-VAP interaction in vitro. (A) Schematic depicting the experimental setup for results in B. (B) *In vitro* binding assay using GST, GST-IncV$_{WT}$, or GST-IncV$_{S3D}$ purified from *E. coli*, immobilized on glutathione beads, and combined with MBP-VAP purified from *E. coli*. The top panel was probed with anti-MBP and the bottom panel was the same membrane stained with Ponceau S to detect the GST construct. Note that the IncV and VAP constructs, only include the cytosolic domain of IncV (aa 167-363) and the MSP domain of VAP, respectively.

Phosphorylation of T_{265} in the non-canonical FFAT of IncV contributes to the IncV-VAP interaction

We have previously shown that IncV displays one non-canonical ($_{262}S^1F^2H^3T^4P^5P^6N^7{}_{268}$) and one canonical FFAT motif ($_{286}E^1Y^2M^3D^4A^5L^6E^7{}_{292}$) (Figure 4.15A) (68). In agreement with position 2 of a FFAT motif being a phenylalanine or a tyrosine residue critical for VAP-FFAT interactions (154, 224), we had shown that alanine substitution of residue in position 2 of each motif, individually (IncV$_{F263A}$ or IncV$_{Y287A}$) and in combination (IncV$_{F263A/Y287A}$), led to a partial and full reduction of the IncV-VAP interaction, respectively, indicating that both FFAT motifs cooperate for VAP binding (68). Recently, Di Mattia et al., identified a new class of FFAT motifs referred to as phospho-FFAT motifs in which the acidic residue in position 4 is replaced by a phosphorylatable residue, such as serine or threonine (158). The presence of a phosphorylatable threonine residue in position 4 of the non-canonical FFAT motif of IncV (T_{265}) (Figure 4.15A) suggests that, as proposed by Di Mattia et al., the non-canonical FFAT of IncV could be a phospho-FFAT motif. To test this hypothesis, T_{265} was substituted for an alanine residue either individually (IncV$_{T265A}$), or in combination with alanine mutation of the tyrosine residue in position two of the canonical FFAT (IncV$_{T265A/Y287A}$). In parallel, a phosphomimetic mutation was generated by substituting both T_{265} to an aspartic acid residue and the proline residue at position 266 (P_{266}) to an alanine residue, as described by Di Mattia et al (158), either individually (IncV$_{T265D/P266A}$) or in combination with mutation in the canonical FFAT (IncV$_{T265D/P266A/Y287A}$). HeLa cells expressing YFP-VAP were infected with the *incV* mutant strain of *C. trachomatis* expressing IncV$_{T265A}$-, IncV$_{T265A/Y287A}$-, IncV$_{T265D/P266A}$-, or IncV$_{T265D/P266A/Y287A}$-

3xFLAG. Cells infected with *incV* mutant strains expressing IncV$_{WT}$-, IncV$_{Y287A}$-, or IncV$_{F263A/Y287A}$-3xFLAG were included as controls. The cells were fixed at 24h pi and immunostained with anti-FLAG antibody, followed by qualitative and quantitative analysis of confocal immunofluorescence microscopy images (Figure 4.15B-C). Although a few of the IncV constructs displayed statistically significant decreases in their inclusion localization (Figure 4.16A), the reduction was minor, leaving a substantial amount of IncV on the inclusion membrane (84-89% of the WT on average) and most likely accounts for very little, if any, to the phenotypes described throughout our study. As previously observed (68), IncV$_{WT}$ exhibited a strong association of YFP-VAP with the inclusion membrane, while IncV$_{Y287A}$ and IncV$_{F263A/Y287A}$ exhibited a significant partial and full loss of inclusion associated YFP-VAP, respectively (Figure 4.15B-C). Similarly, IncV$_{T265A}$ and IncV$_{T265A/Y287A}$ exhibited partial and complete loss of VAP association with the inclusion, respectively (Figure 4.15B-C) indicating that substitution of T$_{265}$ to a non phosphorylatable residue impacted the ability of the non-canonical FFAT motif to mediate the VAP-FFAT interaction. On the contrary, IncV$_{T265D/P266A}$ resulted in VAP inclusion association similar to IncV$_{WT}$, indicating that phosphomimetic mutation of IncV non-canonical FFAT resulted in optimal VAP binding during infection. However, IncV$_{T265D/P266A/Y287A}$ did not result in the expected intermediate VAP recruitment observed with IncV$_{Y287A}$, suggesting that the T265D/P266A mutation of the non-canonical FFAT was not sufficient to rescue VAP binding in the background of an inactivated canonical FFAT.

We next investigated if phosphomimetic mutation of T$_{265}$ of the IncV non-canonical FFAT (IncV$_{T265D/P266A}$) was sufficient to promote the IncV-VAP interaction *in*

vitro. GST-IncV$_{T265D/P266A}$ failed to interact with MBP-VAP$_{MSP}$ in our vitro assay (Figure 4.17), suggesting that phosphorylation of T$_{265}$ is not sufficient for full VAP binding under these conditions.

To further investigate if the non-canonical FFAT of IncV could function as a phospho-FFAT motif, we used a VAP$_{K50L}$ mutant. The K50L mutation resides in the MSP domain of VAP and has been shown to specifically affect VAP binding to phospho-FFAT motifs, but not to canonical FFAT (158). Using a similar experimental set up as in Figure 4.15B-C, we investigated the ability of YFP-VAP$_{K50L}$ to associate with inclusions harboring bacteria expressing IncV$_{WT}$-, IncV$_{Y287A}$-, or IncV$_{T265A}$-3xFLAG (Figure 4.18). Cells expressing YFP-VAP$_{WT}$ and infected with bacteria expressing IncV$_{WT}$- or IncV$_{F263A/Y287A}$-3xFLAG were used as positive and negative controls, respectively. In comparison to these controls, IncV$_{WT}$ led to an intermediate recruitment of VAP$_{K50L}$ to the inclusion, presumably due to binding to the canonical FFAT only, which was supported by the inability of IncV$_{Y287A}$ to recruit VAP$_{K50L}$. IncV$_{T265A}$ also led to an intermediate recruitment of VAP$_{K50L}$ to the inclusion, which was attributed to binding to the canonical FFAT. However, IncV$_{T265A}$ displayed decreased efficiency in VAP recruitment compared to IncV$_{WT}$, suggesting that in the context of IncV, VAP$_{K50L}$ may have low residual affinity to the non-canonical FFAT containing a phosphomimetic mutation of T$_{265}$, and/or reduced activity towards the canonical FFAT.

Although T$_{265}$ cannot be phosphorylated by CK2, given the CK2-dependent role of S$_{345}$, S$_{346}$ and S$_{350}$ in controlling the global level of phosphorylation of IncV, we investigated if CK2 could indirectly affect phosphorylation of T$_{265}$, by testing the ability of the T$_{265}$ phosphomimetic mutation to bypass the need for CK2 for VAP recruitment to

the inclusion. We generated an IncV$_{T265D/P266A/S3A}$ construct and quantified VAP recruitment to inclusions harboring bacteria expressing IncV$_{T265D/P266A/S3A}$-3xFLAG (Figure 4.15D-E). IncV$_{WT}$- and IncV$_{S3A}$-3xFLAG were used as positive and negative controls, respectively. IncV$_{T265D/P266A/S3A}$ inclusion localization was not affected (Figure 4.16B) and led to a partial rescue of VAP recruitment to the inclusion, compared to the controls (Figure 4.15D-E). These results indicate that CK2 and S$_{345}$, S$_{346}$, and S$_{350}$ play an indirect role in the phosphorylation of T265 of the IncV non-canonical FFAT motif.

Altogether, because of inconclusive results with the VAP$_{K50L}$ mutant, it remains unclear if IncV non-canonical FFAT acts as a phospho-FFAT. However, the above results indicate that phosphorylation of T$_{265}$ of IncV non-canonical FFAT is indirectly controlled by CK2 and contributes, but is not sufficient, to mediate the IncV-VAP interaction, suggesting that additional residues must be phosphorylated to ensure full IncV-VAP interaction.
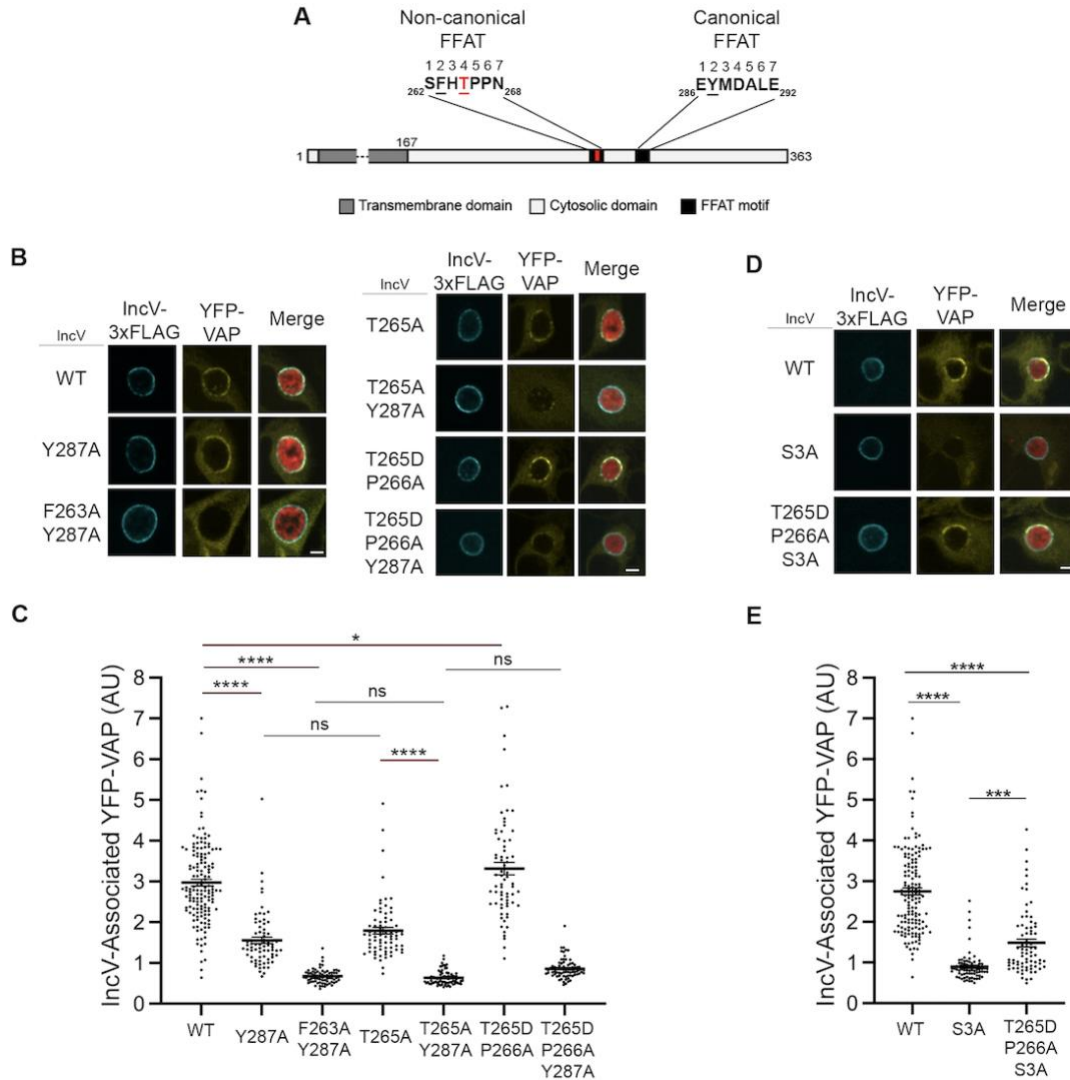
Figure 4.15 Phosphorylation of T265 in the non-canonical FFAT motif of IncV contributes to the IncV-VAP interaction. (A) Schematic depicting the IncV protein. The transmembrane domain, the cytosolic domain, and the non-canonical and the canonical FFAT motif cores are indicated in dark grey, light grey and black, respectively. The amino acid sequence of the FFAT motif cores is shown. Numbers 1-7 indicate the amino acid position within the FFAT motif cores, other numbers indicate the amino acid position within the IncV protein sequence. Residues at position 2 of the FFAT motif cores are in black and underlined. Threonine 265 at position 4 of the non-canonical FFAT is in red and underlined. (B) Single plane confocal images of HeLa cells expressing YFP-VAP (yellow), infected with a *C. trachomatis incV* mutant expressing mCherry constitutively (red) and IncV$_{WT}$- (WT), IncV$_{Y287A}$- (Y287A), IncV$_{F263A/Y287A}$ (F263A/Y287A), IncV$_{T265A}$- (T265A), IncV$_{T265A/Y287A}$- (T265A/Y287A), IncV$_{T265D/P266A}$- (T265D/P266A), or IncV$_{T265D/P266A/Y287A}$-3xFLAG (T265D/P266A/Y287A) (blue). The merge is shown on the right. Scale bar is 5µm. (C, E) Quantification of the mean intensity of YFP-VAP within an object generated from the IncV-3xFLAG signal corresponding to the indicated IncV constructs, and normalized to the mean intensity of YFP-VAP in the ER. Each dot represents one inclusion. Data show the mean and SEM of three to six independent experiments. One-way ANOVA and Tukey's post hoc test was performed. ns non-significant, * $P <0.05$, *** $P <0.001$, **** P

<0.0001. (D) Single plane confocal images of HeLa cells expressing YFP-VAP (yellow), infected with a *C. trachomatis incV* mutant expressing mCherry constitutively (red) and IncV$_{WT}$- (WT), IncV$_{S3A}$- (S3A) or IncV$_{T265D/P266A/S3A}$-3xFLAG (T265D/P266A/S3A) (blue). The merge is shown on the right. Scale bar is 5μm.
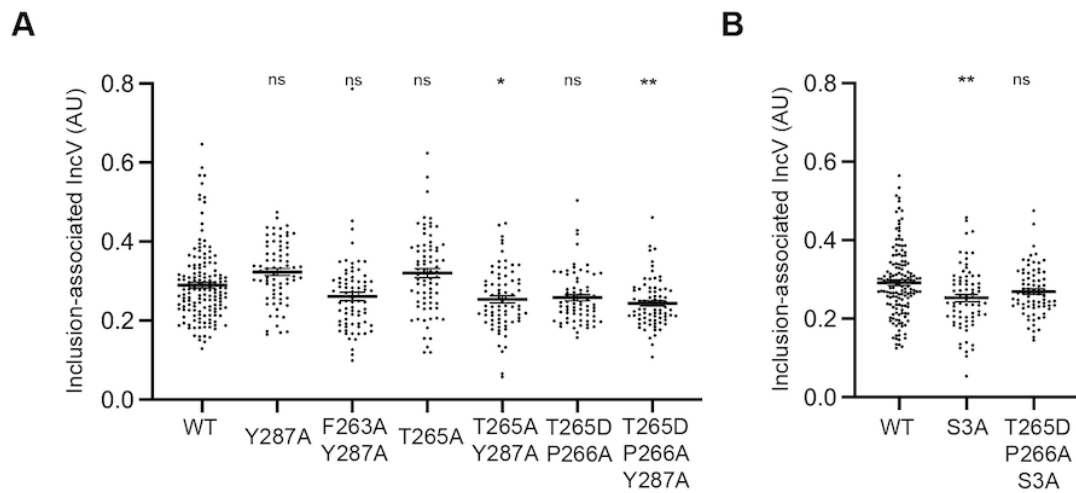
Figure 4.16 Inclusion localization of IncV variants with amino acid substitutions in the canonical and/or non-canonical FFAT motifs. (A-B) Quantification of the volume of the indicated IncV-3xFLAG signal associated with the inclusion normalized to the volume of an object generated from the mCherry signal of the bacteria. Each dot represents one inclusion. The mean and SEM are shown. One-way ANOVA and Tukey's post hoc test was performed comparing alanine or aspartic acid substitution to wild type. ns non-significant, * P <0.05, ** P <0.01.
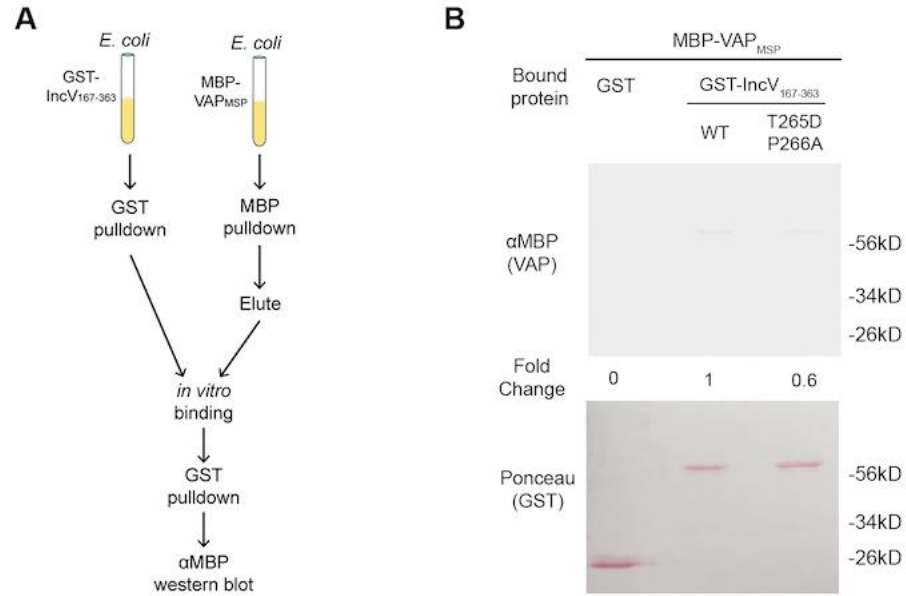
Figure 4.17 Phosphomimetic mutation of T$_{265}$ in the IncV non-canonical FFAT is not sufficient to promote the IncV-VAP interaction in vitro. (A) Schematic depicting the experimental setup for results in B. (B) *In vitro* binding assay using GST, GST-IncV$_{WT}$, or GST-IncV$_{T265D/P266A}$ purified from *E. coli*, immobilized on glutathione beads, and combined with MBP-VAP purified from *E. coli*. The top panel was probed with anti-MBP and the bottom panel was the same membrane stained with Ponceau S to detect the GST construct. Note that the IncV and VAP constructs, only include the cytosolic domain of IncV (aa 167-363) and the MSP domain of VAP, respectively.
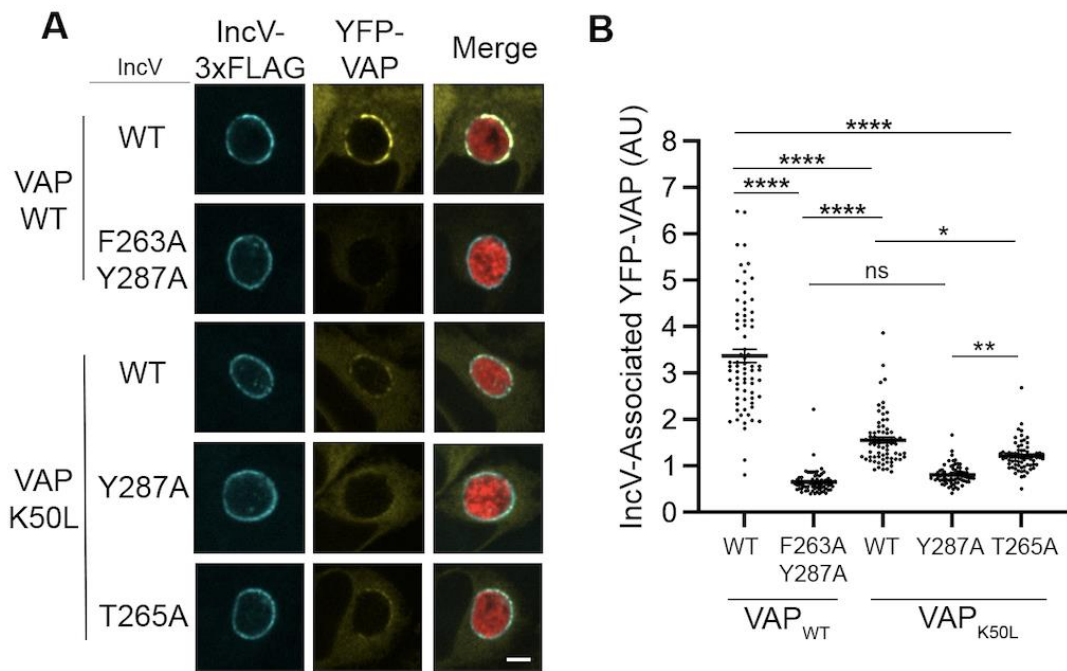
Figure 4.18 Recruitment of VAP_WT and VAP_K50L to *C. trachomatis* inclusions displaying wild-type or mutated IncV. (A) Single plane confocal images of HeLa cells expressing YFP-VAP_WT (VAP_WT) or -VAP_K50L (VAP_K50L) (yellow), infected with a *C. trachomatis incV* mutant expressing mCherry constitutively (red) and IncV_WT- (WT), IncV_F263A/Y287A- (F263A/Y287A), IncV_Y287A- (Y287A), or IncV_T265A-3xFLAG (T265A) (blue). The merge is shown on the right. Scale bar is 5μm. (B) Quantification of the mean intensity of YFP-VAP within an object generated from the IncV-3xFLAG signal corresponding to the indicated IncV constructs and normalized to the mean intensity of YFP-VAP in the ER. Each dot represents one inclusion. Data show the mean and SEM of three independent experiments. One-way ANOVA and Tukey's post hoc test was performed. ns non-significant, * $P < 0.05$, ** $P < 0.01$, **** $P < 0.0001$.

Phosphorylation of serine rich tracts upstream of IncV FFAT motifs substitute typical acidic tracts and are key for the IncV-VAP interaction

In addition to the seven amino acid core of the FFAT motif, VAP-FFAT mediated interactions also rely on the presence of acidic residues upstream of the core sequence, referred to as the acidic tract. It allows for the initial electrostatic interaction with VAP by interacting with the electropositive charge of the MSP domain before the FFAT core motif locks into its dedicated groove (212). We noted that, instead of typical acidic residues, the primary amino acid structures upstream of the IncV FFAT motifs are highly enriched in phosphorylatable serine residues (Figure 4.19A). We hypothesized that, if phosphorylated, these serine residues could serve as an acidic tract and facilitate the IncV-VAP interaction. To test this hypothesis, the 10 residues directly upstream of the non-canonical FFAT motif and the 8 residues directly upstream of the canonical FFAT motif were mutated to alanine residues (referred to as IncV$_{S/A}$). The ability of IncV$_{S/A}$-3xFLAG to recruit VAP to the inclusion was assessed. HeLa cells expressing YFP-VAP were infected with *C. trachomatis incV* mutant strains expressing either IncV$_{WT}$-, IncV$_{F263A/Y287A}$-, or IncV$_{S/A}$-3xFLAG under an aTc inducible promoter. The cells were fixed at 24h pi and analyzed by confocal immunofluorescence microscopy (Figure 4.19B). All IncV constructs were equally localized to the inclusion membrane (Figure 4.20). Qualitative and quantitative analysis revealed that expression of IncV$_{S/A}$-3xFLAG resulted in a significant decrease in YFP-VAP recruitment to the inclusion as observed with IncV$_{F263A/Y287A}$-3xFLAG and compared to IncV$_{WT}$-3xFLAG (Figure 4.18B-C). To determine if this decrease in VAP recruitment was due to a lack of CK2 recruitment, the ability of these strains to recruit YFP-CK2β to the inclusion was assessed by confocal

microscopy (Figure 4.21). All three strains recruited CK2 to the inclusion, indicating that the lack of VAP recruitment upon expression of IncV$_{S/A}$ was not due to a lack of CK2 recruitment.

We next determined if phosphomimetic mutation of the serine-rich tracts of IncV to aspartic acid residues (referred to as IncV$_{S/D}$) was sufficient to rescue the ability of the cytosolic domain of IncV expressed in *E. coli* to interact with the MSP domain of VAP in our VAP binding *in vitro* assay. As observed before, there was minimal binding of VAP$_{MSP}$ to IncV$_{WT}$ (Figure 4.19D, lane 2). However, we observed a 20-fold increase in VAP$_{MSP}$ binding to IncV$_{S/D}$ compared to IncV$_{WT}$ (Figure 4.19D, lane 3), indicating that phosphomimetic mutation of the serine-rich tracts is sufficient to promote the IncV-VAP interaction *in vitro*. Altogether, these results indicate that instead of typical acidic tracts, phosphorylated serine-rich tracts located upstream of IncV FFAT motifs are both necessary and sufficient for promoting the IncV-VAP interaction.

In order to confirm the role of IncV serine-rich tracts in promoting the IncV-VAP interaction during infection, we assessed the ability of IncV$_{S/D}$-3xFLAG to recruit VAP to the inclusion when expressed from an *incV* mutant strain of *C. trachomatis*. In comparison to IncV$_{WT}$ and all other mutated alleles used in this study, IncV$_{S/D}$-3xFLAG remained trapped within the bacteria and did not localize to the inclusion membrane (Figure 4.19E). These results suggest that phosphorylatable serine residues may have been selected over acidic residues to allow proper Type III translocation of IncV to the inclusion membrane.
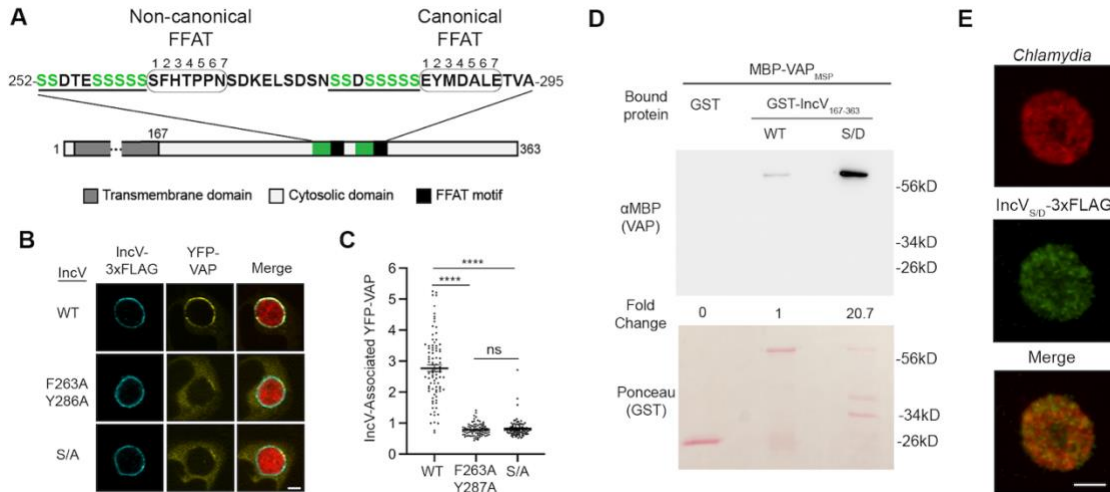
Figure 4.19 Phosphorylation of the serine tracts upstream of the IncV FFAT motifs facilitates the IncV-VAP interaction. (A) Schematic depicting the IncV protein. The transmembrane domain, the cytosolic domain, and the non-canonical and canonical FFAT motif cores are indicated in dark grey, light grey, and black, respectively. The amino acid sequence of the FFAT motif cores (Circled) and their respective upstream sequence is shown. The serine-rich tracts are underlined. Serine residues are in green. Numbers 1-7 indicate the amino acid position within the FFAT motif cores, other numbers indicate the amino acid position within the IncV protein sequence. (B) Single plane confocal images of HeLa cells expressing YFP-VAP (yellow), infected with a *C. trachomatis incV* mutant expressing mCherry constitutively (red) and IncV$_{WT}$-3xFLAG (WT), IncV$_{F263A/Y287A}$-3xFLAG (F263A/Y287A), or IncV$_{S/A}$-3xFLAG (S/A) (blue). The merge is shown on the right. Scale bar is 5μm. (C) Quantification of the mean intensity of YFP-VAP within an object generated from the IncV-3xFLAG signal and normalized to the mean intensity of YFP-VAP in the ER. Each dot represents one inclusion. Data show the mean and SEM of a combination of three independent experiments. One-way ANOVA with Tukey's post hoc test was performed. **** $P < 0.0001$. (D) *In vitro* binding assay using GST, GST-IncV$_{WT}$, or GST-IncV$_{S/D}$ purified from *E. coli*, and immobilized on glutathione beads and combined with MBP-VAP purified from *E. coli*. The top panel was probed with anti-MBP and the bottom panel was the same membrane stained with Ponceau S to detect the GST construct. Note that the IncV and VAP constructs, only include the cytosolic domain of IncV (aa 167-363) and the MSP domain of VAP, respectively. (E) Single plane confocal images of HeLa cells infected with a *C. trachomatis incV* mutant expressing mCherry consitutively (red) and IncV$_{S/D}$-3xFLAG (green). The merge is shown on the bottom. Scale bar is 5μm. Data presented in B and C generated by Samantha D'Spain.
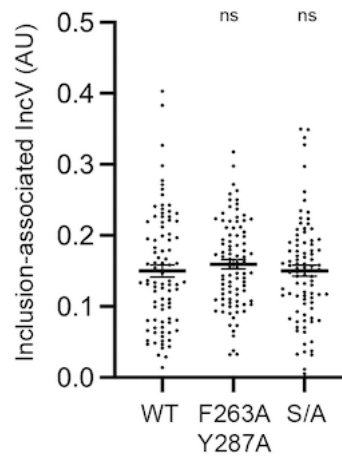
Figure 4.20 Alanine substitution of IncV serine tracts does not affect IncV inclusion localization. Quantification of the volume of the indicated IncV-3xFLAG signal associated with the inclusion normalized to the volume of an object generated from the mCherry signal of the bacteria. Each dot represents one inclusion. The mean and SEM are shown. One-way ANOVA and Tukey's post hoc test was performed comparing alanine substitution to wild type. ns non-significant. Data generated by Samantha D'Spain.
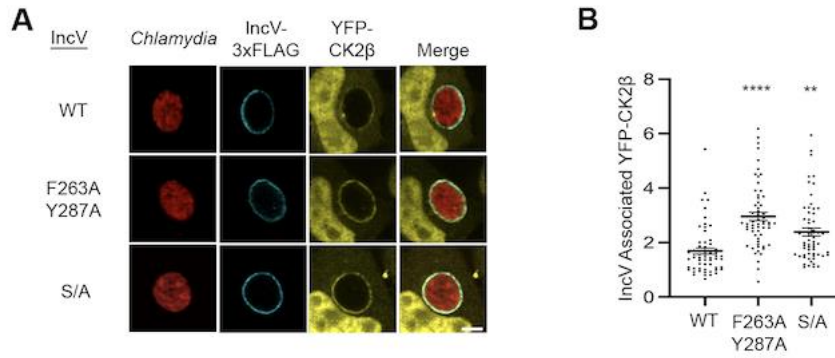
Figure 4.21 Alanine substitution of residues in position 2 of IncV FFAT motifs or of the serine rich tracts upstream of IncV FFAT motifs does not affect IncV-dependent CK2 recruitment to the inclusion. (A) Single plane confocal images of HeLa cells expressing YFP-CK2β (yellow) and infected with a *C. trachomatis incV* mutant expressing mCherry (red) and IncV$_{WT}$-3xFLAG (WT), IncV$_{F263A/Y287A}$-3xFLAG (F263A/Y287A), or IncV$_{S/A}$-3xFLAG (S/A) (blue). The merge is shown on the right. Scale bar is 5μm. (B) Quantification of the mean intensity of the YFP-CK2β within the IncV object normalized to the mean intensity of YFP-CK2β in the cytosol. Data show the mean and SEM of a combination of three independent experiments. One-way ANOVA with Tukey multiple comparisons test was performed to compare IncV$_{F263A/Y287A}$ and IncV$_{S/A}$ to IncV$_{WT}$. ** P <0.01, ****P < 0.0001. Data generated by Samantha D'Spain.

Discussion

IncV/CK2/VAP interplay in ER-Inclusion MCS formation

Based on our results, we propose the following model of assembly of the IncV-VAP tether leading to ER-Inclusion MCS formation during *Chlamydia* infection (Figure 4.22). Unphosphorylated IncV is translocated across the inclusion membrane by the T3SS. Upon insertion into the inclusion membrane and exposure to the cytosol (Figure 4.22, Step 1), IncV recruits the host kinase CK2 through a C-terminal domain containing three serine residues (S_{345}, S_{346} and S_{350}) that are part of CK2 recognition sites (Figure 4.22, Step 2). As a consequence, IncV becomes hyper-phosphorylated, including phosphorylation of T_{265} of the non- canonical FFAT and serine tracts directly upstream of the FFAT motifs (Figure 4.22, Step 3). These phosphorylation events lead to IncV interaction with VAP, tether assembly, and ER-Inclusion MCS formation (Figure 4.22, Step 4). Our data are consistent with CK2 playing a central role in initiating IncV hyper-phosphorylation (Figure 4.22, Step 2), however, additional kinases must contribute, especially for phosphorylation of the T_{265} (Figure 4.22, Step 3). Importantly, the post-translocation phosphorylation of IncV ensures optimal VAP binding while preserving proper T3SS-mediated translocation of IncV to the inclusion membrane. Although this model was in part inferred from overexpression studies, it constitutes a framework to guide futures studies to further dissect the complex phosphorylation events leading to the assembly of the endogenous IncV-VAP tether. Below we discuss our results in the context of emerging regulatory mechanisms of cellular MCS assembly and highlight conserved and pathogen-specific mechanisms.
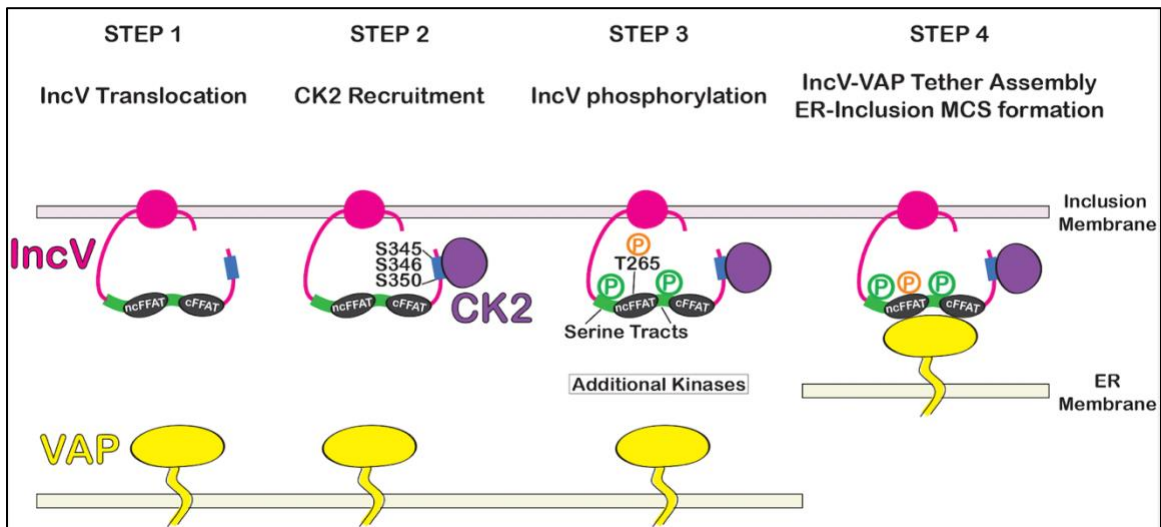
Figure 4.22 Model of assembly of the IncV-VAP tether at ER-Inclusion MCS. Step 1: After T3SS mediated translocation, unphosphorylated IncV (pink) is inserted into the inclusion membrane. Step 2: IncV recruits CK2 (purple) via 3 serine residues S345, S346 and S350 (blue) that are part of CK2 recognition motifs and located in a C-terminal domain of IncV. Step 3: IncV becomes hyperphosphorylated, including phosphorylation of the non-canonical FFAT on threonine residue T265 (orange) and the serine-rich tract (green) immediately upstream of FFAT core motifs (black). Additional kinases contribute to IncV phosphorylation. Step 4: IncV phosphorylation leads to full mimicry of FFAT motifs and binding to VAP (yellow) resulting in ER-Inclusion MCS formation. P: phosphorylated residues. ncFFAT: non-canonical FFAT. cFFAT: canonical FFAT. Light pink: inclusion membrane. Light yellow: ER membrane. Cartoon generated by Isabelle Derré.

IncV-dependent recruitment of CK2 to the inclusion

Few kinases phosphorylating VAP-dependent tethers have been identified (225, 226) and how they associate with MCS to phosphorylate their target has not been explored. Here, we show that IncV recruits CK2 to ER-Inclusion MCS through interaction with its C-terminal domain, a mandatory step for IncV hyper-phosphorylation. Three serine residues (S_{345}, S_{346}, and S_{350}) that match the CK2 recognition motifs (S-x-x-D/E) located in a C-terminal domain of IncV are essential for CK2 recruitment to the inclusion, and IncV phosphorylation. However, while CK2 was required for ER-Inclusion MCS formation during infection, and sufficient for IncV-VAP interaction *in vitro*, the introduction of phosphomimetic mutations at S_{345}, S_{346}, and S_{350} was not sufficient to promote the IncV-VAP interaction *in vitro*. While it is possible that the phosphomimetic mutations failed to mimic phosphorylation, it is more likely that additional phosphorylation sites exist. Kinase-substrate recognition is a complex process that goes beyond the simple recognition of a consensus sequence and can involve docking sites away from the phosphorylation sites (227). The cytosolic domain of IncV contains a large number of additional potential CK2 recognition sites. Among those, two serine residues, S_{253} and S_{283}, located in the serine tracts upstream of the non-canonical FFAT and the canonical FFAT respectively, are direct CK2 targets. Additionally, serine residues S_{257}, S_{258}, and S_{259} (serine tract upstream of the non-canonical FFAT), and S_{278}, S_{281}, S_{282}, and S_{284} (serine tract upstream of the canonical FFAT) can be phosphorylated upon priming the serine or tyrosine residue at the last position of the CK2 recognition motif (S/T-x-x-D/E/pS/pY). We therefore propose that alanine substitution of S_{345}, S_{346}, and S_{350} eliminates an essential docking site for subsequent CK2-mediated phosphorylation of

distal residues in the cytosolic domain of IncV, including the serine tracts next to the FFAT motifs (see below). Further investigation of the IncV-dependent recruitment of CK2 to ER-Inclusion MCS could offer some insights into kinase targeting to cellular MCS. Moreover, since intracellular pathogens often mimic cellular processes, our study points to a role for CK2 as a regulator of cellular MCS.

IncV non-canonical FFAT motif and the role of T$_{265}$

Phospho-null mutation of T$_{265}$ was detrimental to the IncV-dependent recruitment of VAP to the inclusion. Conversely, phosphomimetic mutation of T$_{265}$, in the context of an intact canonical-FFAT, resulted in efficient VAP association with the inclusion. These results are similar to those obtained with the phospho-FFAT motif containing proteins STARD3 and VPS13D (158, 228), and could therefore, suggest that , as previously proposed by Di Mattia et al., the non-canonical FFAT of IncV, via phosphorylation of T$_{265}$, is acting as a phospho-FFAT to mediate direct IncV-VAP interaction. However, in the absence of phospho-proteomic data demonstrating phosphorylation of T$_{265}$, and inconclusive and discrepant results discussed below, further investigation is required to validate that IncV non-canonical FFAT is a phospho-FFAT. First, in the context of a mutated canonical FFAT motif, phosphomimetic mutation of T$_{265}$ was unable to confer the anticipated partial rescue of VAP recruitment to the inclusion. The T265D/P266A phosphomimetic mutation was based on STARD3, where the proline residue directly downstream of the threonine residue had to be mutated to an alanine to introduce flexibility in the amino acid chain and allow for the aspartic acid to act as a phosphomimetic (158). This approach was successful to rescue VAP binding to VAP

147

interacting proteins containing only a single phospho-FFAT motif, like STARD3 and VPS13D (158, 228), and to IncV containing an additional wild-type canonical FFAT, but it may not be optimal for IncV in the context of a mutated canonical FFAT motif, perhaps because of the tertiary structure of the protein. Second, in the context of IncV, the VAP_{K50L} mutation led to partially inconclusive results, which could be due to low residual binding of VAP_{K50L} to IncV non-canonical FFAT motif and/or an overall reduced activity towards the canonical FFAT. Further characterization of the VAP_{K50L} mutant, especially in the context of proteins containing both a phosho-FFAT and a canonical FFAT, could settle these possibilities. Third, in vitro, the phosphomimetic mutation of T_{265} was not sufficient to promote VAP binding, suggesting that phosphorylation of T_{265} is not required in this setting. This conclusion is in line with the fact that, in vitro, CK2 phosphorylated IncV interacts with VAP, despite the fact that T_{265} is not a CK2 target and is therefore presumably not phosphorylated in this particular experiment. Collectively these results suggest that in vitro CK2 phosphorylation of IncV may result in suboptimal binding to VAP, which could be further increased during infection by phosphorylation of T_{265}. It is also possible that the dynamics of IncV-VAP interaction are different in vitro, compared to infection conditions, and that phosphorylation of T_{265} is not needed in this context. Alternatively, it is possible that phosphorylation of T_{265} is necessary in vivo for something other than VAP binding, such as the recruitment or activation of CK2, a step that may be bypassed in vitro given the high amount of CK2. Similarly, the positive in vitro interaction between $IncV_{S/D}$ and VAP, in the absence of T_{265} phosphorylation, could indicate either suboptimal in vitro binding that could be strengthened in vivo by phosphorylation of T_{265}, or a function

independent of VAP binding and leading to phosphorylation of the serine tracts. The latter would be consistent with the partial bypass of the need for CK2 for VAP association with the inclusion upon phosphomimetic mutation of T_{265}. This result also suggests that phosphorylation of T_{265} is dependent on, and temporally downstream of, CK2 binding to S_{345}, S_{346} and S_{350} in the C-terminal of IncV, potentially by allowing the recruitment of the yet to be identified kinase responsible for phosphorylating T_{265}.

The presence of a phospho-FFAT in IncV would add to the growing list of proteins that interact with VAP via a phospho-FFAT. These include STARD3 at ER-endosome contacts, the potassium channel Kv.2 at ER-PM contacts in neurons, Miga at ERMCS, and VPS13D at ER-mitochondria MCS (158, 225, 228, 229). Moreover, a putative phospho-FFAT in the norovirus protein NS2 is essential for interaction with VAP and viral replication (215), indicating that this mechanism of interaction with VAP might also be conserved amongst pathogens.

In the context of the STARD3-dependent formation of ER-endosome contacts, the presence of a single phospho-FFAT is proposed to act as a molecular switch to regulate contact formation (158). In the case of proteins that contain a combination of a canonical FFAT and a phospho-FFAT, such as PTPIP51, an ER-mitochondria contact protein (152), and potentially IncV, it is unclear how a most likely constitutive canonical FFAT and a regulated FFAT motif cooperate, if one is dominant over the other, and how advantageous such a combination is with respect with MCS regulation. In the case of IncV, one could speculate that the canonical FFAT motif allows for a baseline level of VAP recruitment to the inclusion and MCS formation while a phospho-FFAT could increase VAP recruitment beyond this baseline.

149

The IncV-VAP interaction is mediated by phosphorylatable serine tracts

In eukaryotic FFAT motifs, a number of negative charges upstream of the FFAT motif is proposed to facilitate the initial interaction with the MSP domain of VAP (212). This negatively-charged surface is conferred by acidic residues, but phosphorylated residues have been implicated in a few instances. The phosphorylation, by an unknown kinase, of a single serine residue six amino acids upstream of the CERT FFAT motif (S_{315}) enhances the CERT-VAP interaction (230). Similarly, the phosphorylation of three serine residues directly upstream of the FFAT-like motif of ACBD5 promotes VAP binding and peroxisome-ER contacts formation (226). We note that two of these serine residues (S_{259} and S_{261}) are putative CK2 targets, so it would be interesting to determine if CK2 also plays a role in assembly of the ACBD5-VAP tether. Another example are six serine residues, spread over 21 residues upstream of the core FFAT motif of Miga, shown to facilitate the Miga-VAP interaction (225). At least two kinases CKI and CaMKII, were required for Miga phosphorylation; however, other kinases are likely involved (225). In the case of IncV, the mimicry of an acidic track via phosphorylatable residues seems to be brought to the extreme, since the eight to ten amino acid stretch directly preceding each FFAT motif include 80 to 87% of serine residues, the remaining residues being acidic. Except for OSBP2/ORP4, which contains 6 acidic residues (including a phosphorylatable threonine), most acidic tracts contain few acidic residues directly upstream of the core of the FFAT motif (231). IncV is the first example of a FFAT motif-containing protein that displays serine tracts in place of acidic tracts. If built into the available FFAT motif identification algorithms, this feature could potentially reveal additional cellular VAP interacting proteins (158, 211).

Phospho-regulation and pathogenesis

During co-evolution with the mammalian host, obligate intracellular bacteria such as *Chlamydia* have evolved to take advantage of and manipulate cellular machinery. One mechanism is *via* molecular mimicry, in which the pathogen mimics features that are uniquely present in host proteins (232). In the case of IncV and acidic tracks in FFAT motifs, however, one could wonder why evolution would converge toward a mechanism relying on phosphorylation by host cell kinases, as opposed to simply selecting for genetically encoded acidic residues. In the case of *Chlamydia* Inc proteins, it is possible that tracks of aspartic acid or glutamic acid residues would create an excess of negative charges that may interfere with Type III secretion. In support of this notion, we found that *Chlamydia* IncV is no longer properly translocated to the inclusion membrane when the serine tracts are mutated to aspartic acid residues, and instead remains trapped within the bacteria. Our results support the notion that the recruitment of CK2 to the inclusion supports the assembly of the IncV-VAP tether. In addition, we cannot exclude the possibility that the recruitment of a phosphatase to ER-Inclusion MCS may contribute to the disassembly of IncV-VAP tethers, as shown for the calcineurin-dependent disassembly of Kv.2-VAP ER-PM contacts in neurons (233). A combination of host cell kinases and phosphatases could thus regulate the dynamics of ER-Inclusion contact sites during the *Chlamydia* developmental cycle.

Materials and Methods.

Ethics statement.

All genetic manipulations and containment work were approved by the UVA Biosafety Committee and are in compliance with the section III-D-1-a of the National Institutes of Health guidelines for research involving recombinant DNA molecules.

Cell lines and bacterial strains.

HeLa cells (ATCC CCL-2) and HEK293 cells (ATCC CRL-1573) were maintained in DMEM high glucose (Gibco) containing 10% heat-inactivated fetal bovine serum (Gibco) at 37°C and 5% CO_2. *Chlamydia trachomatis* Lymphogranuloma venereum, type II (ATCC L2/434/Bu VR-902B) was propagated in HeLa cells as previously described (181). The *incV::bla* mutant strain of *C. trachomatis* (also known as *CT005::bla*) was obtained from Ted Hackstadt (NIH, Rocky Mountain Laboratories) (99). All cell lines and *Chlamydia* strains are routinely tested for mycoplasma contamination.

Plasmid construction.

Inserts were generated by PCR using the primers (IDT) listed in Table 4.1, and the Herculase DNA polymerase (Stratagene). The inserts were cloned as described below using restriction enzymes (NEB) and T4 DNA ligase (NEB).

Vectors for expression in mammalian cells.

The IncV-3xFLAG construct cloned in the pCMV-IE-N2-3xFLAG vector was previously described (68). The YFP-CK2α and YFP-CK2β plasmids were kind gifts from Claude Cochet and Odile Filhol-Cochet (Institut Albert Bonniot Departement Reponse et Dynamique Cellulaires) and were previously characterized (234). The pCFP-VAP and pYFP-VAP plasmids were constructed by cloning the VAPA open reading frame (ORF)

into pCMV-N1-CFP and pCMV-N1-YFP, respectively, using AgeI and HindIII restriction sites. The pYFP-VAP$_{K50L}$ plasmid was constructed by cloning the VAPA ORF encoding the K50L mutation (generated my overlapping PCR), into pCMV-N1-YFP using AgeI and HindIII restriction sites.

Vectors for expression in *E. coli*.

The GST-VAP$_{MSP}$ plasmid was previously described (68). MBP-VAP$_{MSP}$ was constructed by cloning the MSP domain of VAPA using NotI and BamHI into pMAL. The GST-IncV$_{167-363}$ fusion constructs WT, S3D, S/D or T265D/P266A were generated by cloning a DNA fragment encoding amino acids 167-363 of IncV with the indicated mutations into the BamHI and XhoI restriction sites of pGEX-KG.

Vectors for expression in *C. trachomatis*.

All the constructs to express the various IncV-3xFLAG constructs (1-356, 1-341, S3A, T265A, T265A/Y287A, T265D/P266A, T265D/P266A/Y287A, T265D/P266A/S3A, S/A, and S/D) from the aTc inducible promoter were generated by overlapping PCR and cloned into KpnI and NotI of the p2TK2$_{Spec}$-SW2 mCh(Gro) vector (182). The Tet-IncV$_{FL}$, Tet-IncV$_{F263A/Y287A}$, and Tet-IncV$_{Y287A}$ constructs were previously described (68).

***C. trachomatis* transformation and *incV::bla* complementation.**

Wild type *C. trachomatis* or an *incV* mutant (*incV::bla*) were transformed using our previously described calcium-based *Chlamydia* transformation procedure (182).

DNA transfection.

Cells were transfected with mammalian construct DNA according to manufacturer instructions with X-tremeGENE 9 DNA Transfection Reagent (Roche).

SDS-PAGE.

Cells were either directly lysed in 2x Laemmli buffer with 10mM DTT or IncV was purified as described in the immunoprecipitation and protein purification sections then suspended in a final concentration of 1x Laemmli buffer with 10mM DTT. Protein samples were separated using SDS-PAGE.

Immunoblotting.

After SDS/PAGE, proteins were transferred onto nitrocellulose membranes (GE Healthsciences). Prior to blocking, membranes were stained with Ponceau S in 5% acetic acid and washed in dH$_2$O. Membranes were incubated for 1 hour with shaking at room temperature in blocking buffer (5% skim milk in 1x PBS with 0.05% Tween). Membranes were then incubated with primary and secondary (HRP-conjugated) antibodies diluted in blocking buffer overnight at 4˚C and 1 hour at room temperature, respectively, with shaking. ECL Standard western blotting detection reagents (Amersham) were used to detect HRP-conjugated secondary antibodies on a BioRad ChemiDoc imaging system. CK2β was detected using secondary antibodies conjugated to Alexa Fluor 800 on Li-Cor Odyssey imaging system.

Antibodies.

The following antibodies were used for immunofluorescence microscopy (IF) and immunoblotting (WB): mouse monoclonal anti-FLAG [1:1,000 (IF); 1:10,000 (WB); Sigma], rabbit polyclonal anti-CK2β [1:200 (IF); 1:1,000 (WB); Bethyl Antibodies]; rabbit polyclonal anti-thiophosphate ester antibody [1:2000 (WB); Abcam], rabbit polyclonal anti-MBP [1:10,000 (WB); NEB], rabbit polyclonal anti-GAPDH [1:10,000 (WB);], rabbit polyclonal anti-mCherry [1:2,000 (WB); BioVision], rabbit polyclonal

anti-actin [1:10,000 (WB); Sigma], HRP-conjugated goat anti-rabbit IgG [1:10,000 (WB); Jackson], HRP-conjugated goat anti-mouse IgG [1:10,000 (WB); Jackson], Alexa Fluor 514-, 800-, or Pacific Blue-conjugated goat anti-mouse IgG [1:500 (IF); 1:10,000 (WB); Molecular Probes].

Immunoprecipitation of IncV-3xFLAG from HEK293 cells infected with C. *trachomatis*.

800,000 HEK293 cells were seeded into one well of a six-well plate (Falcon) and infected the following day with *C. trachomatis* at a multiplicity of infection (MOI) of 5. 8h pi, media containing 2ng/mL anhydrotetracycline (aTc) was added to the infected cells for 16 hours. 24 hours pi, culture media was removed from the cells and 500μL of lysis buffer (20 mM Tris pH 7.5, 150 mM NaCl, 2 mM EDTA, 1% Triton X-100, protease inhibitor mixture EDTA-free (Roche)) was added per well. Cells were lysed for 20 minutes at 4˚C with rotation. Lysates were centrifuged at 16,000xg for 10 minutes at 4˚C to pellet nuclei and unlysed cells. Cleared lysates were incubated with 10μL of anti-FLAG M2 affinity beads (Sigma) for 2 hours at 4˚C with rotation. The beads were washed with lysis buffer three times. Proteins were eluted with 50μL of 100μg/mL 3xFLAG peptide (Sigma) in 1x Tris-buffered saline. For cells transfected with pCMV-IE-N2-IncV-3xFLAG, cells were not infected, and the remainder of the protocol remained the same starting with removal of media and lysing.

Phosphatase assay.

Immunoprecipitation was performed as described above with the following changes: The beads were washed with 1x Tris-buffered saline (TBS) three times and proteins were eluted with 55μL of 100μg/mL 3xFLAG peptide (Sigma) in 1x TBS. 20μL of eluate was

combined with 2.5μL of 10mM MnCl2, 2.5μL of 10x PMP buffer (NEB), and 400 units

of lambda (λ) phosphatase (NEB) for 24 hours at 4˚C. The assay was halted by adding

5μL of 6x Laemmli buffer with 10mM DTT. Samples were boiled and 10μL of sample

was then used in SDS-PAGE.

DNA transfections and infections for microscopy.

HeLa cells were seeded onto glass coverslips and transfected with YFP-CK2 (α or β),

CFP-VAP, YFP-VAP or YFP-VAP$_{K50L}$ the following day. 24 hours post-transfection,

cells were infected with the indicated strain of *C. trachomatis* at a MOI of 1. 20 hours pi,

media containing 20ng/mL aTc (final concentration) was added for 4 hours to induce

expression of IncV-3xFLAG.

Immunofluorescence and confocal microscopy.

HeLa cells seeded on glass coverslips and infected with *C. trachomatis* were fixed 24

hours pi with 4% paraformaldehyde in 1x PBS for 20 minutes at room temperature then

washed with 1x PBS three times. The coverslips were sequentially incubated with

primary and secondary antibodies in 0.1% Triton X-100 in 1x PBS for 1 hour at room

temperature. For coverslips stained with anti-CK2β, antibodies were diluted in 0.5%

Triton X-100 and 5% BSA in 1x PBS. Coverslips were washed with 1x PBS three times

then mounted with glycerol containing DABCO and Tris pH 8.0. Confocal images were

obtained using an Andor iXon ULTRA 888BV EMCCD camera and a Yokogawa CSU-

W1 Confocal Scanner Unit attached to a Leica DMi8 microscope. 1 μm thick Z slices

covering the entirety of the cell were captured. Image analysis was performed using the

Imaris software. All the micrographs within a given figure panels are at the same scale.

Quantification of YFP-CK2β, CFP-VAP, and YFP-VAP inclusion association.

Quantification was performed using the Imaris imaging software. A step-by-step illustration of the quantification method is presented in Figure 4.6. Quantification of the IncV-3xFLAG associated with the inclusion was performed to ensure there was no defect in inclusion localization (Figure 4.6A). The sum of the voxels corresponding to the IncV-3xFLAG signal above the threshold set by the signal within the cytosol was calculated for IncV-3xFLAG and mCherry. Objects were edited such that IncV-3xFLAG colocalizing with the mCherry bacteria was removed. The IncV-3xFLAG volume was normalized to its corresponding inclusion volume to determine the inclusion association of IncV in arbitrary units [au]. The association of a given marker was then determined as follow (Figure 4.6B, YFP-VAP is shown as an example). Within the three-dimensional (3D) object generated from the raw signal of IncV-3xFLAG at the inclusion membrane, the mean intensity of the marker of interest was calculated and normalized to the mean intensity of the marker of interest within the cytosol surrounding the inclusion (average of 10 small 3D spheres) to determine the inclusion association of the marker of interest in arbitrary units [au]. A similar approach was used in Figure 4.8E, except that the mean intensity of CFP-VAP was determined within 3D objects generated from the raw signal of the YFP-CK2 at the inclusion and normalized to the CFP-VAP mean intensity in the cytosol.

Each experiment was performed in triplicate with at least 20-30 inclusions analyzed per condition per replicate. Unless specified, data from 3 independent replicates are combined into a single graph. Each point on the graph represents a single inclusion

with the average value and SEM shown. Student's t-tests or one-way ANOVA with multiple comparisons were performed.

Protein purification.

Expression of GST, GST-VAP$_{MSP}$, GST-IncV$_{167\text{-}363}$, GST-IncV$_{167\text{-}363}$ S/D or MBP-VAP$_{MSP}$ was induced for two hours by the addition of isopropyl-β-D-thiogalactopyranoside (0.1mM, final concentration) to a 10 mL culture of *E. coli* BL21-□DE3 at OD 0.8. Bacterial pellets were stored at -80˚C. Frozen pellets were thawed and resuspended in 800μL sonication buffer (20 mM Tris pH 7.5, 300 mM NaCl, 2 mM EDTA, 1 mM MgCl2, 1% Triton X-100, 1mM DTT, 1mM PMSF). The samples were sonicated using five 5-second pulses at 40% power then centrifuged at 13,000xg for 10 minutes at 4˚C. 40μL of glutathione Sepharose beads (GE) for GST-tagged constructs and 40μL of Amylose resin for MBP-tagged constructs were washed three times with sonication buffer then added to the cleared lysate and incubated for 2 hours at 4˚C with rotation. The beads were washed three times in TBS.

***In vitro* kinase assay.**

Protein bound glutathione Sepharose beads were resuspended in 1x NEBuffer™ for Protein Kinases supplemented with 1mM ATPγS and 10 units of CK2 (NEB) and incubated at 30˚C for 45 minutes. P-Nitrobenzyl mesylate (PNBM) was added to the kinase reaction at a final concentration of 2.4mM for 2 hours at room temperature in the dark. The PNBM alkylation reaction was quenched by adding an equal volume of 2x Laemmli buffer. Proteins were separated using SDS-PAGE on a 12% acrylamide gel then transferred to a nitrocellulose membrane. The membrane was stained with Ponceau S in 5% acetic acid to detect total protein then washed in dH$_2$O. The membrane was then

probed with anti-thiophosphate ester antibodies to detect phosphorylated proteins which were detected with HRP-conjugated secondary antibodies.

***In vitro* binding assay.**

First, GST, GST-IncV$_{167-363}$, GST-IncV$_{167-363}$ S/D, and MBP-VAP$_{MSP}$ were purified as described in protein purification. MBP-VAP$_{MSP}$ was eluted from amylose resin using 100μL 1x TBS supplemented with 10mM maltose monohydrate. GST, GST-IncV$_{167-363}$, or GST-IncV$_{167-363}$ S/D attached to glutathione beads were washed three times in sonication buffer. 500μL of sonication buffer containing 1.25μg MBP-VAP$_{MSP}$ was added to each tube with GST beads and binding was allowed to occur overnight at 4˚C with rotation. Following overnight binding, beads were washed three times in 1x TBS. After the final wash, all liquid was removed from the beads which were then suspended in 20μL 2x Laemmli buffer. The entire sample was separated by SDS-PAGE, proteins transferred to a nitrocellulose membrane which was stained with Ponceau S to detect the GST construct then probed with anti-MBP to detect MBP-VAP$_{MSP}$.

***In vitro* binding assay with IncV dephosphorylation.**

First, the phosphatase assay was performed with the following changes: 1,000,000 HEK293 cells stably transfected with pCMV-IE-N2-IncV-3xFLAG were seeded per 6 well. 6 wells were lysed in 500μL lysis buffer each and lysates from two wells were combined. 10μL of anti-FLAG beads were added per 1000μL cleared lysate for 2 hours at 4˚C with rotation. All beads were combined after the first wash, and proteins were eluted in 150μL elution buffer (130μL eluate collected).

Next, GST and GST-VAP$_{MSP}$ were purified as described in protein purification. Per phosphatase assay tube: 1.5μg of GST or GST-VAP$_{MSP}$ attached to beads (determined

empirically by comparison of Coomassie stained gel to BSA standard curve) were suspended in 500µL lysis buffer then added to tubes containing the IncV-3xFLAG-containing eluate (+/- phosphatase treatment). Binding was allowed to occur overnight at 4˚C with rotation.

To confirm that IncV dephosphorylation was successful, a set of control tubes were incubated with beads alone (no GST construct) in lysis buffer to mimic experimental conditions.

24 hours after binding, beads were washed three times in 1x TBS. After the final wash, all liquid was removed from the beads which were then suspended in 20µL 2x Laemmli buffer. The entire sample was separated by SDS-PAGE, proteins transferred to a nitrocellulose membrane which was stained with Ponceau S to detect the GST construct then probed with anti-FLAG to detect IncV-3xFLAG.

***In vitro* binding assay with CK2 phosphorylation of IncV.**

First, GST, GST-IncV$_{167-363}$, and MBP-VAP$_{MSP}$ were purified as described in protein purification. MBP-VAP$_{MSP}$ was eluted from amylose resin using 100µL 1x TBS supplemented with 10mM maltose monohydrate. 1.5µg of GST or GST-IncV$_{167-363}$ attached to glutathione beads (determined empirically by comparison of Coomassie stained gel to BSA standard curve) or beads alone were suspended in 1x NEBuffer™ for Protein Kinases with 200µM ATP (Thermo) and 100 units of CK2 (NEB) at 30˚C for 45 minutes. Beads were washed three times in sonication buffer. 1.25µg MBP-VAP$_{MSP}$ suspended in 500µL sonication buffer was added to each tube with beads and binding was allowed to occur overnight at 4˚C with rotation. 24 hours after binding, beads were washed three times in 1x TBS. After the final wash, all liquid was removed from the

beads which were then suspended in 20µL 2x Laemmli buffer. The entire sample was separated by SDS-PAGE, proteins transferred to a nitrocellulose membrane which was stained with Ponceau S to detect the GST construct then probed with anti-MBP to detect MBP-VAP$_{MSP}$.

GST-Pull down immunoblot quantification.

Immunoblots and Ponceau S staining were quantified using the ImageJ software (NIH). The immunoblot band intensity was normalized to the Ponceau S band intensity and the fold change determined relative to wild type or untreated conditions.

CK2 depletion using siRNA.

CK2 was depleted from cells using a pool of four siRNA duplexes or each duplex individually that was transfected with Dhamafect 1 transfection reagents. On day 0, one volume of 200nM siRNA in siRNA buffer was incubated with one volume of 5µL/mL of Dharmafect 1 transfection reagent in DMEM high glucose in a well for 20 minutes at room temperature. Two volumes of DMEM High Glucose supplemented with 20% FBS and 200,000 HeLa cells per mL were added to the well. Cells were incubated at 37˚C with 5% CO$_2$ for three days. The total volume for one 96 well was 120µL. The *CSNK2B* target sequence for each individual siRNA duplex was: A, CAACCAGAGUGACCUGAUU; B, GACAAGCUCUAGACAUGAU; C, CAGCCGAGAUGCUUUAUGG; D, GCUCUACGGUUUCAAGAUC. The efficacy of the knock down was quantified using the ImageJ software (NIH). The CK2 band intensity was normalized to the GAPDH band intensity and the knock down efficacy was determined relative to the mock condition.

CK2 inhibition using CX-4945 or GO289.

CK2 was inactivated using the CK2-specific inhibitor CX-4945 (0308, Advanced Chemblocks) or GO289 (17586, AOBIOUS), as described in the result sections.

Electron microscopy.

HeLa cells were infected with a strain of *C. trachomatis* expressing IncV$_{WT}$ or IncV$_{S3A}$-3xFLAG under the control of the aTc inducible promoter. Twenty hours pi cells were incubated in the presence of 20 ng/mL of aTc. Twenty-four hours pi, the samples were fixed in 2.5% glutaraldehyde in 0.1 M cacodylate buffer (pH 7.4) for 60 min at RT. After fixation, cells were scraped off and pelleted, as described previously (235). Ultrathin sections of infected cells were stained with osmium tetraoxide before examination with Hitachi 7600 EM under 80 kV equipped with a dual AMT CCD camera system. Quantitative measurement of length for the inclusion membrane and host ER elements attached to this membrane was performed using ImageJ on 24 representative electron micrographs at low magnification to ensure the entire inclusion fit into the field of view.

Acknowledgments.

Chapter 5:
Discussion, Future Directions, and Significance

Summary of Major Findings

My thesis work has shown that multiple host glycolytic enzymes localize to the *C. trachomatis* inclusion membrane (Figure 3.2). This host enzyme localization increases throughout development and corresponds to a decrease in bacterial glycolytic enzyme expression (Figure 3.5A and Figure 3.11), indicating that there is potential interplay between host and bacterial glycolytic metabolism throughout *C. trachomatis* development. We also showed that depletion of the host glycolytic enzyme Aldolase A resulted in a significant decrease in *C. trachomatis* inclusion size and infectious progeny production, indicating the importance of host glycolysis for *C. trachomatis* intracellular development.

Additionally, my thesis work has shown that the IncV-VAP tethering complex, and thus the formation of ER-inclusion MCS, is regulated through multiple host kinase-mediated phosphorylation events. We have specifically demonstrated a role for the host kinase CK2 in regulating the IncV-VAP tethering complex during infection (Figure 4.4). Moreover, we have shown that phosphorylation of the serine-rich tracts directly upstream of the two IncV core FFAT motifs allows for proper IncV translocation and plays a role in facilitating the IncV-VAP interaction (Figure 4.19E). Not only does this work implicate CK2 as a potential regulator of other cellular MCS, but could also allow for the identification of additional FFAT motif containing proteins if displaying a serine tract in place of an acidic tract is incorporated into current FFAT motif identification algorithms. Below, I discuss future directions and implications of my thesis work as well as the overall significance of my findings.

Identification of additional ER-Inclusion MCS components

A preliminary APEX proximity labeling screen to identify additional factors at ER-inclusion MCS identified six host glycolytic enzymes as being present at the inclusion membrane and we have since experimentally validated and characterized the localization of three of these host enzymes to the inclusion membrane (236). However, we observed that the host glycolytic enzymes appeared evenly distributed over the inclusion membrane, rather than in distinct patches as observed for other host factors present at ER-Inclusion MCS (Figure 3.2). Thus, our screen is likely not specific to ER-Inclusion MCS, but rather the inclusion membrane in general and needs to be optimized to specifically identify factors at these contact sites.

Optimization of proximity labeling to increase ER-inclusion MCS specificity

The specificity of our screen could be improved by fusing the proximity labeling enzyme to a bacterial protein present at ER-inclusion MCS, rather than a host protein that localizes to additional locations throughout the host cell. We have attempted to fuse both the BioID and APEX proximity labeling enzymes to IncV, a known bacterial component of ER-inclusion MCS, however the fusion proteins were defective in their catalytic activity or expression, respectively (Figure 2.2 and Figure 2.3). Since the APEX2 proximity labeling enzyme has been successfully fused to other Inc proteins (173-175), it is likely that the conformation of IncV is not amenable for use in proximity labeling. In future studies, the BioID or APEX2 enzymes could be fused to the other bacterial protein that is a known components of ER-inclusion MCS, IncD.

Advances in proximity labeling techniques have led to the generation of Split-BioID and Split-APEX2. In these techniques the BioID or APEX enzyme are divided into N- and C-terminal fragments that can then reform a functional enzyme upon being in close proximity (162). Future work could utilize one of these split construct systems where one half of the enzyme is attached to a bacterial Inc protein and the other half of the enzyme is attached to a known host interacting partner at ER-inclusion MCS. Use of the split construct system would reduce the non-specific background of our screen because the proximity labeling enzymes should only be functional upon reconstitution at ER-inclusion MCS. Additionally, because only a portion of the proximity labeling enzyme is being fused to the Inc protein, this may improve the ability of the fusion protein to be expressed by *Chlamydia* and remain functional.

An alternative approach to proximity labeling

As an alternative approach to proximity labeling, Spatially Targeted Optical Micro Proteomics (STOMP) could be used to identify additional effectors at ER-inclusion MCS (237). In STOMP, regions of interest are labeled for identification by immuno-florescence microscopy and the images are then used to generate "MAP" files of the region of interest. The "MAP" files can then be used to guide two-photon laser driven cross-linking of a photoreactive affinity tag at the region of interest. Affinity purification and mass spectrometry can then be utilized to isolate and identify proteins within the region of interest (237). Recently, an automated STOMP technique (autoSTOMP) has been developed that 1) coordinates the image capture and cross-linking functions and 2) utilizes a commercially available biotin-benzophenone photo-cross-linker to make the

STOMP protocol more accessible and user friendly (238). While the spatial resolution of STOMP (~ 0.6-1μm) is not as high as proximity labeling techniques such as BioID and APEX (~10nm), it is beneficial in that it does not require genetic manipulation to express a fusion protein that must then be accurately targeted to a specific region of interest. In order to identify components at ER-inclusion MCS, STOMP could be performed on cells infected with an IncV overexpressing strain of *C. trachomatis*. As with proximity labeling approaches, recruitment of candidate host factors to ER-inclusion MCS would need to be validated and assessed for co-localization with known ER-inclusion MCS. STOMP could also aid in determining the mechanism of host glycolytic enzyme localization to the inclusion by comparing proteins identified by STOMP at the 60% inclusions that exhibit glycolytic enzyme localization versus the 40% of inclusions that do not (Figure 3.2 C). Proteins enriched at inclusions exhibiting glycolytic enzyme localization could then be overexpressed or disrupted, and the effects on host glycolytic localization to the inclusion assessed by confocal microscopy.

Analyses to identify potential candidate effectors

Even with increasing the specificity of the proximity labeling screen or utilizing STOMP, non-specific background is likely to still be an issue, thus the analysis of the identified proteins will also need to be optimized. The Significance Analysis of INTeractome (SAINT) software package takes quantitative proteomics data and generates confidence scores for putative interactions, which aids in removing non-specific interactions in an un-biased manner (239). Similar proximity labeling studies have utilized SAINT in order to assign significance to the identified proteins, and this same analysis could be applied to

proteins identified in our screen (174). Additionally, we could directly compare the results of our screen against proteins identified in similar proximity labeling screens. Identifying proteins that were also found in similar proximity labeling screens would increase our confidence in the candidate proteins being present at the inclusion membrane. However, as these previous proximity labeling screens have sought to label the inclusion membrane in general, this comparison would not necessarily aid in the specific identification of ER-inclusion MCS components. If we were able identify proteins that were common to all of the screens, but specifically enriched in our screen, this could indicate ER-inclusion MCS specificity. However, as highlighted by Olson et al., differences in experimental procedure and data analysis methods between these studies can make direct comparison difficult (240).

Prioritizing potential candidate effectors

Proximity labeling screens can often result in the identification of hundreds to thousands of potential candidate proteins, therefore, prioritizing candidate proteins for further validation and characterization is an important consideration. Based on our finding that host glycolytic enzymes localize to the inclusion membrane, it would be interesting to see if host glycolytic enzymes continue to be identified in the screen, and would provide insight on whether the host glycolytic enzymes localize to ER-Inclusion MCS specifically or the inclusion membrane in general. Given that additional host kinases are likely involved in the phosphorylation of IncV, host kinases identified in the screen would also be of interest as potential additional kinases that phosphorylate IncV, especially those that were also previously predicted to interact with IncV in the Inc-

Human interactome (198). In addition to kinases, I would be particularly interested in identifying phosphatases that could de-phosphorylate IncV and provide additional insight into the regulation of the IncV-VAP tethering interaction and ER-inclusion MCS formation and maintenance. Due their localization at the inclusion membrane and known ability to interaction with host cell molecules and organelles, any *Chlamydia* Inc proteins would also be of interest, not only as potential ER-inclusion MCS components, but also as potential bacterial factors facilitating the localization host glycolytic enzymes to the inclusion. Additionally, as several host factors known to function at a variety of cellular MCS have been identified as components of ER-inclusion MCS, any host cell factors that are known components of cellular membrane contact sites would also be of interest. Oxysterol binding protein (OSBP) and extended synaptotagmins (E-syts) proteins that serve as both tethers and lipid transfer proteins at ER-Golgi and ER-plasma membrane contact sites respectively, are representative of such host proteins (206). Future studies could utilize confocal microscopy to verify recruitment of the identified host and bacterial candidates to the inclusion membrane and co-localization with known ER-inclusion MCS. To determine if the identified host or bacterial factors play a role in *C. trachomatis* intracellular development, inclusion size and infection progeny production could be measured following infection with *C. trachomatis* mutant strains or host gene silencing by siRNA duplexes.

The role of host glycolytic enzyme inclusion localization

We have shown that several host glycolytic enzymes are recruited to the inclusion membrane (Figure 3.2) and that at least one host glycolytic enzyme, Aldolase A, is

important for *Chlamydia* development (Figure 3.10). However, the specific role that these enzymes are playing at the inclusion membrane is not fully understood.

The presence of the host glycolytic enzymes at the inclusion could simply be generating a local pool of ATP that can then be used by the bacteria. Alternately, rather than direct ATP production, the host glycolytic enzymes could be generating glycolytic intermediates that can be utilized by the bacteria. For example, the glycolytic intermediate glucose-6-phoshate is known to be imported by the bacteria and is largely used for cell-wall biosynthesis (42). The glycolytic pathway also directly feeds into other metabolic pathways, such as the pentose phosphate pathway and the TCA cycle (Figure 1.1). Thus, another possibility is that an increase in glycolysis at the inclusion membrane is leading to a local upregulation of the pentose phosphate pathway and/or TCA cycle to provide the bacteria with host nucleotides or TCA cycle intermediates respectively.

An important consideration regarding the role of the host glycolytic enzymes at the inclusion is how glycolytic intermediates or other host metabolites are entering the inclusion to be available for use by the bacteria. The permeability of the inclusion membrane is not well understood. Originally, the inclusion was shown to be impermeable to low-molecular weight compounds greater that 520 Da (201). However, additional studies have demonstrated that the inclusion membrane is permeable to ions, indicating that host metabolites such as glycolytic substrates, which are smaller than 520 Da, may be able to enter the inclusion (202). However, further experiments are required to validate that these metabolites can passively enter the inclusion. Validating that host metabolites can enter the inclusion would require florescent analogs that could distinguish the presence of glycolytic intermediates in the host cell cytosol versus the inclusion. It is also

possible that the localization of host glycolytic enzymes does not serve to generate metabolites that enter the inclusion, but rather to provide ATP for kinase phosphorylation or lipid/ion exchange reactions at the inclusion surface that mediate interaction with the host cell.

All of the aforementioned roles for localization of host glycolytic enzymes to the inclusion rely on the assumption that the enzymes are functional and participating actively in glycolysis. However, it is also possible, albeit less likely, that the inclusion is sequestering host glycolytic enzymes and/or reducing their activity. A recent study with Hepatitis B Virus (HBV) found that large viral surface antigens of HBV bind to host PKM2 and reduce its enzymatic activity, which shifts the host cell to aerobic glycolysis (241). A similar shift to aerobic glycolysis has been observed upon *C. trachomatis* infection (53), thus it is intriguing to think about the possibility that *C. trachomatis* is able to help shift the cell to aerobic glycolysis, in part by sequestering and reducing the activity of PKM2. If this were the case, treatment with activators of PKM2 (242) might be expected to negatively affect *C. trachomatis* growth and development. However, since only the pool of PKM2 localized to the inclusion would be affected, *C. trachomatis* may not be able to inhibit enough PKM2 to shift the cell to aerobic glycolysis.

Although we showed that depletion of host AldoA negatively affects *C. trachomatis* development (Figure 3.10), additional studies are needed to determine if depletion of PKM2, LDHA, or other host glycolytic enzymes have similar effects on *C. trachomatis* development. If siRNA knockdown of PKM2 or LDHA also resulted in decrease inclusion size or infectious progeny production, then that would indicate that

host glycolytic enzymes in general, not just Aldolase A specifically, play a role in C. trachomatis intracellular growth.

The role of bacterial glycolytic enzymes in *C. trachomatis* development

The *C. trachomatis* glycolytic enzymes were shown to be functional by heterologous expression in *E. coli* (45), however saturated EMS mutagenesis was able to generate a nonsense mutation in the enzyme responsible for shuttling glucose-6-phosphate into the glycolytic pathway, glucose-6-phosphate isomerase (*pgi*). This led to the hypothesis that the glycolytic pathway is expendable for *C. trachomatis* (46). It is possible, however, that the production of fructose-6-phosphate through the pentose phosphatase pathway could compensate for glucose-6-phosphate isomerase activity. Since saturated EMS mutagenesis did not generate nonsense mutations in any of the other *C. trachomatis* glycolytic enzymes (46), the glycolytic pathway may actually be essential for *C. trachomatis* development. To determine the essentiality and function of these glycolytic enzymes, future studies could attempt to generate bacterial glycolytic mutant strains of *C. trachomatis*. Based on our findings that bacterial glycolytic enzyme expression is downregulated throughout development (Figure 3.11), I hypothesize that the *C. trachomatis* glycolytic enzymes are only essential, or play a role, in early intracellular development. The bacterial glycolytic enzymes could allow for the bacteria to begin the developmental cycle and synthesize/recruit factors necessary for host glycolytic enzyme localization to the inclusion, after which the bacterial glycolytic enzymes are no longer strictly necessary.

The ability to generate glycolytic mutant strains would indicate that the bacterial glycolytic enzymes are not essential. Inclusion size and infectious progeny assays could then be performed to determine if these glycolytic enzymes play a role in *C. trachomatis* intracellular growth and development.

Given that we observed increased localization of host glycolytic enzymes to the inclusion over the course of infection and a corresponding decrease in bacterial glycolytic enzyme expression (Figure 3.5A and 3.11), I also hypothesize that host glycolytic enzymes are able to compensate, at least in part, for a lack of bacterial glycolysis. To begin to address this hypothesis, cells with or without siRNA knockdown of host glycolytic enzymes could be infected with bacterial glycolytic mutant strains of *C. trachomatis* and assayed for inclusion size and infectious progeny production. If the host glycolytic enzymes can compensate for decreased bacterial glycolysis, one would expect that knockdown of the host glycolytic enzymes would result in decreased inclusion size and/or bacterial progeny production for glycolytic mutant strains of *C. trachomatis*.

Connecting ER-Inclusion MCS and host glycolytic enzyme inclusion localization

The host glycolytic enzymes were identified in a preliminary proximity labeling screen to identify effectors at ER-inclusion MCS; however, the host glycolytic enzymes appeared evenly distributed over the inclusion membrane rather than in distinct patches as observed for other host factors present at ER-Inclusion MCS (Figure 3.2). Therefore, it is unclear whether the host glycolytic enzymes localize to the inclusion membrane in general or if they are playing a specific role at ER-inclusion MCS. Although the glycolytic enzyme localization at the inclusion is not patchy in appearance, this could be

due to overexpression of the glycolytic enzymes. To determine the inclusion localization of host glycolytic enzymes at endogenous levels, antibodies against the host glycolytic enzymes could be used to visualize endogenous recruitment by confocal microscopy. Preliminary studies with an antibody against Aldolase A were un-successful, thus additional optimization experiments and antibodies would be needed.

If localized to ER-inclusion MCS, it is possible that the glycolytic enzymes could be providing ATP for reactions happening at ER-inclusion MCS. Glycolytic enzymes have been shown to localize to membranes where ATP is being consumed rapidly, such as the membrane of human red blood cells (243). Reactions meditating host-inclusion interaction at ER-inclusion MCS could result in a local depletion of ATP and lead to an ER-inclusion MCS localization of the host glycolytic enzymes.

Another possibility is that the glycolytic enzymes are forming multi-enzyme complexes that are playing a role in maintaining the ER and inclusion in close proximity. In fact, the formation of multi-glycolytic enzyme complexes has been shown to play a role in mitochondria-chloroplast interactions in *Arabidopsis* (244). This possibility could be supported by the fact that we observed the localization of multiple host glycolytic enzymes to the same inclusion (Figure 3.3). To explore a potential role for the host glycolytic enzyme complexes as tethers at ER-inclusion MCS, future studies could perform correlative fluorescence and electron microscopy (CFEM) and compare the amount of ER associated with the inclusion membrane for inclusions that exhibit host glycolytic enzyme recruitment versus those that do not. If the host glycolytic enzymes are contributing to ER-inclusion MCS formation and maintenance, then inclusions exhibiting

host glycolytic enzyme recruitment would be expected to have higher levels of ER association.

Eukaryotic mimicry by intracellular pathogens

Our work has identified several ways in which *C. trachomatis* may be mimicking eukaryotic motifs. Previous work from our lab identified two motifs in IncV that mimicked eukaryotic FFAT motif cores to facilitate interaction with VAP (68). Recently, a new class of FFAT motifs referred to as phospho-FFAT motifs, in which the acidic residue in position 4 is replaced by a phosphorylatable residue, have been described (158). My data now indicate that one of the IncV FFAT motifs could acts as a phospho-FFAT motif, effectively mimicking eukaryotic phospho-FFAT containing proteins such as STARD3 (Figure 4.15). Moreover, *C. trachomatis* may also be mimicking the phosphorylation of residues within the FFAT motif acidic tract. We showed that phosphorylation of the IncV acidic tracts is key for the IncV-VAP interaction (Figure 4.19B and C) and recent studies have shown that eukaryotic FFAT motif containing proteins also utilize phosphorylation of residues upstream of the FFAT motif core to facilitate interaction with VAP at cellular membrane contact sites (225, 226).

Additionally, we identified CK2 as a host kinase responsible for phosphorylating IncV to mediate the IncV-VAP interaction and thus the formation of ER-inclusion MCS (Figure 4.4). CK2 also plays diverse roles for other intracellular pathogens. In fact, several viruses rely on CK2 phosphorylation for a variety of functions. The Vaccinia virus requires CK2 for both actin tail formation and cell-to-cell spread (245). For Human Cytomegalovirus, Bluetongue virus, and certain Human Papillomavirus subtypes, CK2

plays important roles in regulating viral replication (246-248). CK2 also plays a role in Hepatitis C virus (HCV) infection by phosphorylating the HCV NS2 protein and targeting it for proteasome degradation (249). In addition to these viral examples, phospho-regulation of the *Listeria* protein ActA by CK2 mimics the CK2-mediated affinity of the host WASP/WAVE family of proteins for the ARP2/3 complex (250-252). It is likely that *C. trachomatis* has co-opted the ability of CK2 to regulate protein interaction.

Our findings may provide insight into how other intracellular pathogens are displaying eukaryotic mimicry. The norovirus NS1/2 protein interacts with VAP through what would now be characterized as a putative phospho-FFAT motif (215). Interestingly, both the threonine residue in position 4 of the NS1/2 FFAT motif core and a serine reside in the upstream acidic tract are part of CK2 recognition motifs, indicating that these residues could be directly phosphorylated by CK2. It would be interesting to determine if, similarly to what we overserved with IncV, CK2 phosphorylates the NS1/2 protein in order to promote the NS1/2-VAP interaction. Since the NS1/2 FFAT motif was shown to be required for the NS1/2-VAP interaction and proper viral replication (215), this could suggest an important role for CK2 in the norovirus lifecycle.

CK2 as a regulator of cellular MCS

We have shown that phosphorylation of IncV by CK2 mediates the IncV-VAP interaction and tethering at ER-inclusion MCS. Since pathogens often co-opt cellular processes, the regulatory role of CK2 at ER-inclusion MCS could indicate that CK2 is a regulator at cellular MCS. Similar to what we observe with IncV, CK2 could phosphorylate serine or

threonine residues upstream of FFAT motifs in other FFAT motif containing proteins and facilitate binding to VAP family proteins and the formation of cellular MCS.

Additionally, CK2 has also been shown to have a putative HIKE domain which interacts with PH domain containing proteins (253) and this putative HIKE domain plays a role in the interaction of CK2 with CKIP-1 at the plasma membrane (254). As many cellular MCS include PH domain containing proteins, especially ER-MCS, it would be interesting to determine if CK2 associates with PH domain containing proteins at MCS. Our lab has shown that the Inc protein IncD interacts with CERT, a PH domain containing protein at ER-Inclusion MCS (74, 159). The interaction of CK2 with CERT could be tested using an IncD overexpressing strain of *C. trachomatis* to increase CERT recruitment to the inclusion and determine if CK2 is recruited to the inclusion in a CERT dependent manner. If CK2 is able to bind to CERT, it is also possible that CK2 phosphorylates CERT. It has been previously shown that phosphorylation of CERT by other host kinases can alter its confirmation and lipid transfer activity (255), thus CK2 could also potentially contribute to the phospho-regulation of CERT lipid transfer activity. Overall, the putative HIKE domain of CK2 could provide a mechanism by which CK2 is recruited to PH-domain containing proteins at cellular MCS and regulates the activity of the proteins via phosphorylation.

Modulating interactions of the *C. trachomatis* inclusion with VAP-family proteins

The large number of VAP interactors likely results in competition between FFAT-motif containing proteins for binding to VAP-family proteins. As an intracellular pathogen, *C. trachomatis* must ensure that it is able to effectively compete with other host FFAT-motif

containing proteins to bind VAP. The phosphorylation of residues upstream of the core

FFAT motifs and the presence of multiple FFAT motifs in IncV may be mechanisms by

which *C. trachomatis* modulates IncV-VAP binding and downstream ER-inclusion MCS

formation and maintenance.

Phosphorylation of residues upstream of FFAT motifs

Previous studies have suggested that phosphorylation of residues within the acidic tracts

of FFAT motifs can play a role in modulating VAP interactions (140, 225, 226). This is

thought to happen through the negative charge of phosphate groups increasing affinity for

the electropositive face of the VAP-MSP domain. We showed that phosphorylation of the

serine tracts directly upstream of the IncV FFAT motifs are key for the IncV-VAP

interaction (Figure 4.19B and C). One could imagine that the number of phosphorylated

residues upstream of the FFAT motifs could modulate the strength of the IncV-VAP

interaction, with an increase in phosphorylated residues resulting in an enhanced IncV-

VAP binding. The phosphorylation of multiple residues is supported by the large shift in

molecular weight that we observed for IncV (Figure 4.1A). To determine if the number of

phosphorylated serine tract residues plays a role in IncV-VAP interaction, IncV

constructs with varying number of serine tract residues mutated to alanine could be

purified from *E. coli* and assayed for VAP binding *in vitro* as described in Chapter 4.

This hypothesis could be also be tested in the context of infection by infecting cells

expressing YFP-VAP with *C. trachomatis* strains expressing the corresponding IncV

mutants and assessing VAP recruitment to the inclusion. Our current data looked at the

effects of mutating the entirety of the serine tracts upstream of the FFAT motifs,

however, it is possible that only a portion of the serine tract residues are being phosphorylated at any given time. In order to definitively determine the phosphorylation state of the serine tracts of IncV, phosphoproteomic techniques such as post-translational modification mass spectrometry would need to be optimized and performed on IncV purified from infected host cells.

Although the residues upstream of the IncV FFAT motifs are almost all serine residues, it is important to note that each of the serine tracts have acidic residues (Figure 5.1). It is not yet known the extent to which these acidic residues play a role in mediating the IncV-VAP interaction, however they may be playing a substantial role given that acidic tracts for several FFAT containing proteins contain similar numbers of acidic residues (Figure 5.1). In order to determine if these acidic residues play a role in the IncV-VAP interaction, future studies could make *C. trachomatis* strains expressing IncV with single and combination alanine mutations of these acidic residues and assess VAP recruitment via confocal microscopy. Transmission electron microscopy could then be used to assess the role of these acidic residues in ER-inclusion MCS formation.

Interaction with multiple VAP-family proteins

IncV possesses two FFAT motifs, a canonical FFAT motif and a non-canonical FFAT motif that may be acting as a phospho-FFAT motif (Figure 5.1). Similarly, the mitochondrial membrane protein PTPIP51 also possess two FFAT motifs, one of which is likely a phospho-FFAT motif, and has been shown to interact with all known VAP and MOSPD proteins (152, 153). It is possible that the presence of multiple and/or varied FFAT motifs allows for interaction with multiple VAP family proteins. VAP family

proteins can form segregated protein complexes with VAPA, VAPB and MOSPD2 interacting with one another and MOSPD1 and MOSPD3 interacting to form a separate complex (Neefjes and cabukusta, 2021). If the two FFAT motifs of IncV allow for interaction of IncV with multiple VAP family proteins, it could help to ensure that IncV forms multiple distinct interactions with the ER to facilitate ER-inclusion MCS formation.

IncV has previously been shown to interact with both VAPA and VAPB (68), thus, it would be interesting to determine of IncV is also able to interact with MOSPD proteins to facilitate ER-inclusion MCS formation/maintenance. To determine if IncV interacts with MOSPD proteins, cells expressing florescent versions of the MOSPD proteins could be infected with an IncV overexpressing strain of *C. trachomatis* and the recruitment of MOSPD proteins to the inclusion assess by confocal microscopy. To determine if MOSPD proteins contribute to the formation and/or maintenance of ER-inclusion MCS, transmission electron microscopy could be used to assess the amount of ER associated with the inclusion following siRNA knockdown of each of the MOSPD proteins. If MOSPD proteins are contributing to ER-inclusion MCS, one would expect that knockdown of the MOSPD proteins would result in decreased ER association with the inclusion.

Figure 5.1 Phosphorylatable serine residues upstream of the IncV FFAT motifs cores mimic acidic tracts upstream of eukaryotic FFAT motif cores. Alignment of several proteins with reported FFAT and/or Phospho-FFAT (P-FFAT) motifs including *C. trachomatis* IncV. The FFAT motif core is indicated with a grey box. Whether the motif is considered to be a FFAT or P-FFAT motif is indicated with an asterisk on the right. The essential position 2 of the core motif is indicated in blue. Acidic residues are indicated with red and phosphorylatable serine/threonine residues are indicated in orange.

Phosphorylation and the dynamic regulation of ER-inclusion MCS

We have shown that phosphorylation of IncV is necessary to promote the IncV-VAP

tethering interaction at ER-inclusion MCS (Figure 4.3). However, it is unclear whether

phosphorylation of IncV simply strengthens FFAT motif interactions with VAP, or

whether phosphorylation of IncV allows for dynamic regulation of ER-inclusion MCS

formation and disassembly. It is possible that ER association with the inclusion is closely

regulated to prevent excessive interaction with the ER and allow for the inclusion to

interact with other host organelles throughout the developmental cycle. Another

possibility is that a proportion of IncV is kept in an unphosphorylated state to enable

interaction of IncV with other factors, this is supported by IncV having the largest

number of predicted interacting proteins in an Inc-human interactome (198). To

determine if ER-inclusion MCS formation is indeed being regulated by the

phosphorylation of IncV, we must first fully understand how phosphorylation promotes

the IncV-VAP interaction as well as any kinases and phosphatases involved in regulating

the phosphorylation status of IncV.

IncV conformational change upon phosphorylation by CK2

Recruitment of CK2 to the inclusion by C-terminal serine residues of IncV was necessary

for VAP recruitment to the inclusion, but phosphomimetic mutation of these serine

residues alone was not sufficient to promote VAP binding *in vitro* (Figure 4.14).

However, phosphomimetic mutation of the IncV serine tracts was sufficient to promote

VAP binding *in vitro* (Figure 4.19D). Phosphorylation is known to play a role in altering

protein conformation (256), thus one could imagine that the phosphorylation of the three

C-terminal serine residues by CK2 could alter the confirmation of IncV such that the FFAT motifs and the upstream serine tracts are now accessible and able to be phosphorylated by CK2 and other host kinases to facilitate the IncV-VAP interaction. This hypothesis is supported by the S3A mutant version of IncV, that is deficient in CK2 recruitment (Figure 4.10B and C), appearing unphosphorylated (Figure 4.10F). However, it is important to note that mass spectrometry is still necessary to confirm to phosphorylation state of the IncV S3A mutant. To assess whether phosphorylation of the C-terminal serine residues by CK2 results in a conformational change of IncV, mass spectrometry data could be coupled with protein conformation analyses such as Nuclear magnetic resonance (NMR) spectroscopy. The development of solution and solid-state NMR techniques has improved the use of NMR for the structural determination of membrane proteins, however size limitations and sparse data accumulation pose technical challenges for this approach. Ideally, future studies would be able to perform X-ray crystallography to solve the structure of IncV bound to CK2. However, obtaining high resolution crystals of membrane proteins is notoriously difficult due to the need for large amounts of purified protein and difficulties in extracting transmembrane proteins from the membrane.

Additional kinases phosphorylating IncV

Although we have shown that the host kinase CK2 directly phosphorylates IncV (Figure 4.1D), our data are consistent with additional host kinases being necessary to 1) phosphorylate the serine tracts upstream of the FFAT motifs, as prior priming by other kinase(s) would be necessary for CK2 phosphorylation of these regions, and 2)

phosphorylate T_{265} in the IncV non-canonical FFAT, as it is not part of a CK2 recognition

motif. In addition to CK2, the Inc-human interactome predicted nine other kinases to

interact with IncV (Casein Kinase Iα, Casein Kinase Iε, Phosphatidylinositol-5-Phosphate

4-Kinase Type 2α, Phosphatidylinositol-5-Phosphate 4-Kinase Type 2β,

Phosphatidylinositol-5-Phosphate 4-Kinase Type 2γ, Serine/threonine-protein kinase

VRK2, Serine/threonine-protein kinase TAO2, Mitogen-activated protein kinase kinase

kinase kinase 4, and Focal adhesion kinase 1) (198). These nine kinases would be

excellent candidates to test for potential phosphorylation of IncV. Additionally, several

host kinases that have been shown to phosphorylate and regulate interactions at cellular

membrane contact sites would also be good candidates. These kinases include casein

kinase I and Ca^{2+}/calmodulin-dependent protein kinase II that phosphorylate Miga at ER-

mitochondria MCS, and Glycogen synthase kinase 3 beta that phosphorylates ACBD5 at

ER-peroxisome MCS and PTPI51 at ER-mitochondria MCS (208, 226, 257). Lastly,

several kinases have been previously shown to localize to the inclusion membrane,

namely Active Src family kinases, Myosin light-chain kinase, and Protein Kinase C, and

would also serve as potential candidates (70, 94, 258). Further analysis of IncV by the

online program GPS (http://gps.biocuckoo.cn/) (259), indicates that Casein Kinase I,

Serine/threonine-protein kinase VRK2, Ca^{2+}/calmodulin-dependent protein kinase II, and

Protein Kinase C and have potential phosphorylation sites in the IncV serine tracts,

making these kinases of particular interest for future studies.

To test the involvement of these kinases in phosphorylating IncV, cells expressing

fluorescent versions of the kinases could be infected with an IncV overexpressing strain

of *C. trachomatis* and use confocal microscopy to determine if overexpression of IncV

facilitates kinase recruitment to the inclusion. The recruitment of the kinases to the inclusion membrane upon IncV overexpression should also be validated by staining with endogenous antibodies for the kinases. *In vitro* kinase assays could then be used to assess the phosphorylation state of IncV following incubation with the identified kinases alone or in combination with CK2 to determine any cooperative effects of the kinases. To determine if these kinases contribute to the formation and/or maintenance of ER-inclusion MCS, transmission electron microscopy could be used to assess the amount of ER associated with the inclusion following siRNA knockdown, chemical inhibition, or CRISPR/Cas knockout (if feasible) of each of the kinases.

Phosphatases in the regulation of IncV phosphorylation

In addition to kinases, host cell phosphatases could play a significant role in regulating ER-inclusion membrane contact site formation. It is possible that residues phosphorylated by CK2 and other host kinases to promote the IncV-VAP interaction are reciprocally de-phosphorylated by host phosphatases to promote disassembly of the IncV-VAP tethering interaction. Phosphoprotein phosphatases (PPPs) are responsible for more than two thirds of the phosphatase activity in eukaryotic cells, making them interesting candidates (260). One of these PPPs, Protein phosphatase 4 (PP4) has recently been shown to recognize FxxP consensus binding motifs (261). Interestingly, the core of the IncV non-canonical FFAT motif contains an FxxP motif, thus it may be worth determining if PP4 plays a role in de-phosphorylating T_{265} in the non-canonical FFAT motif or upstream serine tract residues to regulate the IncV-VAP interaction and ER-inclusion MCS formation.

To determine if PP4 binds to IncV, co-immunoprecipitation could be performed on samples purified from cells co-expressing a tagged version of the PP4 regulatory subunit PPP4R3 and either wildtype IncV or a mutant version of IncV with the FxxP motif mutated to AxxA. To further determine if PP4 regulates the phosphorylation status of IncV, wildtype and AxxA mutant versions of IncV could be analyzed by Phos-tag or regular SDS-PAGE to determine the effect of mutating the PP4 binding site on the shift in molecular weight of IncV. Quantitative mass spectrometry could also be used to identify phosphorylation sites in IncV that are increased when the PP4 binding site is mutated. Because an AxxA mutant of IncV will result in the mutation of the essential F residue in position two of the non-canonical FFAT motif, it will be difficult to determine if PP4 directly plays a role in the IncV-VAP interaction and ER-inclusion MCS formation. We could try to knockdown or overexpress PP4 and use immunofluorescence and transmission electron microscopy to determine effects on VAP recruitment to the inclusion and ER association with the inclusion respectively. However, both of these options could be difficult as knockdown of PP4 will likely result in negative effects on the host cell and proper overexpression of PP4 may require the overexpression of multiple PP4 subunits.

Additionally, protein phosphatase 1 (PP1) and CK2 have been shown to target the same phosphosites to regulate the function of the DNA-binding protein Ikaros (262, 263). Moreover, PP1 and CK2 have also been implicated in regulating calmodulin phosphorylation at M-type potassium channels (264). Even though the C-terminus of IncV does not contain a typical PP1 binding motif (RVxF), due to the previous examples of reciprocal regulation by PP1 and CK2, it would be interesting to determine if PP1

plays a role in the phosphorylation state of IncV and corresponding ER-inclusion MCS formation. A role for PP1 in modulating the IncV-VAP interaction and ER-inclusion MCS could be determined similarly to what is described above for PP4, but would require the knowledge of where PP1 might bind to IncV.

Regulation of Type III translocation

While mutation of the IncV serine tracts to non-phosphorylatable alanine residues did not inhibit proper translocation of IncV (Figure 4.19B), mutation of the IncV serine tracts to phosphomimetic aspartic acid residues interfered with IncV translocation and the protein remain trapped within the bacteria (Figure 4.19E). However, the mechanism by which IncV translocation is being prevented is not yet understood. One hypothesis is that the aspartic acid residues are leading to an increase in negative charge that is blocking translocation through the T3SS machinery and IncV is becoming trapped in the T3SS. To test this hypothesis, cells infected with an IncV phosphomimetic serine tract mutant strain of *C. trachomatis* could be stained with antibodies against a bacterial effector expressed late in the developmental cycle following IncV induction. Confocal microscopy could then be used to determine if overexpression of this IncV mutant blocks the T3SS machinery and prevents the proper translocation/secretion of other bacterial effectors. Another hypothesis is that the aspartic acidic residues interfere with the proper folding/unfolding of IncV and that IncV is not able to be unfolded to be translocated through the T3SS machinery. To test this hypothesis, circular dichroism could be used to determine the protein folding state of this mutant version of IncV compared to WT. If phosphomimic mutation of the serine tracts is preventing IncV from being unfolded prior

to translocation, I would expect this mutant form of IncV to only be found in the folded conformation. Our data support the idea that *C. trachomatis* IncV has evolved to have a serine tract that can be phosphorylated by a host kinase to ensure proper translocation. It would be interesting to look at other *C. trachomatis* Inc proteins and effectors and determine if they also lack acidic residues or have regions highly enriched in phosphorylatable residues to determine if this is a mechanism commonly used by *C. trachomatis* or even other intracellular pathogens to ensure proper type III translocation/secretion.

Therapeutic potential

We showed that host glycolytic enzymes are recruited to the inclusion membrane and play a role in *C. trachomatis* development. Due to their importance to host cell metabolism and survival, the host glycolytic enzymes are not ideal therapeutic targets. However, the development of glycolytic enzyme inhibitors is a growing interest in the cancer biology field (265), due to the strong connection of increased glycolysis in cancer cells. It is possible that these glycolytic enzyme inhibitors could be used to treat *Chlamydia* infections. Additionally, as we gain a better understanding of the role that the bacterial glycolytic enzymes are playing in *C. trachomatis* development, the bacterial glycolytic enzymes may emerge as potential therapeutic targets. Further studies are needed to determine if the bacterial glycolytic enzymes can be effectively inhibited without also effecting the host glycolytic enzymes.

IncV has been shown to form a tethering interaction with ER resident protein VAP and promote the formation of ER-inclusion MCS (68). These ER-inclusion MCS

are proposed have a role in the non-vesicular trafficking of host lipids to the inclusion membrane, a process that is proposed to be essential for proper chlamydial growth, making IncV an interesting therapeutic target. However, an IncV mutant strain of *C. trachomatis* does not abolish ER-inclusion MCS formation (68). This is not unsurprising given the large amount of tether redundancy at membrane contact sites and the fact that another Inc protein, IncD, is also known to interact with VAP (via CERT) and could also help to facilitate membrane tethering in addition to its proposed functional role (159). Thus, IncV by itself may not be a good therapeutic target, but could be targeted in combination with other factors to fully disrupt ER-inclusion MCS formation. It would be particularly interesting to look at the effects of an IncV/IncD double mutant on ER-inclusion MCS formation.

Overall conclusions and significance

Overall, my thesis work has identified mechanisms by which *Chlamydia* establishes and maintains an intracellular niche. I have shown that host glycolytic enzymes localize to the *Chlamydia* inclusion and play a role in intracellular replication and development. Additionally, my work has identified the host kinase CK2 as an important regulator of the IncV-VAP tethering interaction at ER-inclusion MCS. While much work remains to be done, my work provides insight into how *C. trachomatis* manipulates host cell metabolism and uncovers potential interplay between host and bacterial glycolysis. My work also provides several insights into the general biology of MCS, which are becoming increasingly recognized for their importance in cellular processes and disease (206). Identification of CK2 as a regulator at ER-inclusion MCS could provide a potential

mechanism of regulation at other MCS throughout the cell. In addition, my work also suggests that phosphorylatable residues can substitute for acidic tracts in FFAT motifs. If this was added to current FFAT motif identification algorithms, it could allow for the identification of previously unrecognized FFAT motif-containing proteins. Together with additional future research, my work could lead to the development of new therapeutics for treatment or prevention of *Chlamydia* infection.

References

1. Cheong HC, Lee CYQ, Cheok YY, Tan GMY, Looi CY, Wong WF. 2019. Chlamydiaceae: Diseases in Primary Hosts and Zoonosis. Microorganisms 7.

2. Skelding KA, Hickey DK, Horvat JC, Bao S, Roberts KG, Finnie JM, Hansbro PM, Beagley KW. 2006. Comparison of intranasal and transcutaneous immunization for induction of protective immunity against *Chlamydia muridarum* respiratory tract infection. Vaccine 24:355-66.

3. Patel M, Lin SA, Boddicker MA, DeMaula C, Connolly B, Bednar B, Heinrichs JH, Smith JG. 2015. Quantitative In Vivo Detection of *Chlamydia muridarum* Associated Inflammation in a Mouse Model Using Optical Imaging. Mediators Inflamm 2015:264897.

4. Joseph SJ, Marti H, Didelot X, Castillo-Ramirez S, Read TD, Dean D. 2015. Chlamydiaceae Genomics Reveals Interspecies Admixture and the Recent Evolution of *Chlamydia abortus* Infecting Lower Mammalian Species and Humans. Genome Biol Evol 7:3070-84.

5. Burillo A, Bouza E. 2010. Chlamydophila pneumoniae. Infect Dis Clin North Am 24:61-71.

6. Gautam J, Krawiec C. 2022. *Chlamydia* Pneumonia, StatPearls, Treasure Island (FL).

7. Harkinezhad T, Verminnen K, De Buyzere M, Rietzschel E, Bekaert S, Vanrompay D. 2009. Prevalence of *Chlamydophila psittaci* infections in a human

population in contact with domestic and companion birds. J Med Microbiol 58:1207-1212.

8.   Longbottom D, Coulter LJ. 2003. Animal chlamydioses and zoonotic implications. J Comp Pathol 128:217-44.

9.   Pichon N, Guindre L, Laroucau K, Cantaloube M, Nallatamby A, Parreau S. 2020. *Chlamydia abortus* in Pregnant Woman with Acute Respiratory Distress Syndrome. Emerg Infect Dis 26:628-629.

10.   Mishori R, McClaskey EL, WinklerPrins VJ. 2012. *Chlamydia trachomatis* infections: screening, diagnosis, and management. Am Fam Physician 86:1127-32.

11.   Malhotra M, Sood S, Mukherjee A, Muralidhar S, Bala M. 2013. Genital *Chlamydia trachomatis*: an update. Indian J Med Res 138:303-16.

12.   Elwell C, Mirrashidi K, Engel J. 2016. *Chlamydia* cell biology and pathogenesis. Nat Rev Microbiol 14:385-400.

13.   Wright HR, Turner A, Taylor HR. 2008. Trachoma. Lancet 371:1945-54.

14.   Stoner BP, Cohen SE. 2015. Lymphogranuloma Venereum 2015: Clinical Presentation, Diagnosis, and Treatment. Clin Infect Dis 61 Suppl 8:S865-73.

15.   Rawla P, Thandra KC, Limaiem F. 2022. Lymphogranuloma Venereum, StatPearls, Treasure Island (FL).

16.   Taylor BD, Haggerty CL. 2011. Management of *Chlamydia trachomatis* genital tract infection: screening and treatment challenges. Infect Drug Resist 4:19-29.

17. Workowski KA, Bachmann LH, Chan PA, Johnston CM, Muzny CA, Park I, Reno H, Zenilman JM, Bolan GA. 2021. Sexually Transmitted Infections Treatment Guidelines, 2021. MMWR Recomm Rep 70:1-187.

18. Sutton TL, Martinko T, Hale S, Fairchok MP. 2003. Prevalence and high rate of asymptomatic infection of *Chlamydia trachomatis* in male college Reserve Officer Training Corps cadets. Sex Transm Dis 30:901-4.

19. Peipert JF. 2003. Clinical practice. Genital chlamydial infections. N Engl J Med 349:2424-30.

20. de la Maza LM, Darville TL, Pal S. 2021. *Chlamydia trachomatis* vaccines for genital infections: where are we and how far is there to go? Expert Rev Vaccines 20:421-435.

21. Poston TB, Gottlieb SL, Darville T. 2019. Status of vaccine research and development of vaccines for *Chlamydia trachomatis* infection. Vaccine 37:7289-7294.

22. Stamm WE. 1999. *Chlamydia trachomatis* infections: progress and problems. J Infect Dis 179 Suppl 2:S380-3.

23. Darville T, Hiltke TJ. 2010. Pathogenesis of genital tract disease due to *Chlamydia trachomatis*. J Infect Dis 201 Suppl 2:S114-25.

24. Wynn A, Mussa A, Ryan R, Hansman E, Simon S, Bame B, Moreri-Ntshabele B, Ramogola-Masire D, Klausner JD, Morroni C. 2022. Evaluating the diagnosis and treatment of *Chlamydia trachomatis* and *Neisseria gonorrhoeae* in pregnant women to prevent adverse neonatal consequences in Gaborone, Botswana: protocol for the Maduo study. BMC Infect Dis 22:229.

25. Nogueira AT, Braun KM, Carabeo RA. 2017. Characterization of the Growth of *Chlamydia trachomatis* in In Vitro-Generated Stratified Epithelium. Front Cell Infect Microbiol 7:438.

26. Gitsels A, Sanders N, Vanrompay D. 2019. Chlamydial Infection From Outside to Inside. Front Microbiol 10:2329.

27. Moulder JW. 1991. Interaction of chlamydiae and host cells in vitro. Microbiol Rev 55:143-90.

28. Abdelrahman YM, Belland RJ. 2005. The chlamydial developmental cycle. FEMS Microbiol Rev 29:949-59.

29. Moore ER, Ouellette SP. 2014. Reconceptualizing the chlamydial inclusion as a pathogen-specified parasitic organelle: an expanded role for Inc proteins. Front Cell Infect Microbiol 4:157.

30. Clausen JD, Christiansen G, Holst HU, Birkelund S. 1997. *Chlamydia trachomatis* utilizes the host cell microtubule network during early events of infection. Mol Microbiol 25:441-9.

31. Grieshaber SS, Grieshaber NA, Hackstadt T. 2003. *Chlamydia trachomatis* uses host cell dynein to traffic to the microtubule-organizing center in a p50 dynamitin-independent process. J Cell Sci 116:3793-802.

32. Hackstadt T, Scidmore-Carlson MA, Shaw EI, Fischer ER. 1999. The *Chlamydia trachomatis* IncA protein is required for homotypic vesicle fusion. Cell Microbiol 1:119-30.

33. Todd WJ, Caldwell HD. 1985. The interaction of *Chlamydia trachomatis* with host cells: ultrastructural studies of the mechanism of release of a biovar II strain from HeLa 229 cells. J Infect Dis 151:1037-44.

34. Hybiske K, Stephens RS. 2007. Mechanisms of host cell exit by the intracellular bacterium *Chlamydia*. Proc Natl Acad Sci U S A 104:11430-5.

35. Nunes A, Gomes JP. 2014. Evolution, phylogeny, and molecular epidemiology of Chlamydia. Infect Genet Evol 23:49-64.

36. Bachmann NL, Polkinghorne A, Timms P. 2014. *Chlamydia* genomics: providing novel insights into chlamydial biology. Trends Microbiol 22:464-72.

37. Stephens RS, Kalman S, Lammel C, Fan J, Marathe R, Aravind L, Mitchell W, Olinger L, Tatusov RL, Zhao Q, Koonin EV, Davis RW. 1998. Genome sequence of an obligate intracellular pathogen of humans: *Chlamydia trachomatis*. Science 282:754-9.

38. Moulder JW. 1970. Glucose Metabolism of L Cells Before and After Infection with *Chlamydia psittaci*. J Bacteriol 104:1189-96.

39. Gill SD, Stewart RB. 1970. Effect of metabolic inhibitors on the production of *Chlamydia psittaci* by infected L cells. Can J Microbiol 16:1079-85.

40. Becker Y, Asher Y. 1972. Obligate parasitism of trachoma agent: lack of trachoma development in ethidium bromide-treated cells. Antimicrob Agents Chemother 1:171-3.

41. Hatch TP, Al-Hossainy E, Silverman JA. 1982. Adenine nucleotide and lysine transport in *Chlamydia psittaci*. J Bacteriol 150:662-70.

42.   Mehlitz A, Eylert E, Huber C, Lindner B, Vollmuth N, Karunakaran K, Goebel W, Eisenreich W, Rudel T. 2017. Metabolic adaptation of *Chlamydia trachomatis* to mammalian host cells. Mol Microbiol 103:1004-1019.

43.   Schwoppe C, Winkler HH, Neuhaus HE. 2002. Properties of the glucose-6-phosphate transporter from *Chlamydia pneumoniae* (HPTcp) and the glucose-6-phosphate sensor from *Escherichia coli* (UhpC). J Bacteriol 184:2108-15.

44.   Tjaden J, Winkler HH, Schwoppe C, Van Der Laan M, Mohlmann T, Neuhaus HE. 1999. Two nucleotide transport proteins in *Chlamydia trachomatis*, one for net nucleoside triphosphate uptake and the other for transport of energy. J Bacteriol 181:1196-202.

45.   Iliffe-Lee ER, McClarty G. 1999. Glucose metabolism in *Chlamydia trachomatis*: the 'energy parasite' hypothesis revisited. Mol Microbiol 33:177-87.

46.   Kokes M, Dunn JD, Granek JA, Nguyen BD, Barker JR, Valdivia RH, Bastidas RJ. 2015. Integrating chemical mutagenesis and whole-genome sequencing as a platform for forward and reverse genetic analysis of *Chlamydia*. Cell Host Microbe 17:716-25.

47.   Hatch TP, Miceli M, Silverman JA. 1985. Synthesis of protein in host-free reticulate bodies of *Chlamydia psittaci* and *Chlamydia trachomatis*. J Bacteriol 162:938-42.

48.   Plaunt MR, Hatch TP. 1988. Protein synthesis early in the developmental cycle of *Chlamydia psittaci*. Infect Immun 56:3021-5.

49.   Crenshaw RW, Fahr MJ, Wichlan DG, Hatch TP. 1990. Developmental cycle-specific host-free RNA synthesis in *Chlamydia* spp. Infect Immun 58:3194-201.

50. Skipp PJ, Hughes C, McKenna T, Edwards R, Langridge J, Thomson NR, Clarke IN. 2016. Quantitative Proteomics of the Infectious and Replicative Forms of *Chlamydia trachomatis*. PLoS One 11:e0149011.

51. Saka HA, Thompson JW, Chen YS, Kumar Y, Dubois LG, Moseley MA, Valdivia RH. 2011. Quantitative proteomics reveals metabolic and pathogenic properties of *Chlamydia trachomatis* developmental forms. Mol Microbiol 82:1185-203.

52. Omsland A, Sager J, Nair V, Sturdevant DE, Hackstadt T. 2012. Developmental stage-specific metabolic and transcriptional activity of *Chlamydia trachomatis* in an axenic medium. Proc Natl Acad Sci U S A 109:19781-5.

53. Rother M, Gonzalez E, Teixeira da Costa AR, Wask L, Gravenstein I, Pardo M, Pietzke M, Gurumurthy RK, Angermann J, Laudeley R, Glage S, Meyer M, Chumduri C, Kempa S, Dinkel K, Unger A, Klebl B, Klos A, Meyer TF. 2018. Combined Human Genome-wide RNAi and Metabolite Analyses Identify IMPDH as a Host-Directed Target against *Chlamydia* Infection. Cell Host Microbe 23:661-671 e8.

54. Warburg O. 1956. On the origin of cancer cells. Science 123:309-14.

55. Vander Heiden MG, Cantley LC, Thompson CB. 2009. Understanding the Warburg effect: the metabolic requirements of cell proliferation. Science 324:1029-33.

56. Asgari Y, Zabihinpour Z, Salehzadeh-Yazdi A, Schreiber F, Masoudi-Nejad A. 2015. Alterations in cancer cell metabolism: the Warburg effect and metabolic adaptation. Genomics 105:275-81.

57.   Wagner S, Grin I, Malmsheimer S, Singh N, Torres-Vargas CE, Westerhausen S. 2018. Bacterial type III secretion systems: a complex device for the delivery of bacterial effector proteins into eukaryotic host cells. FEMS Microbiol Lett 365.

58.   Hsia RC, Pannekoek Y, Ingerowski E, Bavoil PM. 1997. Type III secretion genes identify a putative virulence locus of *Chlamydia*. Mol Microbiol 25:351-9.

59.   Kalman S, Mitchell W, Marathe R, Lammel C, Fan J, Hyman RW, Olinger L, Grimwood J, Davis RW, Stephens RS. 1999. Comparative genomes of *Chlamydia pneumoniae* and *C. trachomatis*. Nat Genet 21:385-9.

60.   Read TD, Brunham RC, Shen C, Gill SR, Heidelberg JF, White O, Hickey EK, Peterson J, Utterback T, Berry K, Bass S, Linher K, Weidman J, Khouri H, Craven B, Bowman C, Dodson R, Gwinn M, Nelson W, DeBoy R, Kolonay J, McClarty G, Salzberg SL, Eisen J, Fraser CM. 2000. Genome sequences of *Chlamydia trachomatis* MoPn and *Chlamydia pneumoniae* AR39. Nucleic Acids Res 28:1397-406.

61.   Thomson NR, Yeats C, Bell K, Holden MT, Bentley SD, Livingstone M, Cerdeno-Tarraga AM, Harris B, Doggett J, Ormond D, Mungall K, Clarke K, Feltwell T, Hance Z, Sanders M, Quail MA, Price C, Barrell BG, Parkhill J, Longbottom D. 2005. The *Chlamydophila abortus* genome sequence reveals an array of variable proteins that contribute to interspecies variation. Genome Res 15:629-40.

62.   Bugalhao JN, Mota LJ. 2019. The multiple functions of the numerous *Chlamydia trachomatis* secreted proteins: the tip of the iceberg. Microb Cell 6:414-449.

63. Bannantine JP, Griffiths RS, Viratyosin W, Brown WJ, Rockey DD. 2000. A secondary structure motif predictive of protein localization to the chlamydial inclusion membrane. Cell Microbiol 2:35-47.

64. Dehoux P, Flores R, Dauga C, Zhong G, Subtil A. 2011. Multi-genome identification and characterization of chlamydiae-specific type III secretion substrates: the Inc proteins. BMC Genomics 12:109.

65. Lutter EI, Martens C, Hackstadt T. 2012. Evolution and conservation of predicted inclusion membrane proteins in chlamydiae. Comp Funct Genomics 2012:362104.

66. Shaw EI, Dooley CA, Fischer ER, Scidmore MA, Fields KA, Hackstadt T. 2000. Three temporal classes of gene expression during the *Chlamydia trachomatis* developmental cycle. Mol Microbiol 37:913-25.

67. Weber MM, Bauler LD, Lam J, Hackstadt T. 2015. Expression and localization of predicted inclusion membrane proteins in *Chlamydia trachomatis*. Infect Immun 83:4710-8.

68. Stanhope R, Flora E, Bayne C, Derre I. 2017. IncV, a FFAT motif-containing *Chlamydia* protein, tethers the endoplasmic reticulum to the pathogen-containing vacuole. Proc Natl Acad Sci U S A 114:12039-12044.

69. Wang X, Hybiske K, Stephens RS. 2018. Direct visualization of the expression and localization of chlamydial effector proteins within infected host cells. Pathog Dis 76.

70. Mital J, Miller NJ, Fischer ER, Hackstadt T. 2010. Specific chlamydial inclusion membrane proteins associate with active Src family kinases in microdomains that interact with the host microtubule network. Cell Microbiol 12:1235-49.

71. Nguyen PH, Lutter EI, Hackstadt T. 2018. *Chlamydia trachomatis* inclusion membrane protein MrcA interacts with the inositol 1,4,5-trisphosphate receptor type 3 (ITPR3) to regulate extrusion formation. PLoS Pathog 14:e1006911.

72. Li Z, Chen C, Chen D, Wu Y, Zhong Y, Zhong G. 2008. Characterization of fifty putative inclusion membrane proteins encoded in the *Chlamydia trachomatis* genome. Infect Immun 76:2746-57.

73. Scidmore-Carlson MA, Shaw EI, Dooley CA, Fischer ER, Hackstadt T. 1999. Identification and characterization of a *Chlamydia trachomatis* early operon encoding four novel inclusion membrane proteins. Mol Microbiol 33:753-65.

74. Derre I, Swiss R, Agaisse H. 2011. The lipid transfer protein CERT interacts with the *Chlamydia* inclusion protein IncD and participates to ER-*Chlamydia* inclusion membrane contact sites. PLoS Pathog 7:e1002092.

75. Elwell CA, Czudnochowski N, von Dollen J, Johnson JR, Nakagawa R, Mirrashidi K, Krogan NJ, Engel JN, Rosenberg OS. 2017. *Chlamydia* interfere with an interaction between the mannose-6-phosphate receptor and sorting nexins to counteract host restriction. Elife 6.

76. Paul B, Kim HS, Kerr MC, Huston WM, Teasdale RD, Collins BM. 2017. Structural basis for the hijacking of endosomal sorting nexin proteins by *Chlamydia trachomatis*. Elife 6.

77.   Sun Q, Yong X, Sun X, Yang F, Dai Z, Gong Y, Zhou L, Zhang X, Niu D, Dai L,
        Liu JJ, Jia D. 2017. Structural and functional insights into sorting nexin 5/6
        interaction with bacterial effector IncE. Signal Transduct Target Ther 2:17030.

78.   Gauliard E, Ouellette SP, Rueden KJ, Ladant D. 2015. Characterization of
        interactions between inclusion membrane proteins from *Chlamydia trachomatis*.
        Front Cell Infect Microbiol 5:13.

79.   Scidmore MA, Hackstadt T. 2001. Mammalian 14-3-3beta associates with the
        Chlamydia trachomatis inclusion membrane via its interaction with IncG. Mol
        Microbiol 39:1638-50.

80.   Saka HA, Thompson JW, Chen YS, Dubois LG, Haas JT, Moseley A, Valdivia
        RH. 2015. *Chlamydia trachomatis* Infection Leads to Defined Alterations to the
        Lipid Droplet Proteome in Epithelial Cells. PLoS One 10:e0124630.

81.   Johnson CM, Fisher DJ. 2013. Site-specific, insertional inactivation of incA in
        Chlamydia trachomatis using a group II intron. PLoS One 8:e83989.

82.   Bannantine JP, Stamm WE, Suchland RJ, Rockey DD. 1998. *Chlamydia
        trachomatis* IncA is localized to the inclusion membrane and is recognized by
        antisera from infected humans and primates. Infect Immun 66:6017-21.

83.   Suchland RJ, Rockey DD, Bannantine JP, Stamm WE. 2000. Isolates of
        Chlamydia trachomatis that occupy nonfusogenic inclusions lack IncA, a protein
        localized to the inclusion membrane. Infect Immun 68:360-7.

84.   Delevoye C, Nilges M, Dehoux P, Paumet F, Perrinet S, Dautry-Varsat A, Subtil
        A. 2008. SNARE protein mimicry by an intracellular bacterium. PLoS Pathog
        4:e1000022.

85.   Ronzone E, Paumet F. 2013. Two coiled-coil domains of *Chlamydia trachomatis* IncA affect membrane fusion events during infection. PLoS One 8:e69769.

86.   Cingolani G, McCauley M, Lobley A, Bryer AJ, Wesolowski J, Greco DL, Lokareddy RK, Ronzone E, Perilla JR, Paumet F. 2019. Structural basis for the homotypic fusion of chlamydial inclusions by the SNARE-like protein IncA. Nat Commun 10:2747.

87.   Cocchiaro JL, Kumar Y, Fischer ER, Hackstadt T, Valdivia RH. 2008. Cytoplasmic lipid droplets are translocated into the lumen of the *Chlamydia trachomatis* parasitophorous vacuole. Proc Natl Acad Sci U S A 105:9379-84.

88.   Sturdevant GL, Kari L, Gardner DJ, Olivares-Zavaleta N, Randall LB, Whitmire WM, Carlson JH, Goheen MM, Selleck EM, Martens C, Caldwell HD. 2010. Frameshift mutations in a single novel virulence factor alter the in vivo pathogenicity of *Chlamydia trachomatis* for the female murine genital tract. Infect Immun 78:3660-8.

89.   Sturdevant GL, Zhou B, Carlson JH, Whitmire WM, Song L, Caldwell HD. 2014. Infectivity of urogenital *Chlamydia trachomatis* plasmid-deficient, CT135-null, and double-deficient strains in female mice. Pathog Dis 71:90-2.

90.   Belland RJ, Zhong G, Crane DD, Hogan D, Sturdevant D, Sharma J, Beatty WL, Caldwell HD. 2003. Genomic transcriptional profiling of the developmental cycle of *Chlamydia trachomatis*. Proc Natl Acad Sci U S A 100:8478-83.

91.   Dumoux M, Menny A, Delacour D, Hayward RD. 2015. A *Chlamydia* effector recruits CEP170 to reprogram host microtubule organization. J Cell Sci 128:3420-34.

92.   Alzhanov DT, Weeks SK, Burnett JR, Rockey DD. 2009. Cytokinesis is blocked
       in mammalian cells transfected with *Chlamydia trachomatis* gene CT223. BMC
       Microbiol 9:2.

93.   Sharma J, Zhong Y, Dong F, Piper JM, Wang G, Zhong G. 2006. Profiling of
       human antibody responses to *Chlamydia trachomatis* urogenital tract infection
       using microplates arrayed with 156 chlamydial fusion proteins. Infect Immun
       74:1490-9.

94.   Lutter EI, Barger AC, Nair V, Hackstadt T. 2013. *Chlamydia trachomatis*
       inclusion membrane protein CT228 recruits elements of the myosin phosphatase
       pathway to regulate release mechanisms. Cell Rep 3:1921-31.

95.   Shaw JH, Key CE, Snider TA, Sah P, Shaw EI, Fisher DJ, Lutter EI. 2018.
       Genetic Inactivation of *Chlamydia trachomatis* Inclusion Membrane Protein
       CT228 Alters MYPT1 Recruitment, Extrusion Production, and Longevity of
       Infection. Front Cell Infect Microbiol 8:415.

96.   Faris R, Merling M, Andersen SE, Dooley CA, Hackstadt T, Weber MM. 2019.
       Chlamydia trachomatis CT229 Subverts Rab GTPase-Dependent CCV
       Trafficking Pathways to Promote Chlamydial Infection. Cell Rep 26:3380-3390
       e5.

97.   Rzomp KA, Moorhead AR, Scidmore MA. 2006. The GTPase Rab4 interacts
       with *Chlamydia trachomatis* inclusion membrane protein CT229. Infect Immun
       74:5362-73.

98.   Sixt BS, Bastidas RJ, Finethy R, Baxter RM, Carpenter VK, Kroemer G, Coers J,
       Valdivia RH. 2017. The *Chlamydia trachomatis* Inclusion Membrane Protein

CpoS Counteracts STING-Mediated Cellular Surveillance and Suicide Programs. Cell Host Microbe 21:113-121.

99. Weber MM, Lam JL, Dooley CA, Noriea NF, Hansen BT, Hoyt FH, Carmody AB, Sturdevant GL, Hackstadt T. 2017. Absence of Specific *Chlamydia trachomatis* Inclusion Membrane Proteins Triggers Premature Inclusion Membrane Lysis and Host Cell Death. Cell Rep 19:1406-1417.

100. Jia TJ, Liu DW, Luo JH, Zhong GM. 2007. [Localization of the hypothetical protein CT249 in the *Chlamydia trachomatis* inclusion membrane]. Wei Sheng Wu Xue Bao 47:645-8.

101. Almeida F, Luis MP, Pereira IS, Pais SV, Mota LJ. 2018. The Human Centrosomal Protein CCDC146 Binds *Chlamydia trachomatis* Inclusion Membrane Protein CT288 and Is Recruited to the Periphery of the *Chlamydia*-Containing Vacuole. Front Cell Infect Microbiol 8:254.

102. Starnbach MN, Loomis WP, Ovendale P, Regan D, Hess B, Alderson MR, Fling SP. 2003. An inclusion membrane protein from *Chlamydia trachomatis* enters the MHC class I pathway and stimulates a CD8+ T cell response. J Immunol 171:4742-9.

103. Sisko JL, Spaeth K, Kumar Y, Valdivia RH. 2006. Multifunctional analysis of *Chlamydia*-specific genes in a yeast expression system. Mol Microbiol 60:51-66.

104. Chen C, Chen D, Sharma J, Cheng W, Zhong Y, Liu K, Jensen J, Shain R, Arulanandam B, Zhong G. 2006. The hypothetical protein CT813 is localized in the *Chlamydia trachomatis* inclusion membrane and is immunogenic in women urogenitally infected with *C. trachomatis*. Infect Immun 74:4826-40.

105. Wesolowski J, Weber MM, Nawrotek A, Dooley CA, Calderon M, St Croix CM, Hackstadt T, Cherfils J, Paumet F. 2017. *Chlamydia* Hijacks ARF GTPases To Coordinate Microtubule Posttranslational Modifications and Golgi Complex Positioning. mBio 8.

106. Clifton DR, Fields KA, Grieshaber SS, Dooley CA, Fischer ER, Mead DJ, Carabeo RA, Hackstadt T. 2004. A chlamydial type III translocated protein is tyrosine-phosphorylated at the site of entry and associated with recruitment of actin. Proc Natl Acad Sci U S A 101:10166-71.

107. Kumar Y, Valdivia RH. 2008. Actin and intermediate filaments stabilize the *Chlamydia trachomatis* vacuole by forming dynamic structural scaffolds. Cell Host Microbe 4:159-69.

108. Bastidas RJ, Elwell CA, Engel JN, Valdivia RH. 2013. Chlamydial intracellular survival strategies. Cold Spring Harb Perspect Med 3:a010256.

109. Kumar Y, Valdivia RH. 2008. Reorganization of the host cytoskeleton by the intracellular pathogen *Chlamydia trachomatis*. Commun Integr Biol 1:175-7.

110. Volceanov L, Herbst K, Biniossek M, Schilling O, Haller D, Nolke T, Subbarayal P, Rudel T, Zieger B, Hacker G. 2014. Septins arrange F-actin-containing fibers on the *Chlamydia trachomatis* inclusion and are required for normal release of the inclusion by extrusion. mBio 5:e01802-14.

111. Patel AL, Chen X, Wood ST, Stuart ES, Arcaro KF, Molina DP, Petrovic S, Furdui CM, Tsang AW. 2014. Activation of epidermal growth factor receptor is required for *Chlamydia trachomatis* development. BMC Microbiol 14:277.

112. Haines A, Wesolowski J, Ryan NM, Monteiro-Bras T, Paumet F. 2021. Cross Talk between ARF1 and RhoA Coordinates the Formation of Cytoskeletal Scaffolds during *Chlamydia* Infection. mBio 12:e0239721.

113. Al-Zeer MA, Al-Younes HM, Kerr M, Abu-Lubad M, Gonzalez E, Brinkmann V, Meyer TF. 2014. *Chlamydia trachomatis* remodels stable microtubules to coordinate Golgi stack recruitment to the chlamydial inclusion surface. Mol Microbiol 94:1285-97.

114. Mital J, Lutter EI, Barger AC, Dooley CA, Hackstadt T. 2015. *Chlamydia trachomatis* inclusion membrane protein CT850 interacts with the dynein light chain DYNLT1 (Tctex1). Biochem Biophys Res Commun 462:165-70.

115. Hackstadt T, Scidmore MA, Rockey DD. 1995. Lipid metabolism in *Chlamydia trachomatis*-infected cells: directed trafficking of Golgi-derived sphingolipids to the chlamydial inclusion. Proc Natl Acad Sci U S A 92:4877-81.

116. Hackstadt T, Rockey DD, Heinzen RA, Scidmore MA. 1996. *Chlamydia trachomatis* interrupts an exocytic pathway to acquire endogenously synthesized sphingomyelin in transit from the Golgi apparatus to the plasma membrane. EMBO J 15:964-77.

117. Moore ER, Fischer ER, Mead DJ, Hackstadt T. 2008. The chlamydial inclusion preferentially intercepts basolaterally directed sphingomyelin-containing exocytic vacuoles. Traffic 9:2130-40.

118. Heuer D, Rejman Lipinski A, Machuy N, Karlas A, Wehrens A, Siedler F, Brinkmann V, Meyer TF. 2009. *Chlamydia causes* fragmentation of the Golgi compartment to ensure reproduction. Nature 457:731-5.

119. Gurumurthy RK, Chumduri C, Karlas A, Kimmig S, Gonzalez E, Machuy N, Rudel T, Meyer TF. 2014. Dynamin-mediated lipid acquisition is essential for *Chlamydia trachomatis* development. Mol Microbiol 94:186-201.

120. Matsumoto A, Bessho H, Uehira K, Suda T. 1991. Morphological studies of the association of mitochondria with chlamydial inclusions and the fusion of chlamydial inclusions. J Electron Microsc (Tokyo) 40:356-63.

121. Vanrompay D, Charlier G, Ducatelle R, Haesebrouck F. 1996. Ultrastructural changes in avian *Chlamydia psittaci* serovar A-, B-, and D-infected Buffalo Green Monkey cells. Infect Immun 64:1265-71.

122. Chowdhury SR, Reimer A, Sharan M, Kozjak-Pavlovic V, Eulalio A, Prusty BK, Fraunholz M, Karunakaran K, Rudel T. 2017. *Chlamydia* preserves the mitochondrial network necessary for replication via microRNA-dependent inhibition of fission. J Cell Biol 216:1071-1089.

123. Kurihara Y, Itoh R, Shimizu A, Walenna NF, Chou B, Ishii K, Soejima T, Fujikane A, Hiromatsu K. 2019. *Chlamydia trachomatis* targets mitochondrial dynamics to promote intracellular survival and proliferation. Cell Microbiol 21:e12962.

124. Peterson EM, de la Maza LM. 1988. *Chlamydia* parasitism: ultrastructural characterization of the interaction between the chlamydial cell envelope and the host cell. J Bacteriol 170:1389-92.

125. Giles DK, Wyrick PB. 2008. Trafficking of chlamydial antigens to the endoplasmic reticulum of infected epithelial cells. Microbes Infect 10:1494-503.

126. Elwell CA, Jiang S, Kim JH, Lee A, Wittmann T, Hanada K, Melancon P, Engel JN. 2011. *Chlamydia trachomatis* co-opts GBF1 and CERT to acquire host sphingomyelin for distinct roles during intracellular development. PLoS Pathog 7:e1002198.

127. Dumoux M, Clare DK, Saibil HR, Hayward RD. 2012. Chlamydiae assemble a pathogen synapse to hijack the host endoplasmic reticulum. Traffic 13:1612-27.

128. Dumoux M, Nans A, Saibil HR, Hayward RD. 2015. Making connections: snapshots of chlamydial type III secretion systems in contact with host membranes. Curr Opin Microbiol 23:1-7.

129. Prinz WA. 2014. Bridging the gap: membrane contact sites in signaling, metabolism, and organelle dynamics. J Cell Biol 205:759-69.

130. Funato K, Riezman H, Muniz M. 2020. Vesicular and non-vesicular lipid export from the ER to the secretory pathway. Biochim Biophys Acta Mol Cell Biol Lipids 1865:158453.

131. Scorrano L, De Matteis MA, Emr S, Giordano F, Hajnoczky G, Kornmann B, Lackner LL, Levine TP, Pellegrini L, Reinisch K, Rizzuto R, Simmen T, Stenmark H, Ungermann C, Schuldiner M. 2019. Coming together to define membrane contact sites. Nat Commun 10:1287.

132. Wu H, Carvalho P, Voeltz GK. 2018. Here, there, and everywhere: The importance of ER membrane contact sites. Science 361.

133. Phillips MJ, Voeltz GK. 2016. Structure and function of ER membrane contact sites with other organelles. Nat Rev Mol Cell Biol 17:69-82.

134. Levine T. 2004. Short-range intracellular trafficking of small molecules across endoplasmic reticulum junctions. Trends Cell Biol 14:483-90.

135. Chung J, Torta F, Masai K, Lucast L, Czapla H, Tanner LB, Narayanaswamy P, Wenk MR, Nakatsu F, De Camilli P. 2015. INTRACELLULAR TRANSPORT. PI4P/phosphatidylserine countertransport at ORP5- and ORP8-mediated ER-plasma membrane contacts. Science 349:428-32.

136. Kumagai K, Hanada K. 2019. Structure, functions and regulation of CERT, a lipid-transfer protein for the delivery of ceramide at the ER-Golgi membrane contact sites. FEBS Lett 593:2366-2377.

137. Selitrennik M, Lev S. 2016. The role of phosphatidylinositol-transfer proteins at membrane contact sites. Biochem Soc Trans 44:419-24.

138. Honscher C, Mari M, Auffarth K, Bohnert M, Griffith J, Geerts W, van der Laan M, Cabrera M, Reggiori F, Ungermann C. 2014. Cellular metabolism regulates contact sites between vacuoles and mitochondria. Dev Cell 30:86-94.

139. Duan G, Walther D. 2015. The roles of post-translational modifications in the context of protein interaction networks. PLoS Comput Biol 11:e1004049.

140. Kumagai K, Kawano-Kawada M, Hanada K. 2014. Phosphoregulation of the ceramide transport protein CERT at serine 315 in the interaction with VAMP-associated protein (VAP) for inter-organelle trafficking of ceramide in mammalian cells. J Biol Chem 289:10748-10760.

141. Lev S. 2010. Non-vesicular lipid transport by lipid-transfer proteins and beyond. Nat Rev Mol Cell Biol 11:739-50.

142. Hanada K. 2018. Lipid transfer proteins rectify inter-organelle flux and accurately deliver lipids at membrane contact sites. J Lipid Res 59:1341-1366.

143. Foskett JK, Daniel Mak DO. 2010. Regulation of IP(3)R Channel Gating by Ca(2+) and Ca(2+) Binding Proteins. Curr Top Membr 66:235-72.

144. Soboloff J, Rothberg BS, Madesh M, Gill DL. 2012. STIM proteins: dynamic calcium signal transducers. Nat Rev Mol Cell Biol 13:549-65.

145. Srikanth S, Gwack Y. 2012. Orai1, STIM1, and their associating partners. J Physiol 590:4169-77.

146. Prakriya M. 2013. The theory, operation, and roles of store-operated calcium. Curr Top Membr 71:xi-xii.

147. Lunz V, Romanin C, Frischauf I. 2019. STIM1 activation of Orai1. Cell Calcium 77:29-38.

148. Park CY, Hoover PJ, Mullins FM, Bachhawat P, Covington ED, Raunser S, Walz T, Garcia KC, Dolmetsch RE, Lewis RS. 2009. STIM1 clusters and activates CRAC channels via direct binding of a cytosolic domain to Orai1. Cell 136:876-90.

149. Murphy SE, Levine TP. 2016. VAP, a Versatile Access Point for the Endoplasmic Reticulum: Review and analysis of FFAT-like motifs in the VAPome. Biochim Biophys Acta 1861:952-961.

150. Dong R, Saheki Y, Swarup S, Lucast L, Harper JW, De Camilli P. 2016. Endosome-ER Contacts Control Actin Nucleation and Retromer Function through VAP-Dependent Regulation of PI4P. Cell 166:408-423.

151. Eden ER, Sanchez-Heras E, Tsapara A, Sobota A, Levine TP, Futter CE. 2016. Annexin A1 Tethers Membrane Contact Sites that Mediate ER to Endosome Cholesterol Transport. Dev Cell 37:473-83.

152. Di Mattia T, Wilhelm LP, Ikhlef S, Wendling C, Spehner D, Nomine Y, Giordano F, Mathelin C, Drin G, Tomasetto C, Alpy F. 2018. Identification of MOSPD2, a novel scaffold for endoplasmic reticulum membrane contact sites. EMBO Rep 19.

153. Cabukusta B, Berlin I, van Elsland DM, Forkink I, Spits M, de Jong AWM, Akkermans J, Wijdeven RHM, Janssen GMC, van Veelen PA, Neefjes J. 2020. Human VAPome Analysis Reveals MOSPD1 and MOSPD3 as Membrane Contact Site Proteins Interacting with FFAT-Related FFNT Motifs. Cell Rep 33:108475.

154. Loewen CJ, Roy A, Levine TP. 2003. A conserved ER targeting motif in three families of lipid binding proteins and in Opi1p binds VAP. EMBO J 22:2025-35.

155. Loewen CJ, Levine TP. 2005. A highly conserved binding site in vesicle-associated membrane protein-associated protein (VAP) for the FFAT motif of lipid-binding proteins. J Biol Chem 280:14097-104.

156. Mikitova V, Levine TP. 2012. Analysis of the key elements of FFAT-like motifs identifies new proteins that potentially bind VAP on the ER, including two AKAPs and FAPP2. PLoS One 7:e30455.

157. Slee JA, Levine TP. 2019. Systematic prediction of FFAT motifs across eukaryote proteomes identifies nucleolar and eisosome proteins with the predicted capacity to form bridges to the endoplasmic reticulum. Contact (Thousand Oaks) 2:1-21.

158. Di Mattia T, Martinet A, Ikhlef S, McEwen AG, Nomine Y, Wendling C, Poussin-Courmontagne P, Voilquin L, Eberling P, Ruffenach F, Cavarelli J, Slee J, Levine TP, Drin G, Tomasetto C, Alpy F. 2020. FFAT motif phosphorylation controls formation and lipid transfer function of inter-organelle contacts. EMBO J 39:e104369.

159. Agaisse H, Derre I. 2014. Expression of the effector protein IncD in *Chlamydia trachomatis* mediates recruitment of the lipid transfer protein CERT and the endoplasmic reticulum-resident protein VAPB to the inclusion membrane. Infect Immun 82:2037-47.

160. Agaisse H, Derré I. 2015. STIM1 Is a Novel Component of ER-*Chlamydia trachomatis* Inclusion Membrane Contact Sites. PLoS One 10:e0125671.

161. Nguyen TMT, Kim J, Doan TT, Lee MW, Lee M. 2020. APEX Proximity Labeling as a Versatile Tool for Biological Research. Biochemistry 59:260-269.

162. Trinkle-Mulcahy L. 2019. Recent advances in proximity-based labeling methods for interactome mapping. F1000Res 8.

163. Samavarchi-Tehrani P, Samson R, Gingras AC. 2020. Proximity Dependent Biotinylation: Key Enzymes and Adaptation to Proteomics Approaches. Mol Cell Proteomics 19:757-773.

164. Choi-Rhee E, Schulman H, Cronan JE. 2004. Promiscuous protein biotinylation by *Escherichia coli* biotin protein ligase. Protein Sci 13:3043-50.

165. Roux KJ, Kim DI, Raida M, Burke B. 2012. A promiscuous biotin ligase fusion protein identifies proximal and interacting proteins in mammalian cells. J Cell Biol 196:801-10.

166. Lam SS, Martell JD, Kamer KJ, Deerinck TJ, Ellisman MH, Mootha VK, Ting AY. 2015. Directed evolution of APEX2 for electron microscopy and proximity labeling. Nat Methods 12:51-4.

167. Rhee HW, Zou P, Udeshi ND, Martell JD, Mootha VK, Carr SA, Ting AY. 2013. Proteomic mapping of mitochondria in living cells via spatially restricted enzymatic tagging. Science 339:1328-1331.

168. Hua R, Cheng D, Coyaud E, Freeman S, Di Pietro E, Wang Y, Vissa A, Yip CM, Fairn GD, Braverman N, Brumell JH, Trimble WS, Raught B, Kim PK. 2017. VAPs and ACBD5 tether peroxisomes to the ER for peroxisome maintenance and lipid homeostasis. J Cell Biol 216:367-377.

169. Cho IT, Adelmant G, Lim Y, Marto JA, Cho G, Golden JA. 2017. Ascorbate peroxidase proximity labeling coupled with biochemical fractionation identifies promoters of endoplasmic reticulum-mitochondrial contacts. J Biol Chem 292:16382-16392.

170. Kabeiseman EJ, Cichos KH, Moore ER. 2014. The eukaryotic signal sequence, YGRL, targets the chlamydial inclusion. Front Cell Infect Microbiol 4:129.

171. Mojica SA, Hovis KM, Frieman MB, Tran B, Hsia RC, Ravel J, Jenkins-Houk C, Wilson KL, Bavoil PM. 2015. SINC, a type III secreted protein of *Chlamydia psittaci*, targets the inner nuclear membrane of infected cells and uninfected neighbors. Mol Biol Cell 26:1918-34.

172. McKuen MJ, Mueller KE, Bae YS, Fields KA. 2017. Fluorescence-Reported Allelic Exchange Mutagenesis Reveals a Role for *Chlamydia trachomatis* TmeA in Invasion That Is Independent of Host AHNAK. Infect Immun 85.

173. Rucks EA, Olson MG, Jorgenson LM, Srinivasan RR, Ouellette SP. 2017. Development of a Proximity Labeling System to Map the *Chlamydia trachomatis* Inclusion Membrane. Front Cell Infect Microbiol 7:40.

174. Olson MG, Widner RE, Jorgenson LM, Lawrence A, Lagundzin D, Woods NT, Ouellette SP, Rucks EA. 2019. Proximity Labeling To Map Host-Pathogen Interactions at the Membrane of a Bacterium-Containing Vacuole in *Chlamydia trachomatis*-Infected Human Cells. Infect Immun 87.

175. Dickinson MS, Anderson LN, Webb-Robertson BM, Hansen JR, Smith RD, Wright AT, Hybiske K. 2019. Proximity-dependent proteomics of the *Chlamydia trachomatis* inclusion membrane reveals functional interactions with endoplasmic reticulum exit sites. PLoS Pathog 15:e1007698.

176. Almeida F, Borges V, Ferreira R, Borrego MJ, Gomes JP, Mota LJ. 2012. Polymorphisms in inc proteins and differential expression of inc genes among *Chlamydia trachomatis* strains correlate with invasiveness and tropism of lymphogranuloma venereum isolates. J Bacteriol 194:6574-85.

177. Nicholson TL, Olinger L, Chong K, Schoolnik G, Stephens RS. 2003. Global stage-specific gene regulation during the developmental cycle of *Chlamydia trachomatis*. J Bacteriol 185:3179-89.

178. James C, Kehlenbach RH. 2021. The Interactome of the VAP Family of Proteins: An Overview. Cells 10.

179. Levine T, Loewen C. 2006. Inter-organelle membrane contact sites: through a glass, darkly. Curr Opin Cell Biol 18:371-8.

180. Lebiedzinska M, Szabadkai G, Jones AW, Duszynski J, Wieckowski MR. 2009. Interactions between the endoplasmic reticulum, mitochondria, plasma membrane and other subcellular organelles. Int J Biochem Cell Biol 41:1805-16.

181. Derré I, Pypaert M, Dautry-Varsat A, Agaisse H. 2007. RNAi screen in Drosophila cells reveals the involvement of the Tom complex in *Chlamydia* infection. PLoS Pathog 3:1446-58.

182. Cortina ME, Ende RJ, Bishop RC, Bayne C, Derré I. 2019. *Chlamydia trachomatis* and *Chlamydia muridarum* spectinomycin resistant vectors and a transcriptional fluorescent reporter to monitor conversion from replicative to infectious bacteria. PLoS One 14:e0217753.

183. Fisher DJ, Fernandez RE, Maurelli AT. 2013. *Chlamydia trachomatis* transports NAD via the Npt1 ATP/ADP translocase. J Bacteriol 195:3381-6.

184. Nelson DL, Cox MM. 2008. Glycolysis, Gluconeogenesis, and the Pentose Phosphate Pathway, p 527-568, Lehninger Principles of Biochemistry, 5th ed. W.H. Freeman, New York.

185. Rockey DD, Heinzen RA, Hackstadt T. 1995. Cloning and characterization of a *Chlamydia psittaci* gene coding for a protein localized in the inclusion membrane of infected cells. Mol Microbiol 15:617-26.

186. Arnold H, Pette D. 1968. Binding of glycolytic enzymes to structure proteins of the muscle. Eur J Biochem 6:163-71.

187. Wang J, Morris AJ, Tolan DR, Pagliaro L. 1996. The molecular nature of the F-actin binding activity of aldolase revealed with site-directed mutants. J Biol Chem 271:6861-5.

188. Clarke FM, Masters CJ. 1975. On the association of glycolytic enzymes with structural proteins of skeletal muscle. Biochim Biophys Acta 381:37-46.

189. Boiteux A, Hess B. 1981. Design of glycolysis. Philos Trans R Soc Lond B Biol Sci 293:5-22.

190. Brooks SP, Storey KB. 1991. Where is the glycolytic complex? A critical evaluation of present data from muscle tissue. FEBS Lett 278:135-8.

191. Menard L, Maughan D, Vigoreaux J. 2014. The structural and functional coordination of glycolytic enzymes in muscle: evidence of a metabolon? Biology (Basel) 3:623-44.

192. Opperdoes FR, Borst P. 1977. Localization of nine glycolytic enzymes in a microbody-like organelle in *Trypanosoma brucei*: the glycosome. FEBS Lett 80:360-4.

193. Michels PA, Bringaud F, Herman M, Hannaert V. 2006. Metabolic functions of glycosomes in trypanosomatids. Biochim Biophys Acta 1763:1463-77.

194. Crowe LP, Wilkinson CL, Nicholson KR, Morris MT. 2020. *Trypanosoma brucei* Pex13.2 Is an Accessory Peroxin That Functions in the Import of Peroxisome Targeting Sequence Type 2 Proteins and Localizes to Subdomains of the Glycosome. mSphere 5.

195. Haanstra JR, Gonzalez-Marcano EB, Gualdron-Lopez M, Michels PA. 2016. Biogenesis, maintenance and dynamics of glycosomes in trypanosomatid parasites. Biochim Biophys Acta 1863:1038-48.

196. Jang S, Nelson JC, Bend EG, Rodriguez-Laureano L, Tueros FG, Cartagenova L, Underwood K, Jorgensen EM, Colon-Ramos DA. 2016. Glycolytic Enzymes

Localize to Synapses under Energy Stress to Support Synaptic Function. Neuron 90:278-91.

197.   Aeberhard L, Banhart S, Fischer M, Jehmlich N, Rose L, Koch S, Laue M, Renard BY, Schmidt F, Heuer D. 2015. The Proteome of the Isolated *Chlamydia trachomatis* Containing Vacuole Reveals a Complex Trafficking Platform Enriched for Retromer Components. PLoS Pathog 11:e1004883.

198.   Mirrashidi KM, Elwell CA, Verschueren E, Johnson JR, Frando A, Von Dollen J, Rosenberg O, Gulbahce N, Jang G, Johnson T, Jager S, Gopalakrishnan AM, Sherry J, Dunn JD, Olive A, Penn B, Shales M, Cox JS, Starnbach MN, Derre I, Valdivia R, Krogan NJ, Engel J. 2015. Global Mapping of the Inc-Human Interactome Reveals that Retromer Restricts *Chlamydia* Infection. Cell Host Microbe 18:109-21.

199.   Lee JK, Enciso GA, Boassa D, Chander CN, Lou TH, Pairawan SS, Guo MC, Wan FYM, Ellisman MH, Sutterlin C, Tan M. 2018. Replication-dependent size reduction precedes differentiation in *Chlamydia trachomatis*. Nat Commun 9:45.

200.   Yang M, Rajeeve K, Rudel T, Dandekar T. 2019. Comprehensive Flux Modeling of *Chlamydia trachomatis* Proteome and qRT-PCR Data Indicate Biphasic Metabolic Differences Between Elementary Bodies and Reticulate Bodies During Infection. Front Microbiol 10:2350.

201.   Heinzen RA, Hackstadt T. 1997. The *Chlamydia trachomatis* parasitophorous vacuolar membrane is not passively permeable to low-molecular-weight compounds. Infect Immun 65:1088-94.

202. Grieshaber S, Swanson JA, Hackstadt T. 2002. Determination of the physical environment within the *Chlamydia trachomatis* inclusion using ion-selective ratiometric probes. Cell Microbiol 4:273-83.

203. Lowden NM, Yeruva L, Johnson CM, Bowlin AK, Fisher DJ. 2015. Use of aminoglycoside 3' adenyltransferase as a selection marker for *Chlamydia trachomatis* intron-mutagenesis and in vivo intron stability. BMC Res Notes 8:570.

204. Borges V, Ferreira R, Nunes A, Nogueira P, Borrego MJ, Gomes JP. 2010. Normalization strategies for real-time expression data in *Chlamydia trachomatis*. J Microbiol Methods 82:256-64.

205. Livak KJ, Schmittgen TD. 2001. Analysis of relative gene expression data using real-time quantitative PCR and the 2(-Delta Delta C(T)) Method. Methods 25:402-8.

206. Prinz WA, Toulmay A, Balla T. 2020. The functional universe of membrane contact sites. Nat Rev Mol Cell Biol 21:7-24.

207. Area-Gomez E, Del Carmen Lara Castillo M, Tambini MD, Guardia-Laguarta C, de Groof AJ, Madra M, Ikenouchi J, Umeda M, Bird TD, Sturley SL, Schon EA. 2012. Upregulated function of mitochondria-associated ER membranes in Alzheimer disease. EMBO J 31:4106-23.

208. Stoica R, De Vos KJ, Paillusson S, Mueller S, Sancho RM, Lau KF, Vizcay-Barrena G, Lin WL, Xu YF, Lewis J, Dickson DW, Petrucelli L, Mitchell JC, Shaw CE, Miller CC. 2014. ER-mitochondria associations are regulated by the

VAPB-PTPIP51 interaction and are disrupted by ALS/FTD-associated TDP-43.
Nat Commun 5:3996.

209.   Castro IG, Schuldiner M, Zalckvar E. 2018. Mind the Organelle Gap -
Peroxisome Contact Sites in Disease. Trends Biochem Sci 43:199-210.

210.   Eisenberg-Bord M, Shai N, Schuldiner M, Bohnert M. 2016. A Tether Is a Tether
Is a Tether: Tethering at Membrane Contact Sites. Dev Cell 39:395-409.

211.   Murphy SE, Levine TP. 2016. VAP, a Versatile Access Point for the Endoplasmic
Reticulum: Review and analysis of FFAT-like motifs in the VAPome. Biochim
Biophys Acta doi:10.1016/j.bbalip.2016.02.009.

212.   Furuita K, Jee J, Fukada H, Mishima M, Kojima C. 2010. Electrostatic interaction
between oxysterol-binding protein and VAMP-associated protein A revealed by
NMR and mutagenesis studies. J Biol Chem 285:12961-70.

213.   Derre I. 2017. Hijacking of Membrane Contact Sites by Intracellular Bacterial
Pathogens. Adv Exp Med Biol 997:211-223.

214.   Justis AV, Hansen B, Beare PA, King KB, Heinzen RA, Gilk SD. 2017.
Interactions between the *Coxiella burnetii* parasitophorous vacuole and the
endoplasmic reticulum involve the host protein ORP1L. Cell Microbiol 19.

215.   McCune BT, Tang W, Lu J, Eaglesham JB, Thorne L, Mayer AE, Condiff E, Nice
TJ, Goodfellow I, Krezel AM, Virgin HW. 2017. Noroviruses Co-opt the
Function of Host Proteins VAPA and VAPB for Replication via a Phenylalanine-
Phenylalanine-Acidic-Tract-Motif Mimic in Nonstructural Viral Protein NS1/2.
mBio 8.

216. Ishikawa-Sasaki K, Nagashima S, Taniguchi K, Sasaki J. 2018. A model of OSBP-mediated cholesterol supply to Aichi virus RNA replication sites involving protein-protein interactions among viral proteins, ACBD3, OSBP, VAP-A/B, and SAC1. J Virol doi:10.1128/JVI.01952-17.

217. Lara-Tejero M, Galan JE. 2019. The Injectisome, a Complex Nanomachine for Protein Injection into Mammalian Cells. EcoSal Plus 8.

218. Allen JJ, Li M, Brinkworth CS, Paulson JL, Wang D, Hubner A, Chou WH, Davis RJ, Burlingame AL, Messing RO, Katayama CD, Hedrick SM, Shokat KM. 2007. A semisynthetic epitope for kinase substrates. Nat Methods 4:511-6.

219. Buchou T, Vernet M, Blond O, Jensen HH, Pointu H, Olsen BB, Cochet C, Issinger OG, Boldyreff B. 2003. Disruption of the regulatory beta subunit of protein kinase CK2 in mice leads to a cell-autonomous defect and early embryonic lethality. Mol Cell Biol 23:908-15.

220. Zhang R, Ou HY, Zhang CT. 2004. DEG: a database of essential genes. Nucleic Acids Res 32:D271-2.

221. Rusin SF, Adamo ME, Kettenbach AN. 2017. Identification of Candidate Casein Kinase 2 Substrates in Mitosis by Quantitative Phosphoproteomics. Front Cell Dev Biol 5:97.

222. Borgo C, Cesaro L, Hirota T, Kuwata K, D'Amore C, Ruppert T, Blatnik R, Salvi M, Pinna LA. 2021. Comparing the efficacy and selectivity of Ck2 inhibitors. A phosphoproteomics approach. Eur J Med Chem 214:113217.

223. Litchfield DW. 2003. Protein kinase CK2: structure, regulation and role in cellular decisions of life and death. Biochem J 369:1-15.

224. Kawano M, Kumagai K, Nishijima M, Hanada K. 2006. Efficient trafficking of ceramide from the endoplasmic reticulum to the Golgi apparatus requires a VAMP-associated protein-interacting FFAT motif of CERT. J Biol Chem 281:30279-88.

225. Xu L, Wang X, Zhou J, Qiu Y, Shang W, Liu JP, Wang L, Tong C. 2020. Miga-mediated endoplasmic reticulum-mitochondria contact sites regulate neuronal homeostasis. Elife 9.

226. Kors S, Hacker C, Bolton C, Maier R, Reimann L, Kitchener EJA, Warscheid B, Costello JL, Schrader M. 2022. Regulating peroxisome-ER contacts via the ACBD5-VAPB tether by FFAT motif phosphorylation and GSK3beta. J Cell Biol 221.

227. Miller CJ, Turk BE. 2018. Homing in: Mechanisms of Substrate Targeting by Protein Kinases. Trends Biochem Sci 43:380-394.

228. Guillen-Samander A, Leonzino M, Hanna MG, Tang N, Shen H, De Camilli P. 2021. VPS13D bridges the ER to mitochondria and peroxisomes via Miro. J Cell Biol 220.

229. Johnson B, Leek AN, Sole L, Maverick EE, Levine TP, Tamkun MM. 2018. Kv2 potassium channels form endoplasmic reticulum/plasma membrane junctions via interaction with VAPA and VAPB. Proc Natl Acad Sci U S A 115:E7331-E7340.

230. Kumagai K, Kawano-Kawada M, Hanada K. 2014. Phosphoregulation of the ceramide transport protein CERT at serine 315 in the interaction with VAMP-associated protein (VAP) for inter-organelle trafficking of ceramide in mammalian cells. J Biol Chem 289:10748-60.

231. Neefjes J, Cabukusta B. 2021. What the VAP: The Expanded VAP Family of Proteins Interacting With FFAT and FFAT-Related Motifs for Interorganellar Contact. Contact (Thousand Oaks) 4:25152564211012246.

232. Mondino S, Schmidt S, Buchrieser C. 2020. Molecular Mimicry: a Paradigm of Host-Microbe Coevolution Illustrated by Legionella. mBio 11.

233. Park KS, Mohapatra DP, Misonou H, Trimmer JS. 2006. Graded regulation of the Kv2.1 potassium channel by variable phosphorylation. Science 313:976-9.

234. Filhol O, Nueda A, Martel V, Gerber-Scokaert D, Benitez MJ, Souchier C, Saoudi Y, Cochet C. 2003. Live-cell fluorescence imaging reveals the dynamics of protein kinase CK2 individual subunits. Mol Cell Biol 23:975-87.

235. Folsch H, Pypaert M, Schu P, Mellman I. 2001. Distribution and function of AP-1 clathrin adaptor complexes in polarized epithelial cells. J Cell Biol 152:595-606.

236. Ende RJ, Derre I. 2020. Host and Bacterial Glycolysis during *Chlamydia trachomatis* Infection. Infect Immun 88.

237. Hadley KC, Rakhit R, Guo H, Sun Y, Jonkman JE, McLaurin J, Hazrati LN, Emili A, Chakrabartty A. 2015. Determining composition of micron-scale protein deposits in neurodegenerative disease by spatially targeted optical microproteomics. Elife 4.

238. Yin B, Mendez R, Zhao XY, Rakhit R, Hsu KL, Ewald SE. 2020. Automated Spatially Targeted Optical Microproteomics (autoSTOMP) to Determine Protein Complexity of Subcellular Structures. Anal Chem 92:2005-2010.

239. Teo G, Liu G, Zhang J, Nesvizhskii AI, Gingras AC, Choi H. 2014. SAINTexpress: improvements and additional features in Significance Analysis of INTeractome software. J Proteomics 100:37-43.

240. Olson MG, Ouellette SP, Rucks EA. 2020. A meta-analysis of affinity purification-mass spectrometry experimental systems used to identify eukaryotic and chlamydial proteins at the *Chlamydia trachomatis* inclusion membrane. J Proteomics 212:103595.

241. Wu YH, Yang Y, Chen CH, Hsiao CJ, Li TN, Liao KJ, Watashi K, Chen BS, Wang LH. 2021. Aerobic glycolysis supports hepatitis B virus protein synthesis through interaction between viral surface antigen and pyruvate kinase isoform M2. PLoS Pathog 17:e1008866.

242. Anastasiou D, Yu Y, Israelsen WJ, Jiang JK, Boxer MB, Hong BS, Tempel W, Dimov S, Shen M, Jha A, Yang H, Mattaini KR, Metallo CM, Fiske BP, Courtney KD, Malstrom S, Khan TM, Kung C, Skoumbourdis AP, Veith H, Southall N, Walsh MJ, Brimacombe KR, Leister W, Lunt SY, Johnson ZR, Yen KE, Kunii K, Davidson SM, Christofk HR, Austin CP, Inglese J, Harris MH, Asara JM, Stephanopoulos G, Salituro FG, Jin S, Dang L, Auld DS, Park HW, Cantley LC, Thomas CJ, Vander Heiden MG. 2012. Pyruvate kinase M2 activators promote tetramer formation and suppress tumorigenesis. Nat Chem Biol 8:839-47.

243. Puchulu-Campanella E, Chu H, Anstee DJ, Galan JA, Tao WA, Low PS. 2013. Identification of the components of a glycolytic enzyme metabolon on the human red blood cell membrane. J Biol Chem 288:848-58.

244. Zhang Y, Sampathkumar A, Kerber SM, Swart C, Hille C, Seerangan K, Graf A, Sweetlove L, Fernie AR. 2020. A moonlighting role for enzymes of glycolysis in the co-localization of mitochondria and chloroplasts. Nat Commun 11:4509.

245. Alvarez DE, Agaisse H. 2012. Casein kinase 2 regulates vaccinia virus actin tail formation. Virology 423:143-51.

246. Mohl BP, Roy P. 2016. Cellular Casein Kinase 2 and Protein Phosphatase 2A Modulate Replication Site Assembly of Bluetongue Virus. J Biol Chem 291:14566-74.

247. Nogalski MT, Podduturi JP, DeMeritt IB, Milford LE, Yurochko AD. 2007. The human cytomegalovirus virion possesses an activated casein kinase II that allows for the rapid phosphorylation of the inhibitor of NF-kappaB, IkappaBalpha. J Virol 81:5305-14.

248. Piirsoo A, Piirsoo M, Kala M, Sankovski E, Lototskaja E, Levin V, Salvi M, Ustav M. 2019. Activity of CK2alpha protein kinase is required for efficient replication of some HPV types. PLoS Pathog 15:e1007788.

249. Franck N, Le Seyec J, Guguen-Guillouzo C, Erdtmann L. 2005. Hepatitis C virus NS2 protein is phosphorylated by the protein kinase CK2 and targeted for degradation to the proteasome. J Virol 79:2700-8.

250. Chong R, Swiss R, Briones G, Stone KL, Gulcicek EE, Agaisse H. 2009. Regulatory mimicry in *Listeria monocytogenes* actin-based motility. Cell Host Microbe 6:268-78.

251. Cory GO, Cramer R, Blanchoin L, Ridley AJ. 2003. Phosphorylation of the WASP-VCA domain increases its affinity for the Arp2/3 complex and enhances actin polymerization by WASP. Mol Cell 11:1229-39.

252. Pocha SM, Cory GO. 2009. WAVE2 is regulated by multiple phosphorylation events within its VCA domain. Cell Motil Cytoskeleton 66:36-47.

253. Alberti S. 1999. HIKE, a candidate protein binding site for PH domains, is a major regulatory region of Gbeta proteins. Proteins 35:360-3.

254. Olsten ME, Canton DA, Zhang C, Walton PA, Litchfield DW. 2004. The Pleckstrin homology domain of CK2 interacting protein-1 is required for interactions and recruitment of protein kinase CK2 to the plasma membrane. J Biol Chem 279:42114-27.

255. Kumagai K, Kawano M, Shinkai-Ouchi F, Nishijima M, Hanada K. 2007. Interorganelle trafficking of ceramide is regulated by phosphorylation-dependent cooperativity between the PH and START domains of CERT. J Biol Chem 282:17758-66.

256. Nishi H, Shaytan A, Panchenko AR. 2014. Physicochemical mechanisms of protein regulation by phosphorylation. Front Genet 5:270.

257. Stoica R, Paillusson S, Gomez-Suaga P, Mitchell JC, Lau DH, Gray EH, Sancho RM, Vizcay-Barrena G, De Vos KJ, Shaw CE, Hanger DP, Noble W, Miller CC. 2016. ALS/FTD-associated FUS activates GSK-3beta to disrupt the VAPB-PTPIP51 interaction and ER-mitochondria associations. EMBO Rep 17:1326-42.

258. Sah P, Nelson NH, Shaw JH, Lutter EI. 2019. *Chlamydia trachomatis* recruits protein kinase C during infection. Pathog Dis 77.

259. Xue Y, Liu Z, Cao J, Ma Q, Gao X, Wang Q, Jin C, Zhou Y, Wen L, Ren J. 2011. GPS 2.1: enhanced prediction of kinase-specific phosphorylation sites with an algorithm of motif length selection. Protein Eng Des Sel 24:255-60.

260. Brautigan DL, Shenolikar S. 2018. Protein Serine/Threonine Phosphatases: Keys to Unlocking Regulators and Substrates. Annu Rev Biochem 87:921-964.

261. Ueki Y, Kruse T, Weisser MB, Sundell GN, Larsen MSY, Mendez BL, Jenkins NP, Garvanska DH, Cressey L, Zhang G, Davey N, Montoya G, Ivarsson Y, Kettenbach AN, Nilsson J. 2019. A Consensus Binding Motif for the PP4 Protein Phosphatase. Mol Cell 76:953-964 e6.

262. Popescu M, Gurel Z, Ronni T, Song C, Hung KY, Payne KJ, Dovat S. 2009. Ikaros stability and pericentromeric localization are regulated by protein phosphatase 1. J Biol Chem 284:13869-13880.

263. Wang H, Song C, Gurel Z, Song N, Ma J, Ouyang H, Lai L, Payne KJ, Dovat S. 2014. Protein phosphatase 1 (PP1) and Casein Kinase II (CK2) regulate Ikaros-mediated repression of TdT in thymocytes and T-cell leukemia. Pediatr Blood Cancer 61:2230-5.

264. Kang S, Xu M, Cooper EC, Hoshi N. 2014. Channel-anchored protein kinase CK2 and protein phosphatase 1 reciprocally regulate KCNQ2-containing M-channels via phosphorylation of calmodulin. J Biol Chem 289:11536-11544.

265. Abdel-Wahab AF, Mahmoud W, Al-Harizy RM. 2019. Targeting glucose metabolism to suppress cancer progression: prospective of anti-glycolytic cancer therapy. Pharmacol Res 150:104511.

Appendix

Table 2.1 Primers used in Chapter 2

Primer Name	Primer Sequence
TetR STOP 5 Kpn	GGTGGTACCTTAAGACCCACTTTCACATTTAAG
0260BioID 5	GAAGAAACCCTCTCGTAAAAGCAGAGCCGCCATCAACAAGC
0260BioID 3	GCTTGTTGATGGCGGCTCTGCTTTTACGAGAGGGTTTCTTC
HADterm 5	CGATGTACCGGATTACGCATAGGGATGACATGTGATTCGCG
HADterm 3	CGCGAATCACATGTCATCCCTATGCGTAATCCGGTACATCG
IncDTerm 3 Not	GCGGGCGGCCGCGTCTTAGGAGCTTTTTGCAATGC
0260FAPEX2 5	GAAGAAACCCTCTCGTAAAGACTACAAGGATGACGACGATAAG
0260FAPEX2 3	CTTATCGTCGTCATCCTTGTAGTCTTTACGAGAGGGTTTCTTC
APEX2Dterm 5	GAGCGCCTGACCCTGGACTAAGGATGACATGTGATTCGCG
APEX2Dterm 3	CGCGAATCACATGTCATCCTTAGTCCAGGGTCAGGCGCTC
MycAPEX2 5 NheI	GCTGCTAGCATGGAACAAAAACTCATCTCAGAAGAGGATCTCGGAAAGTCTTACCCAACTGTG
APEX2 3 XhoI	CTCCTCGAGGTCCAGGGTCAGGCGCTCCAG
CERT 5 KpnI	GGTGGTACCATGTCGGATAATCAGAGCTGG
CERTAPEX2 5	GCAGGAAAGCCTATTTTGTTCGACTACAAGGATGACGACG
CERTAPEX2 3	CGTCGTCATCCTTGTAGTCGAACAAAATAGGCTTTCCTGC
APEX2STOP 3 Not1	GCGGCGGCCGCTTAGTCCAGGGTCAGGCGCTCCAG

Table 3.1 Primers used in Chapter 3

Primer Name	Primer Sequence
AldoA Fwd BamHI	GGAGGATCCATGCCCTACCAATATCCAGCACTG
AldoA Rev XhoI	CTCCTCGAGTTAATAGGCGTGGTTAGAGAC
PKM2 Fwd BamHI	GGAGGATCCATGTCGAAGCCCCATAGTGAAGC
PKM2 Rev XhoI	CTCCTCGAGTCACGGCACAGGAACAACACG
LDHA Fwd EcoRI	GAAGAATTCTATGGCAACTCTAAAGGATCAG
LDHA Rev XhoI	CTCCTCGAGTTAAAATTGCAGCTCCTTTTG
HAAldoA 5 KpnI	GGTGGTACCATGTACCCTTACGATGTACCGGATTACGCAATGCCCTACCAATATCC
AldoA 3 NotI	GCGGCGGCCGCTTAATAGGCGTGGTTAGAGACG
R42A AldoA Fwd	GAGCATTGCCAAGGCACTGCAGTCCATTGG
R42A AldoA Rev	CCAATGGACTGCAGTGCCTTGGCAATGCTC
R148 AldoA Fwd	CTTCGCCAAGTGGGCATGTGTGCTGAAG
R148 AldoA Rev	CTTCAGCACACATGCCCACTTGGCGAAG
CTL0184 129 130 IBS1/2	AAAAAAGCTTATAATTATCCTTATCATGCATCGCAGTGCGCCCAGATAGGGTG
CTL0184 129 130 EBS1/delta	CAGATTGTACAAATGTGGTGATAACAGATAAGTCATCGCAGGTAACTTACCTTTCTTTGT
CTL0184 129 130 EBS2	TGAACGCAAGTTTCTAATTTCGATTCATGATCGATAGAGGAAAGTGTCT
CTL0184 Up	GCAGAAATAGGTCTGAGGCTG
CTL0184 Dwn	CAACGAATTAGACATTCGTC

Table 3.2 Primers and probes used for quantitative PCR analysis in Chapter 3

Gene	Probe	Primer	Sequence
16S rRNA	#105	Ct 16s Fwd	gccgctaataccgaatgtg
		Ct 16s Rev	aaggtcctaagatcccttcttt
omcA	#33	CTL0703 Fwd	cggtggttgcaactcttgta
		CTL0703 Rev	tcagcatcttggtgcgtatc
pgi	#69	CTL0633 Fwd	gctgctgcgatagcaagac
		CTL0633 Rev	atacagaaactctgcaagacgaag
dhnA	#24	CTL0467 Fwd	ttcagtcaagttgaagatgccta
		CTL0467 Rev	agtaaatcgttgctccgacag
pykF	#159	CTL0586 Fwd	gataggccctgcaacgaata
		CTL0586 Rev	cattcatccctgcatcgag

Table 4.1: Primers used in Chapter 4

Primer Names:	Primer Sequences:
VAPAN1H3	AAGAAGCTTATGGCGTCCGCCTCAGGGGCCATGGCG
VAPAN1Age	ACCACCGGTGGCAAGATGAATTTCCCTAGAAAG
VAPA K50L 3	GTAGTCTTCACTAGGAAACACAC
VAPA K50L 5	GTGTGTTTCCTAGTGAAGACTAC
VAPAATG Not 5	GCGGGCGGCCGCATGGCGTCCGCCTCAGGGGC
VAPAMSP Bam 3	GGAGGATCCCTACATTTCAAATACGCATCTC
0260ATG167 Bam 5	GGAGGATCCATGCAAGTTGAGTTAGCTGCCTG
0260STOP Xho 3	CTCCTCGAGTTATTTACGAGAGGGTTTCTTCTTTTG
IncV T265D P266A 3	CGGACAGTTCTTTATCGCTATTTGGTGCGTCGTGGAAGCTAGAAG
IncV T265D P266A 5	CTTCTAGCTTCCACGACGCACCAAATAGCGATAAAGAACTGTCCG
TetR STOP 5 Kpn	GGTGGTACCTTAAGACCCACTTTCACATTTAAG
0260 1-356 3	CATGGTCTTTGTAGTCcatTTGAGATGAATCGGAAGAGG
0260 1-356 5	CCTCTTCCGATTCATCTCAAatgGACTACAAAGACCATG
IncDTerm 3 Not	GCGGGCGGCCGCgtcttaggagcttttttgcaatgc
0260 1-341 3	CATGGTCTTTGTAGTCcatGTCTTGTCTTTGCTCTTGGTC
0260 1-341 5	GACCAAGAGCAAAGACAAGACatgGACTACAAAGACCATG
IncVS345,346,350A 3	GAATCGGAAGATGCTTCCTCATCTGCTGCTTCGCTGCTGTC
IncV S345,346,350A 5	GACAGCAGCGAAGCAGCAGATGAGGAAGCATCTTCCGATTC
IncV T265A 3	CAGTTCTTTATCGCTATTTGGTGGTGCGTGGAAGCTAGAAG
IncV T265A 5	CTTCTAGCTTCCACGCACCACCAAATAGCGATAAAGAACTG
IncV T236A T239A 3	GCTCACTATCTGCAGAATGTGCGGTTGTAGAG
IncV T236A T239A 5	CTCTACAACCGCACATTCTGCAGATAGTGAGC
0260 ncAT-A 3	GGTGGAGTGTGGAAGCTTGCTGCTGCTGCTGCTGCTGCTGCTG CTTGAGGACTGACAGAAGTTAG
0260 ncAT-A 5	CTAACTTCTGTCAGTCCTCAAGCAGCAGCAGCAGCAGCAGCAG CAGCAAGCTTCCACACTCCACC
0260 cAT-A 3	CAAGAGCATCCATATATTCTGCTGCTGCTGCTGCTGCTGCATTC GAGTCGGACAGTTC
0260 cATA-A 5	GAACTGTCCGACTCGAATGCAGCAGCAGCAGCAGCAGCAGCAGAA TATATGGATGCTCTTG
0260 ncAT-D 3	GGTGGAGTGGGTAAGCTATCATCATCATCATCATCATCATCATCAT CTTGAGGACTGACAGAAGTTAG
0260 ncAT-D 5	CTAACTTCTGTCAGTCCTCAAGATGATGATGATGATGATGATGATG ATGATAGCTTACCCACTCCACC
0260 cAT-D 3	CAAGAGCATCCATATATTCATCATCATCATCATCATCATCATCATTC GAGTCGGACAGTTC
0260 cAT-D 5	GAACTGTCCGACTCGAATGATGATGATGATGATGATGATGATGAAT ATATGGATGCTCTTG